

TECHNISCHE UNIVERSITÄT MÜNCHEN

Fachgebiet Organische Chemie

Creation of Novel Pulses for Magnetic Resonance by Optimal Control

Manoj Manohar Nimbalkar

Vollständiger Abdruck der von der Fakultät für Chemie der Technischen Universität
München zur Erlangung des akademischen Grades eines

Doktors der Naturwissenschaften

genehmigten Dissertation.

Vorsitzender: Univ.-Prof. Dr. Bernd Reif
Prüfer der Dissertation: 1. Univ.-Prof. Dr. Steffen J. Glaser
2. Univ.-Prof. Dr. Axel Haase

Die Dissertation wurde am 27.10.2011 bei der Technischen Universität München eingereicht
und durch die Fakultät für Chemie am 01.12.2011 angenommen.

गुकारु तो अज्ञान अंधकारु । येयाचा निराशु तो रुकारु ।
करी अज्ञानासी संव्हारु । तो गुरु म्हणीजे ॥ २७ ॥

विवेकसिंधू

। आई तुच माझा गुरु ।

The first letter “गु” (Gu) of “गुरु”, (Guru) Teacher, represents the darkness of illiteracy, ignorance, unawareness. The second letter “रु” (Ru) stands for the eradication of that darkness. Therefore, who brings/helps you from the darkness of ignorance towards the path of enlightenment is a true “गुरु”.

Viveksindhu

My Mother has always guided me through the difficult situations and showed me the ways towards the right directions. Therefore, she is and will be my true “गुरु”, who showed me the path toward the enlightenment.

मी हा प्रबंध आजी ,अण्णा आणि आजोबा यांना समर्पित करतो.

I dedicate this Thesis to my grandparents Aaji and Anna, and Aajoba.

Declaration

I hereby declare that parts of this Thesis are already published/submitted or planned to be submitted in scientific journals:

List of Publications

Linear phase slope in pulse design: Application to coherence transfer;
Naum I. Gershenson, Thomas E. Skinner, Bernhard Brutscher, Navin Khaneja, Manoj Nimbalkar, Burkhard Luy, Steffen J. Glaser, *J. Magn. Reson.*, **192**, 235–243 (2008).

Broadband 180° universal rotation pulses for NMR spectroscopy designed by optimal control;
Thomas E. Skinner, Naum I. Gershenson, Manoj Nimbalkar, Wolfgang Bermel, Burkhard Luy, Steffen J. Glaser, [arXiv: 1111.6647](https://arxiv.org/abs/1111.6647), *J. Magn. Reson.*, *in press*, 2011.

Optimal control design of band-selective excitation pulses that accommodate relaxation and RF inhomogeneity;
Thomas E. Skinner, Naum I. Gershenson, Manoj Nimbalkar, Steffen J. Glaser, [arXiv: 1111.6650](https://arxiv.org/abs/1111.6650), *J. Magn. Reson.*, *submitted*, 2011.

Multiple-spin coherence transfer in linear Ising spin chains and beyond: numerically-optimized pulses and experiments;
Manoj Nimbalkar, Robert Zeier, Jorge L. Neves, S. Begam Elavarasi, Haidong Yuan, Navin Khaneja, Kavita Dorai, and Steffen J. Glaser, [arXiv: 1110.5262](https://arxiv.org/abs/1110.5262), *Phys. Rev. A*, *in press*, 2011.

The Fantastic Four: A plug ‘n’ play set of optimal control pulses for enhancing nmr spectroscopy;
Manoj Nimbalkar, Burkhard Luy, Thomas E. Skinner, Jorge L. Neves, Naum I. Gershenson, Kyryl Kobzar, Wolfgang Bermel, Steffen J. Glaser, *in preparation*.

Eidesstattliche Versicherung

Ich versichere, dass ich die von mir vorgelegte Dissertation selbständig angefertigt, die benutzten Quellen und Hilfsmittel vollständig angegeben und die Stellen der Arbeit, die anderen Werken im Wortlaut oder dem Sinn nach entnommen sind, in jedem Einzelfall als Entlehnung kenntlich gemacht habe; dass diese Dissertation noch keiner anderen Fakultät oder Universität zur Prüfung vorgelegen hat; dass sie abgesehen von unten angegebenen Teilpublikationen noch nicht veröffentlicht worden ist sowie, dass ich eine solche Veröffentlichung vor Abschluss des Promotionsverfahrens nicht vornehmen werde. Die Bestimmungen dieser Promotionsordnung sind mir bekannt. Die von mir vorgelegte Dissertation ist von Herrn Prof. Dr. S. J. Glaser betreut worden.

Publikationsliste

Linear phase slope in pulse design: Application to coherence transfer;
Naum I. Gershenzon, Thomas E. Skinner, Bernhard Brutscher, Navin Khaneja, Manoj Nimbalkar, Burkhard Luy, Steffen J. Glaser, *J. Magn. Reson.*, **192**, 235–243 (2008).

Broadband 180° universal rotation pulses for NMR spectroscopy designed by optimal control;

Thomas E. Skinner, Naum I. Gershenzon, Manoj Nimbalkar, Wolfgang Bermel, Burkhard Luy, Steffen J. Glaser, [arXiv: 1111.6647](https://arxiv.org/abs/1111.6647), *J. Magn. Reson.*, *in press*, 2011.

Optimal control design of band-selective excitation pulses that accommodate relaxation and RF inhomogeneity;

Thomas E. Skinner, Naum I. Gershenzon, Manoj Nimbalkar, Steffen J. Glaser, [arXiv: 1111.6650](https://arxiv.org/abs/1111.6650), *J. Magn. Reson.*, *submitted*, 2011.

Multiple-spin coherence transfer in linear Ising spin chains and beyond: numerically-optimized pulses and experiments;

Manoj Nimbalkar, Robert Zeier, Jorge L. Neves, S. Begam Elavarasi, Haidong Yuan, Navin Khaneja, Kavita Dorai, and Steffen J. Glaser, [arXiv: 1110.5262](https://arxiv.org/abs/1110.5262), *Phys. Rev. A*, *in press*, 2011.

The Fantastic Four: A plug ‘n’ play set of optimal control pulses for enhancing nmr spectroscopy;

Manoj Nimbalkar, Burkhard Luy, Thomas E. Skinner, Jorge L. Neves, Naum I. Gershenzon, Kyril Kobzar, Wolfgang Bermel, Steffen J. Glaser, *in preparation*.

Abstract

This thesis is concerned with developing, optimizing, and implementing shaped pulses and pulse sequences using the principles of optimal control theory (Chapter 2). It helps to solve some of the most basic yet important problems in nuclear magnetic resonance (NMR) spectroscopy and magnetic resonance imaging (MRI), such as inhomogeneity in the radio frequency (RF) fields delivered to the sample, the need for large chemical shift bandwidth, and loss of signal intensity due to relaxation.

Considering the specific application for high-field NMR spectroscopy Chapter 3 presents robust broadband excitation pulses optimized using optimal control methods with a defined linear phase dispersion. This makes it possible to create pulses that are equivalent to ideal hard pulses followed by an effective evolution period. Chapter 4 introduces new modifications of the optimal control algorithm that incorporate symmetry principles and relax conservative limits on peak RF pulse amplitude for short time periods to generate a set of broadband universal rotation pulses. They are suitable for widespread use in carbon spectroscopy on the majority of available probes.

Chapter 5 puts forth relaxation-compensated and RF-inhomogeneity robust selective excitation pulses for short longitudinal (T_1) and transverse (T_2) relaxation equal to the pulse length, which reduces signal loss significantly while achieving nearly ideal frequency selectivity. Improvements in performance are the result of allowing residual unrefocused magnetization after applying relaxation-compensated selective excitation by optimized pulses (RC-SEBOP).

Chapter 6 presents numerical approaches to create multiple (3-6) spin coherence for spins-1/2 in multi-dimensional NMR experiments for Ising coupled three to six spins-1/2 with equal and unequal couplings. These pulses are significantly shorter in duration compared to conventional pulse sequences. Utilizing the DANTE approach the shaped pulses were made broadband and implemented experimentally and compared with conventional pulse sequences to create the desired coherence order for three and four spins-1/2 systems.

The last Chapter 7 is about “Fantastic Four” (Fanta4) pulses, a set of highly robust, optimal control-based shaped pulses that are able to replace all hard pulses (in one-to-one fashion) in pulse sequences consisting of 90° and 180° pulses for better performance. The set of four pulses for each nucleus consists of point-to-point (PP) 90° and 180° , and universal rotation (UR) 90° and 180° pulses of identical duration (1 ms).

Zusammenfassung

Diese Arbeit befasst sich mit der Entwicklung, Optimierung und Implementierung von geformten Pulsen und Pulssequenzen, die Prinzipien aus der optimalen Steuerungstheorie verwenden (Kapitel 2). Sie trägt dazu bei, einige der grundlegendsten und zugleich wichtigsten Probleme der NMR-Spektroskopie und der MR-Bildgebung zu lösen, wie zum Beispiel Inhomogenität der auf die Probe eingestrahlten Radiofrequenz-Felder, der Bedarf für große chemische Verschiebungsbandbreite und relaxationsbedingter Verlust der Signalintensität.

Unter Beachtung spezifischer Anwendungen für die Hochfeld-NMR-Spektroskopie werden in Kapitel 3 robuste und breitbandige Anregungspulse vorgestellt, die unter Verwendung von Methoden der optimalen Steuerungstheorie optimiert wurden und eine lineare Phasendispersion aufweisen. Dies ermöglicht die Erzeugung von Pulsen, die sich äquivalent verhalten, wie ein idealer harter Puls gefolgt von einem effektiven Evolutionsdelay. In Kapitel 4 werden neue Modifikationen des optimalen Steuerungsalgorithmus vorgestellt, die Symmetrieprinzipien berücksichtigen und konservative Beschränkungen der höchstmöglichen RF-Pulsamplitude für kurze Zeitabschnitte lockern, um eine Gruppe von breitbandigen universellen Rotationspulsen zu erzeugen. Sie sind für vielfältige Anwendungen in der Kohlenstoffspektroskopie und für die Mehrzahl der gängigen Probenköpfe geeignet.

In Kapitel 5 werden relaxationskompensierte und RF-Inhomogenitäts-robuste selektive Anregungspulse vorgestellt deren Pulsdauer gleich der longitudinalen T_1 und transversalen T_2 Relaxationszeiten sind. Dadurch wird der Signalverlust signifikant reduziert und gleichzeitig eine nahezu ideale Frequenzselektivität erreicht. Verbesserte Ergebnisse können dadurch erzielt werden, dass nicht refokussierte Magnetisierung nach Anwendung eines relaxationskompensierten selektiven Anregungspulses (relaxation-compensated selective excitation by optimized pulses, RC-SEBOP) zugelassen wird.

In Kapitel 6 werden numerische Verfahren zur Erzeugung von mehrfachen (3-6) Spinkohärenzen für Spin-1/2-Systeme in mehrdimensionalen NMR-Experimenten für drei und sechs Ising-Spins 1/2 mit gleichen und unterschiedlichen Kopplungen vorgestellt. Diese Pulse weisen im Vergleich zu konventionellen Pulssequenzen deutlich kürzere Pulsdauern auf. Unter Verwendung des DANTE-Verfahrens wird die Breitbandigkeit dieser Pulse erhöht. Sie werden experimentell implementiert und mit einer konventionellen Pulssequenz verglichen, die die gewünschte Kohärenzordnung für ein drei- und ein vier-Spin-1/2-System erzeugt.

Das letzte Kapitel 7 behandelt "Fantastic Four" (Fanta4) Pulse, eine Gruppe von besonders robusten und auf optimaler Steuerungstheorie basierenden Pulsen, die ("eins-zu-eins") alle harten 90° und 180° Pulse in Pulssequenzen ersetzen können, um eine bessere Leistung zu erzielen. Die Gruppe von vier Pulsen für jeden Kern besteht aus Punkt-zu-Punkt (PP) 90° und 180° Pulsen und aus universellen 90° und 180° Rotationspulsen (UR) gleicher Dauer (1 ms).

Acknowledgements

I would like to thank all with whom I worked during my thesis. I would like to give special thanks to Burkhard Luy, Jorge L. Neves, Kyril Kobzar and Nikolas Pomplum for their initial help and also to Raimond Marx, Andreas Spörl, Robert Fischer, Uwe Sander, Grit Kummerlöwe, Jochen Klages, Arnaud Ngongang Djintchui, Xiaodong Yang, Michael Braun, Martin Janich, Dr. Rainer Haeßner, Dr. Gerd Gemmecker, Adeline Palisse, Ariane Garon, Mirjam Holbach, Martha Fill, and rest of Glaser group; Kessler group; Luy group. I would like to thank my theoretical collaborators, Robert Zeier, Navin Khaneja, Naum I. Gershenson, and special thank to Thomas E. Skinner for his advice. I would like to thank Dr. Wolfgang Eisenreich for allowing to use spectrometer at their facility in Department of Chemie, TUM. I would like to thank Bayerisches NMR Zentrum. I would like to thank TUM Graduate school. I am very grateful to all my friends, teachers and others whom I did not mention here.

Without saying I am very grateful to my family (Aai, Pappa, Dada and Vaini, Vashutai and bhauji, and Balutai and jiju, mothe Mama and Mami, Mama and Mami, and all other) and for their moral support, motivation, and encouragement.

Finally, I would like to thank Prof. Steffen J. Glaser for his exceptional supervision.

Contents

1	Prologue	1
1.1	Prospect	1
1.2	Lay out of thesis	1
1.3	Synopsis of Chapters	2
2	Optimal control methodologies	5
2.1	Introduction	5
2.2	Optimal control using Bloch equation	5
2.2.1	Classical Euler-Lagrange formalism	6
2.2.2	Optimal control algorithm without relaxation	6
2.2.3	Optimal control algorithm with relaxation	7
2.3	Optimal control using Liouville-von Neuman equation	8
3	Linear phase slope in pulse design	11
3.1	Introduction	11
3.2	Phase Slope	12
3.3	Optimal control algorithm	12
3.4	Applications	13
3.4.1	Shorter broadband excitation	13
3.4.2	Coherence transfer	13
3.4.3	Experimental	14
3.5	Conclusion	15
4	Broadband 180° universal rotation pulses	21
4.1	Introduction	21
4.2	Optimal control algorithm for 180° _{UR} pulses	22
4.2.1	Flavor I (basic vanilla)	22
4.2.2	Flavor II (symmetry principle)	23
4.2.3	Flavor III (time-dependent RF limit)	23
4.3	BURBOP compared to refocusing with PP pulses	23
4.3.1	Algorithms A _T and A _{S,T}	24
4.4	Experiment	27
4.5	Conclusion	27
5	Band-selective excitation pulses that accommodate relaxation and RF inhomogeneity	35
5.1	Introduction	35
5.2	Selective pulse design	36
5.2.1	Phase slope	36

5.2.2	Selective pulses as digital filters	37
5.2.3	Optimal control	37
5.3	Results and Discussion	38
5.3.1	Tolerance to RF inhomogeneity	39
5.3.2	Compensation for relaxation and RF inhomogeneity	39
5.4	Experimental	44
5.5	Conclusion	48
6	Time optimal pulses for multiple-spin coherence transfer	49
6.1	Introduction	49
6.2	Coherence transfer in linear Ising spin chains	51
6.3	Linear three-spin chains: analytic and numerical approaches	52
6.3.1	Analytic approach	52
6.3.2	Numerical approach	53
6.4	Linear four-spin chains: analytic and numerical approaches	55
6.4.1	Analytic approach	55
6.4.2	Numerical approach	56
6.5	More generally-coupled spin systems of three and four spins	57
6.5.1	Three-spin system	58
6.5.2	Four-spin system	58
6.6	Experimental results	58
6.6.1	Conventional pulse sequences	64
6.7	Linear spin chains with more than four spins	64
6.8	Conclusion	65
7	The Fantastic Four: A plug ‘n’ play set of optimal control pulses	67
7.1	Introduction	67
7.2	Optimization	69
7.3	Experiments	70
7.4	Results	70
7.4.1	HSQC: Testing with Sodium Formate	70
7.4.2	HSQC: Testing with Hydroxycitronellal	70
7.4.3	HMBC: Testing on Real molecule	73
7.5	Discussion	73
7.6	Conclusion	78
7.7	Appendix	78
7.7.1	Optimization of pulse pairs for two coupled heteronuclear spins-1/2	78
7.7.2	Fanta4 pulse selection	79
7.7.3	Fanta4 pulse shapes and excitation profiles	82

Abbreviations

- NMR: Nuclear Magnetic Resonance
- MRI: Magnetic Resonance Imaging
- RF: Radio Frequency
- B_1^0 : Nominal RF amplitude
- T_1 : Longitudinal relaxation time
- T_2 : Transverse relaxation time
- RC-SEBOP: Relaxation-Compensated Selective Excitation by Optimized Pulse
- DANTE: Delays Alternating with Nutations for Tailored Excitation
- Fanta4: Flavored rf and offset robust Alike-duration Numerically-optimized Trouble-free Applicable 4 pulses
- PP: Point to point pulse
- UR: Universal Rotation pulse
- B_0 : The Static magnetic field
- ICEBERG: Inherent Coherence Evolution optimized Broadband Excitation Resulting in constant phase Gradients
- BURBOP: Broadband Universal Rotation by Optimized Pulses
- EPR: Electron Spin Resonance
- DNP: Dynamic Nuclear Polarization
- HMQC: Heteronuclear Multiple Quantum Coherence
- RF_{\max} : Maximum RF amplitude
- T_p or t_p : Total pulse duration
- FIR: Finite Impulse Response
- BW: Band Width
- SLR: Shinnar-LeRoux algorithm
- COSY: Correlation Spectroscopy

- INEPT: Insensitive Nuclei Enhanced by Polarization Transfer
- GRAPE: Gradient Ascent Pulse Engineering
- TOP: Time Optimal Pulse curve
- HSQC: Heteronuclear Single Quantum Coherence
- HMBC: Heteronuclear Multiple-Bond Coherence
- INADEQUATE: Incredible Natural Abundance Double Quantum Transfer Experiment
- NOESY: Nuclear Overhauser Enhancement Spectroscopy

List of Figures

2.1	Optimization scheme.	8
3.1	Performance of a 16.7 μ s hard pulse.	14
3.2	Amplitude-modulated pulse of length 39 μ s and peak RF amplitude = 15 kHz, optimized to excite transverse magnetization M_{xy} with linear phase slope $R = 1/2$ over resonance offsets of 50 kHz.	15
3.3	The use of a linear phase slope pulse to reduce the delay τ in selective coherence transfer in the case where T_p is relatively long.	16
3.4	The RF amplitude and Phase are plotted for ICEBERG pulses of $R = -0.5$ to 0.95.	17
3.5	Excitation profile of ICEBERG pulses with different R compared with hard pulse ($T_p = 16.7 \mu$ s)	18
3.6	Creation of ICEBERG-HMQC from conventional HMQC.	19
3.7	Experimental comparison of ICEBERG-HMQC and hard pulse HMQC	20
4.1	The amplitude and phase of adiabatic Chirp80 pulse from Bruker pulse library.	25
4.2	The amplitude and phase of 180°_{UR} pulse 4 from Table 1 obtained using algorithm $A_{S,T}$	25
4.3	Theoretical performance of four 180°_{UR} pulses for inversion of magnetization about the y-axis, designed using different algorithms.	26
4.4	Theoretical performance of pulse 1 and pulse 4 of Table, and composite adiabatic pulse for inversion of magnetization about the y-axis.	28
4.5	Simulations: Further quantitative detail for the $M_x \rightarrow -M_x$ transformation from Fig. 4.4b for pulse 4 of Table 1 and Fig. 4.4c for Chirp80.	29
4.6	Experimental measurements of the inversion profile and phase deviation for pulse 4 of Table 1 and adiabatic Chirp80.	30
4.7	Experimental lineshapes (black) comparing optimal control 180°_{UR} pulse 4 of Table 1 and adiabatic Chirp80.	31
4.8	Simulations: Further quantitative detail for the $M_y \rightarrow M_y$ transformation from Fig. 4.4b for pulse 4 of Table 1 and Fig. 4.4c for Chirp80.	32
4.9	Experimental measurements of the $M_y \rightarrow M_y$ and phase deviation for pulse 4 of Table 1 and adiabatic Chirp80.	33
4.10	Simulations and experimental detail for the $M_z \rightarrow -M_z$ transformation from Fig. 4.4b for pulse 4 of Table 1 and Fig. 4.4c for Chirp80.	34
5.1	The ideal rectangular frequency response for a finite length selective pulse.	38
5.2	Simulations: Selectivity comparison of SLR and SEBOP pulse.	40
5.3	Simulations: Excitation profile comparison for SLURP-1 and RC-SEBOP.	42

5.4	Simulations: Excitation profile comparison for eSNOB and RC-SEBOP.	43
5.5	The sequences are designed to eliminate residual y -magnetization.	45
5.6	Experimental selectivity profiles of RC-BEBOP and eSNOB for $T_1 = T_2 = T_p = 1$ ms.	46
5.7	Experimental selectivity profiles of RC-BEBOP and eSNOB for short T_1 and T_2 than T_p	47
6.1	A linear three-spin chain.	52
6.2	Analytic pulses for linear three-spin chains.	52
6.3	The schematic coupling topology of the three-spin systems.	53
6.4	A linear four-spin chain.	55
6.5	Analytic pulses for linear four-spin chains.	56
6.6	The topology of a four-spin system.	56
6.7	Comparison numerically-optimized TOP curves for three-spin systems with one and six RF controls keeping $J_{12} = J_{23} = 88.05$ Hz constant while varying J_{13}	59
6.8	In the DANTE approach an on-resonance shaped pulse is converted to a series of short hard pulses and delays Δ_i	60
6.9	Simulation and experimental profile comparison of conventional and broadband version of $k = 1$ analytic pulse for linear three spin system.	60
6.10	Simulation and experimental profile comparison of conventional and broadband version of $k = 1.59$ analytic pulse for linear three spin system.	62
6.11	Simulation and experimental comparison of conventional pulse sequence, analytical, and numerical shaped pulses for four spin system.	63
6.12	The RF controls for numerically-optimized pulse shapes for linear spin chains of length five and six.	64
7.1	This schematic demonstrates a simple block of hard pulses.	68
7.2	Creation of Fanta4-HSQC from conventional-HSQC.	71
7.3	Creation of Fanta4-HMBC from conventional-HMBC.	72
7.4	The structure of molecules used for comparison of conventional pulse sequences and Fanta4 pulse sequences.	73
7.5	1D-HSQC: Chemical shift ($\Delta\nu$) excitation profile comparison of Fanta4 and conventional -HSQC.	74
7.6	Fanta4-HSQC projection compared with conventional-HSQC.	75
7.7	2D Fanta4-HMBC compared with conventional-HSQC.	76
7.8	Traces of 2D HMBC.	77
7.9	The amplitude and phase of ^1H and ^{13}C pulses optimized simultaneously.	80
7.10	Simulation of ^1H and ^{13}C pulses optimized simultaneously.	81
7.11	A product operator analysis for the combinations of PP_H 90° pulse with rest of ^{13}C pulses.	83
7.12	A product operator analysis for the combinations of PP_H 180° pulse with rest of ^{13}C pulses.	84
7.13	A product operator analysis for the combinations of UR_H 90° pulse with rest of ^{13}C pulses.	85
7.14	A product operator analysis for the combinations of UR_H 180° pulse with rest of ^{13}C pulses.	86
7.15	Figure depicts the combinatorial approach to select the best set of pulses.	87
7.16	The amplitude and phase of ^1H Fanta4 pulses.	88
7.17	Experimental performance of ^1H Fanta4 pulses as function of the offset for single spin.	89

7.18	The amplitude and phase of ^{13}C Fanta4 pulses.	90
7.19	Experimental performance of ^{13}C Fanta4 pulses as function of the offset for single spin.	91

List of Tables

4.1	List of four pulses optimized using different algorithm to execute a 180° universal rotation about the y -axis.	27
6.1	Comparison of the duration t_p , the fidelity F , and the shape of numerically-optimized pulses for a linear three-spin chains.	54
6.2	For coherence transfers in linear three-spin chains, list of the numerically-optimized times t_p and the fidelities F in the case of one, two, and six RF controls.	55
6.3	Plot of controls along y axis for linear four-spin chains with coupling ratios $k_1 = 1$ and $k_2 = 1$, and $k_1 = 2.38$ and $k_2 = 0.94$	57
6.4	For coherence transfers in linear four-spin chains ($k_1 = k_2 = 1$ as well as $k_1 = 2.38$ and $k_2 = 0.94$), list of the numerically-optimized times t_p and the fidelities F in the case of two, four, and eight RF-controls.	58
6.5	Numerical results for more generally-coupled three-spin systems.	61
6.6	Numerical results for a more generally-coupled four-spin systems with coupling ratios $k_1 = 2.38$ and $k_2 = 0.94$	62
6.7	Comparison of the duration t_p and fidelity F of numerically-optimized shaped pulses in the case of three- and four-spin systems allowing a varying number of RF controls u	63
6.8	Comparison of the minimum time t_p required for a coherence transfer by numerically-optimized (oc) and conventional (conv) pulse sequences.	65
7.1	Q_2 is summarized for the current set of ^1H and ^{13}C Fanta4 pulses.	82

Chapter 1

Prologue

1.1 Prospect

Nuclear Magnetic Resonance (NMR) is an interesting, important and an indispensable technique in a very wide variety of fields. In organic chemistry and structural biology NMR is one of the most important tools for the elucidation and determination of three-dimensional structures for small molecules, proteins and other macromolecules. It gives us information on internal mobility and overall molecular motion in both large and small molecules. Magnetic Resonance Imaging (MRI) has become one of the best methods for obtaining anatomical images of human subjects and animals and for exploring physiological processes. Materials science uses NMR spectroscopy and imaging to describe the structure, motion, and electronic properties of heterogeneous and technologically important substances. NMR is widely used in the food industry to measure moisture content and to assess the quality of certain foodstuffs. Moreover, NMR is used to measure the flow of liquids in pipes in industrial processes and to observe the flow of blood in human beings and is used in the exploration for petroleum.

However, the static magnetic field (B_0) and radio frequency (RF) pulses, which govern the individual nucleus in a molecule or human tissue during NMR or MRI measurements, are associated with intrinsic problems such as inhomogeneous B_0 and RF fields delivered to the sample, increase in chemical shift bandwidth due to increase in B_0 field strength e.g., for ^{13}C and ^{31}P nuclei, and loss of signal intensity due to relaxation effects. This thesis focuses on developing, optimizing, and implementing shaped pulses and pulse sequences using principles of optimal control theory which are robust to RF inhomogeneity, large chemical shift bandwidth, and relaxation effects. This helps to solve some of the most basic yet important problems in NMR spectroscopy and MR imaging.

1.2 Lay out of thesis

Every chapter in general is arranged in the following way,

- Introduction,
- Theory,
- Experiment(s),

- Conclusion
- Appendix (if necessary)

and at the end is a Bibliography of all chapters.

1.3 Synopsis of Chapters

- **Chapter 2**

Chapter 2 gives the overview of the basic optimal control methodologies, which are already developed for non-interacting and coupled spin systems. These methodologies were used as a basis to develop further control schemes that respects given constraints in the rest of the chapters.

- **Chapter 3**

Using optimal control methods, robust broadband excitation pulses can be designed with a defined linear phase dispersion. This makes it possible to create pulses that are equivalent to ideal hard pulses followed by an effective evolution period. For example, in applications, where the excitation pulse is followed by a constant delay, e.g., for the evolution of heteronuclear couplings, part of the pulse duration can be absorbed in existing delays, significantly reducing the time overhead of long, highly robust pulses. We refer to the class of such excitation pulses with a defined linear phase dispersion as ICEBERG pulses (Inherent Coherence Evolution optimized Broadband Excitation Resulting in constant phase Gradients). A systematic study of the dependence of the excitation efficiency on the phase dispersion of the excitation pulses is presented, which reveals surprising opportunities for improved pulse sequence performance.

- **Chapter 4**

Broadband inversion pulses that rotate all magnetization components 180° about a given fixed axis are necessary for refocusing and mixing in high-resolution NMR spectroscopy. The relative merits of various methodologies for generating pulses suitable for broadband refocusing are considered. The de novo design of 180° universal rotation pulses (180_{UR}°) using optimal control can provide improved performance compared to schemes which construct refocusing pulses as composites of existing pulses. The advantages of broadband universal rotation by optimized pulses (BURBOP) are most evident for pulse design that includes tolerance to RF inhomogeneity or miscalibration. We present new modifications of the optimal control algorithm that incorporate symmetry principles and relax conservative limits on peak RF pulse amplitude for short time periods that pose no threat to the probe. We apply them to generate a set of 180_{BURBOP}° pulses suitable for widespread use in ^{13}C spectroscopy on the majority of available probes.

- **Chapter 5**

Existing optimal control protocols for mitigating the effects of relaxation and/or RF inhomogeneity on broadband pulse performance are extended to the more difficult problem of designing robust, refocused, frequency selective excitation pulses. For the demanding case of short T_1 and T_2 equal to the pulse length, anticipated signal losses can be significantly reduced while achieving nearly ideal frequency selectivity. Improvements in performance are the result of allowing residual unrefocused magnetization after applying relaxation-compensated selective excitation

by optimized pulses (RC-SEBOP). This unwanted residual signal is easily eliminated in a single-acquisition sequence or using the two-scan acquisition sequence that achieves the calculated theoretical performance for the refocused component.

- **Chapter 6**

We study multiple-spin coherence transfers in linear Ising spin chains with nearest neighbor couplings. These constitute a model for efficient information transfers in future quantum computing devices and for many multi-dimensional experiments for the assignment of complex spectra in nuclear magnetic resonance spectroscopy. We complement prior analytic techniques for multiple-spin coherence transfers with a systematic numerical study where we obtain strong evidence that a certain analytically-motivated family of restricted controls is sufficient for time-optimality. In the case of a linear three-spin system, additional evidence suggests that prior analytic pulse sequences using this family of restricted controls are time-optimal even for arbitrary local controls. In addition, we compare the pulse sequences for linear Ising spin chains to more realistic spin systems with additional long-range couplings between non-adjacent spins. We implement the derived pulse sequences in three and four spin systems and demonstrate that they are applicable in realistic settings under relaxation and experimental imperfections—in particular—by deriving broadband pulse sequences which are robust with respect to frequency offsets.

- **Chapter 7**

We present “Fantastic Four” (Fanta4: Flavored rf and offset robust Alike-duration Numerically-optimized Trouble-free Applicable 4) pulses, a set of highly robust, optimal control-based shaped pulses that are able to replace all hard pulses, in a one-to-one fashion, in pulse sequences consisting of 90° and 180° pulses for better performance. The set of four pulses for each nucleus consists of point-to-point (PP) 90° and 180° , and universal rotation (UR) 90° and 180° pulses of identical duration (1 ms). These pulses are robust to a range of frequency offsets (20 kHz for ^1H and 35 kHz for ^{13}C) and tolerate reasonably large radio frequency (RF) inhomogeneity/miscalibration ($\pm 15\%$ for ^1H and $\pm 10\%$ for ^{13}C). We compare the experimental performance of conventional pulse sequences to the corresponding Fanta4-pulse sequence.

Chapter 2

Optimal control methodologies

2.1 Introduction

Optimal control theory originally was introduced for optimizations in engineering and economy. In recent years, optimal control theory is considered as a methodology for pulse sequence design in liquid state NMR, solid state NMR, EPR, DNP, quantum computing, and being used in MR imaging [1]. It provides systematically imposing desirable constraints on a spin system evolution and therefor has a wealth of applications. In applications of NMR spectroscopy and MRI, it is desirable to have optimized pulses and pulse sequences tailored to specific applications, such as, pulses which are robust to radio frequency (RF) miscalibration/inhomogeneity, which excites spins at large chemical shift ranges and robust to relaxation effects of the individual nucleus. It helps to maximize the coherence transfer between coupled spins in multi-dimensional NMR pulse sequences and improves the overall signal to noise ratio.

From an engineering perspective all these problems are challenges in optimal control where one is interested in tailoring the excitation of a dynamical system to maximize a given performance criterion. This chapter introduces a basic overview of the use of principles of optimal control theory to develop algorithms to design robust broadband excitation pulses (Chapter 3), universal rotation pulses (Chapter 4), relaxation and RF inhomogeneity optimized selective excitation pulses (Chapter 5), and pulses for effective multiple coherence transfer for more than two spin system (Chapter 6).

2.2 Optimal control using Bloch equation

In 1946 Felix Bloch formulated a set of equations that describe the behavior of a non-interacting nuclear spins in a magnetic field under the influence of RF pulses. Bloch assumed that nuclear spins relax following the application of RF pulses along z-axis and in the x-y plane at different rates following a first -order kinetics. These rates are designated $1/T_1$ and $1/T_2$ for z-axis and x-y plane, respectively. T_1 is called spin-lattice (longitudinal) relaxation and T_2 is called spin-spin (transverse) relaxation. In the following, we will use Bloch equations without and with relaxation to calculate the trajectories of the non-interacting spins.

2.2.1 Classical Euler-Lagrange formalism

Optimal control theory is a generalization of the classical Euler-Lagrange formalism [2]. The goal is to find the curve or trajectory $x(t)$ which optimizes the value of the functional

$$\mathcal{J}[x] = \int_{t_0}^{t_1} \mathcal{L}[t, x(t), u(t)] dt \quad (2.1)$$

over the time interval $[t_0, t_1]$. In classical mechanics, $u = dx/dt$, $x(t_0)$ and $x(t_1)$ are fixed, and the curves $x(t)$ and $u(t)$ are required to be continuous. The necessary condition that such a curve be an optimizing curve is that the variation $\delta\mathcal{J}$ at all points of the path be equal to zero, which results in the familiar Euler-Lagrange differential equation for the Lagrangian \mathcal{L} [3]. Additional constraints which can be imposed on points of the optimization curve, of the form $g(x) = c$, are included in the formalism by introducing Lagrange multipliers λ_j for each constraint equation g_j , which transform the Euler-Lagrange equation for \mathcal{L} to a similar one for the function

$$h = \mathcal{L} - \sum_j \lambda_j g_j. \quad (2.2)$$

2.2.2 Optimal control algorithm without relaxation

For the non-interacting spins in NMR without relaxation effects, the goal is to find the trajectory by optimal control for the magnetization vector $M(t)$ that optimizes a suitably chosen cost function \mathcal{J} . In units of angular frequency (rad/s), the effective RF field in the rotating frame is

$$\omega_e = \omega_1(t)[\cos\varphi(t)\hat{x} + \sin\varphi(t)\hat{y}] + \Delta\nu(t)\hat{z}, \quad (2.3)$$

which contains any desired modulation of the amplitude ω_1 , phase φ , and frequency offset $\Delta\nu$ of the pulse. The possible trajectories $M(t)$ are constrained to satisfy the Bloch equation

$$\dot{M} = \omega_e \times M, \quad (2.4)$$

which therefore introduces three Lagrange multipliers λ_j (see Section 2.2.1). The three constraint functions g_j in Eq. 2.2 are then simply the components of the vector

$$g = \omega_e \times M. \quad (2.5)$$

Since $\omega_e(t)$ controls the evolution of $M(t)$, the goal of finding the optimum trajectory is the same as finding the optimal RF sequence to apply to the spins in a sample. Given an initial state $M(t_0)$ and a desired final or target state F at the end of the pulse, we want to optimize

$$\mathcal{J}[M] = \int_{t_0}^{t_p} \mathcal{L}[t, M(t), \omega_e(t)] dt + \Phi[M(t_p)] \quad (2.6)$$

over the interval $[t_0, t_p]$. Compared to Eq. 2.1, we now have $u = \omega_e$. Typically, the running cost function \mathcal{L} is chosen with no explicit dependence on M or t . In addition, a final cost term $\Phi[M]$ evaluated at the end of the pulse is generally included.

Including the Bloch equation constraint on M , the requirement $\delta\mathcal{J} = 0$ implies

$$\dot{\lambda} = -\partial h / \partial M \quad (2.7)$$

with initial condition

$$\lambda(t_p) = -\partial\Phi / \partial M \quad (2.8)$$

for the time evolution of λ , and

$$\partial h(t)/\partial \omega_e(t) = 0, \quad (2.9)$$

at all points on the optimal trajectory, which provides a means for adjusting the RF controls. By analogy with the Hamiltonian formalism of classical mechanics, M and λ are conjugate variables, since

$$\dot{M} = \omega_e \times M = \partial h / \partial \lambda. \quad (2.10)$$

according to Eqs. 2.2 and 2.5.

2.2.3 Optimal control algorithm with relaxation

Following section 2.2.2, the Bloch equation for the non-interacting spins with relaxation T_1 and T_2 will be

$$\dot{M}(t) = \omega_e(t) \times M(t) + D[M_0 - M(t)], \quad (2.11)$$

where $M_0 = \hat{z}$ is the unit equilibrium polarization for appropriately normalized units, the effective field ω_e in rad/s is given in terms of the time-dependent RF amplitude ω_1 and phase φ in Eq. 2.3 and the relaxation matrix is

$$D = \begin{pmatrix} 1/T_2 & 0 & 0 \\ 0 & 1/T_2 & 0 \\ 0 & 0 & 1/T_1 \end{pmatrix}. \quad (2.12)$$

Including relaxation a time-dependent hamiltonian h can be redefined in terms of a Lagrange multiplier λ as

$$h(t) = \lambda(t) \cdot \dot{M}(t) = \lambda \cdot [\omega_e \times M + D(M_0 - M)], \quad (2.13)$$

which returns the Bloch equation as

$$\dot{M} = \partial h / \partial \lambda, \quad (2.14)$$

with the known value $M(t_0)$ at the beginning of the pulse. For a given cost function Φ chosen to measure the pulse performance, the optimization formalism results in the conjugate or adjoint equation

$$\dot{\lambda}(t) = -\partial h / \partial M \quad (2.15)$$

$$\dot{\lambda}(t) = \omega_e(t) \times \lambda(t) + D\lambda(t), \quad (2.16)$$

with the value $\lambda(t_p) = \partial \Phi / \partial M$ required at the end of the pulse, giving $\lambda(t_p) = F$ for the cost

$$\Phi = M(t_p) \cdot F, \quad (2.17)$$

for example.

The final necessary condition that must be satisfied by a pulse that optimizes the cost function is

$$\partial h(t) / \partial \omega_e(t) = 0 = M(t) \times \lambda(t), \quad (2.18)$$

at each time. For a non-optimal pulse, Eq. 2.18 is not fulfilled. It then represents a gradient giving the proportional adjustment to make in the controls $\omega_e(t)$ for the next iteration towards an optional solution. For more details and applications refer to Ref. [4] and Chapter 5.

This numerical algorithm can be generalized for desired applications in NMR such as excitation and inversion of a given spin system with defined constraints. The following steps explain how the optimizing the cost (Φ) /desired target (F) can be incorporated in an algorithm:

1. Choose initial RF controls/sequence ω_e^0 .
2. Evolve M forward in time from the initial state $M(t_0)$.
3. Evolve λ backwards in time from the target state F (see Figure 2.1).
4. $\omega_e^{k+1}(t) \rightarrow \omega_e^k(t) + \epsilon[M(t) \times \lambda(t)]$, where ϵ is a suitable step size.
5. With these as the new controls, go to step 2 until a desired convergence of Φ is reached.

More details can be found in Ref [5].

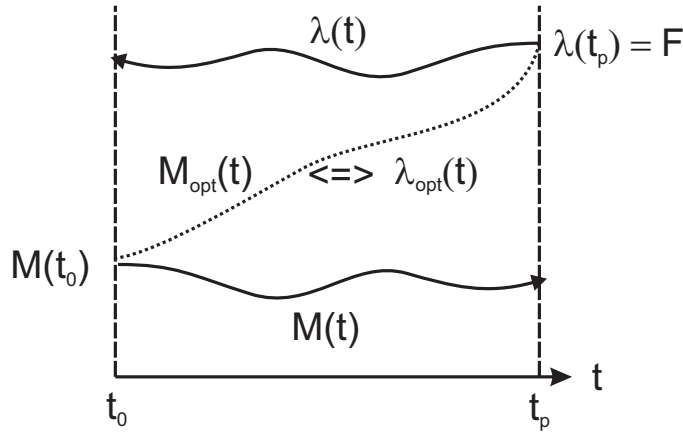


Figure 2.1: (Figure adapted from Ref. [5]) Optimization scheme. For a given RF sequence $\omega_e(t)$, the initial state $M(t_0)$ evolves to some final state $M(t_p)$ through a sequence of intermediate states, shown schematically as the solid line connecting $M(t_0)$ and $M(t_p)$. Similarly, the desired final target state F , which equal to the Lagrange multiplier term $\lambda(t_p)$ according to Eqs. 2.8 and 2.17, evolves backwards in time to some initial state $\lambda(t_0)$. The separate paths for $M(t)$ and $\lambda(t)$ becomes equal for the optimized RF sequence $\omega_{opt}(t)$ and drives $M(t_0)$ to $\lambda(t_p) = F$. At each time, a comparison of the two paths via $M(t) \times \lambda(t)$ gives the proportional adjustment ϵ to make in each component of the control field $\omega_e(t)$ to bring the two paths closer together.

2.3 Optimal control using Liouville-von Neuman equation

The Bloch equation is unable to treat coupled spin systems and hence we have to change to Liouville-von Neuman equation where the state of the spin system is defined by the density operator $\rho(t)$. The Liouville-von Neuman equation for transfer between Hermitian operators in absence of relaxation is

$$\dot{\rho}(t) = -i[(H_0 + \sum_{k=1}^m u_k(t)H_k), \rho(t)], \quad (2.19)$$

where H_0 is the free evolution Hamiltonian, H_k are the RF Hamiltonians corresponding to available control fields and $u(t) = (u_1(t), u_2(t), \dots, u_m(t))$ represents the vector of amplitudes that can be changed and which is referred to as control vector. The problem is to find the optimal control amplitudes $u_k(t)$ of the RF fields that steer a given initial density operator $\rho(0) = \rho_0$ in a specified time T to a density operator $\rho(T)$ with

maximum overlap to some desired target operator F . For Hermitian operator ρ_0 and F , this overlap can be measured by the standard inner product

$$\langle F|\rho(T)\rangle = \text{Tr}\{F^\dagger \rho(T)\}. \quad (2.20)$$

Hence, the performance index Φ of the transfer process can be defined as

$$\Phi = \langle F|\rho(T)\rangle. \quad (2.21)$$

In the following, we will assume for simplicity that the chosen transfer time T is discretized in N equal steps of duration $\Delta t = T/N$ and during each step, the control amplitudes u_k are constant, i.e. during the j th step the amplitude $u_k(t)$ of the k th control Hamiltonian is given by $u_k(j)$. The time-evolution of the spin system during a time step j is given by the propagator

$$U_j = \exp\{-i\Delta t(H_0 + \sum_{k=1}^m u_k(t)H_k)\}. \quad (2.22)$$

The final density operator at time $t = T$ is

$$\rho(T) = U_n \dots U_1 \rho_0 U_1^\dagger \dots U_N^\dagger, \quad (2.23)$$

and the performance function Φ to be maximized can be expressed as

$$\Phi = \langle F|U_n \dots U_1 \rho_0 U_1^\dagger \dots U_N^\dagger\rangle. \quad (2.24)$$

Using the definition of the inner product (Eq. 2.21) and the fact that the trace of a product is invariant under cyclic permutations of the factors, this can be rewritten as

$$\Phi = \underbrace{\langle U_{j+1}^\dagger \dots U_N^\dagger F U_N \dots U_{j+1} |}_{\lambda_i} \underbrace{|U_j \dots U_1 \rho_0 U_1^\dagger \dots U_j^\dagger\rangle}_{\rho_j}. \quad (2.25)$$

where ρ_j is the density operator $\rho(t)$ at time $t = j\Delta t$ and λ_j is the backward propagated target operator F at the same time $t = j\Delta t$. Let us see how the performance Φ changes when we perturb the control amplitude $u_k(j)$ at time step j to $u_k(j) + \delta u_k(j)$. From Eq. 2.22, the change in U_j to first order in $\delta u_k(j)$ is given by

$$\delta U_j = -i\Delta t \delta u_k(j) \overline{H}_k U_j \quad (2.26)$$

with

$$\overline{H}_k \Delta t = \int_0^{\Delta t} U_j(\tau) H_k U_j(-\tau) d\tau \quad (2.27)$$

and

$$U_j(\tau) = \exp\left\{-i\tau\left(H_0 + \sum_{k=1}^m u_k(j)H_k\right)\right\}. \quad (2.28)$$

This follows from the standard formula

$$\frac{d}{dx} e^{A+xB}|_{x=0} = e^A \int_0^1 e^{A\tau} B e^{-A\tau} d\tau. \quad (2.29)$$

For small Δt (when $\Delta t \ll \|H_0 + \sum_{k=1}^m u_k(j)H_k\|^{-1}$), $\overline{H}_k \approx H_k$ and using Eqs. 2.25 and 2.26 we find to first order in Δt

$$G_j = \frac{\delta\Phi}{\delta u_k(j)} = -\langle \lambda_j | i\Delta t [H_k, \rho_j] \rangle. \quad (2.30)$$

Observe we increase the performance function Φ if we choose

$$u_k(j) \rightarrow u_k(j) + \epsilon \frac{\delta\Phi}{\delta u_k(j)}, \quad (2.31)$$

where ϵ is a small step size. This forms the basis of the following algorithm, which is known as the gradient ascent pulse engineering (GRAPE) to distinguish it from conventional gradient approaches used in NMR based on difference methods.

Basic GRAPE algorithm

1. Guess initial controls $u_k(j)$.
2. Starting from ρ_0 , calculate $\rho_j = U_j \dots U_1 \rho_0 U_1^\dagger \dots U_j^\dagger$ for all $j \leq N$.
3. Starting from $\lambda_N = F$, calculate $\lambda_j = U_{j+1}^\dagger \dots U_N^\dagger F U_N \dots U_{j+1}$ for all $j \leq N$.
4. Evaluate $\frac{\delta\Phi}{\delta u_k(j)}$ and update the $m \times N$ control amplitudes $u_k(j)$ according to Eq.2.31.
5. With these as the new controls, go to step 2.

The algorithm is terminated if the change in the performance index Φ is smaller than a chosen threshold value.

For treatment of non-Hermitian operators and for relaxation-optimized coherence transfer refer to Refs. [6, 7].

Chapter 3

Linear phase slope in pulse design: Application to coherence transfer

3.1 Introduction

This chapter is a part of an article [8] and it focuses on applications and experimental implementations of ICEBERG (Inherent Coherence Evolution optimized Broadband Excitation Resulting in constant phase Gradients) pulses. The fundamental goal of pulse sequence design is to control spin trajectories. Although the ideal final state of the sample magnetization just prior to acquisition may be obvious for a given application, how to achieve this state can be less obvious. Optimal control theory [9] is a powerful method which can be applied to this problem. It has been used, for example, to derive ultra-broadband excitation pulses, BEBOP [10–14], which are tolerant to RF inhomogeneity/ miscalibration and require no phase correction. This imposes a rather stringent requirement on the optimal control algorithm for a range of possible RF calibrations, it must drive all spins within the desired range of resonance offsets to the same final state. Yet, a linear phase dispersion in the final magnetization as a function of offset is readily corrected in many practical applications utilizing, for example, hard pulses or Gaussian pulses [15].

We have formerly compared BEBOP performance (no phase correction required) to a phase-corrected hard pulse, since this is an excellent benchmark for broadband excitation. BEBOP pulses are exceptional by this standard, but a fairer comparison would entail optimized pulses that can be phase-corrected, also. We therefore consider the advantages of allowing this increased flexibility in pulse design.

The slope of the phase as a function of offset appears to be an important parameter for pulse design. Applications include increased bandwidth for a given pulse length compared to equivalent pulses requiring no phase correction (or, shorter pulses for the same bandwidth), selective pulses, and pulses that mitigate the effects of relaxation [16]. In particular, we consider pulses for coherence transfer that make it possible to absorb some of the evolution time for heteronuclear couplings into the excitation pulse. One can then utilize specific performance benefits of relatively long pulses without adding significantly to the experiment time.

3.2 Phase Slope

We are interested in controlling the phase, φ , that the transverse magnetization, M_{xy} , acquires during a pulse of length T_p . The phase is measured here from the x-axis. Requiring the slope of the phase to be constant as a function of resonance offset $\Delta\nu$ (units of radians/s) gives a linear phase for M_{xy} , which is desirable for many applications. The particular value for the slope, $\partial\varphi/\partial\Delta\nu$, then requires some elaboration.

In the absence of the pulse, the phase acquired by M_{xy} at offset $\Delta\nu$ during time T_p due to chemical-shift evolution is $\Delta\nu T_p$, so the slope is equal to T_p . We define a normalized, dimensionless phase slope

$$R = (1/T_p)\partial\varphi/\partial\Delta\nu \quad (3.1)$$

Values of R at each offset characterize the phase relative to the maximum phase that could be produced solely by chemical-shift evolution during the time T_p . A pulse that produces focused magnetization of fixed phase for all spins in the offset range of interest would have a constant $R = 0$ (i.e., a self-refocused pulse). BEBOP pulses obtained to date are typically $R \approx 0$ pulses. It is considered, in the context of relaxation effects, the design of pulses with the equivalent phase slope of a hard pulse [16]. The desired slope is obtained from a hard pulse phase slope (equal to $2/\pi$ on resonance), scaled according to Eq. 3.1 by t_{90}/T_p , where t_{90} is the length of the hard pulse. As expected, there was a considerable performance advantage for such pulses compared to $R = 0$.

The utility of the phase slope is presented by the equivalence of chemical-shift and coupling evolution of an irradiated spin. During the pulse, the effect of the coupling J (in radians/s) on the irradiated spins at a chemical-shift offset $\Delta\nu$ is simply an additional offset $\pm J/2$ for the \pm orientation of the spins. Thus, if the irradiated spins at all offsets in a range of interest are transformed to the same state so that $R = 0$ independent of offset, there is no net J -evolution at the end of the pulse. A different but related definition with relevance to spin decoupling has been presented by Waugh [17]. Conversely, if the chemicalshift evolution of the irradiated spins during a pulse of length T_p is the same as the chemical-shift evolution during a delay of the same length ($R = 1$ for all offsets), the coupling evolution is the undiminished value $(J/2)T_p$. For constant R (i.e., linear phase slope) in the range $0 < R < 1$, partial coupling evolution occurs. In addition, $R < 0$ would generate magnetization of reverse phase that would refocus after a delay RT_p .

More details on applications and the range of R attainable in practice are discussed in Ref [8].

3.3 Optimal control algorithm

The optimal control methodology has been described in chapter 2 and in detail previously [10–14]. It was used to calculate what are referred to here as $R = 0$ pulses, which transform initial z magnetization to the x-axis for any offset and RF calibration within the design specifications. For excitation of transverse magnetization of phase slope R , we now consider separate target states for each offset of the form

$$\vec{F} = [\cos(\varphi), \sin(\varphi), 0] \quad (3.2)$$

Choosing $\varphi = R(\Delta\nu T_p)$ gives a linear phase slope, which is our focus here, but any function can be considered for its potential to define a useful target phase, making the method completely general.

We have previously input random noise for the initial RF used to start the algorithm. Characterizing the performance of various modifications and additions to the algorithm was an important goal, and we wanted to avoid imposing any bias on what might constitute the best final solution. Inputting noise also served to demonstrate the power and efficiency of optimal control, showing that it is not necessary to guess an approximate solution in order for the algorithm to either converge or converge in a useable time frame, which is often the case in standard optimization routines. Some of the resulting pulses look very much like noise themselves, although their outstanding performance demonstrates they are not at all random.

Now that the algorithm is well-established, we turn to the derivation of smooth pulse shapes. We start the algorithm with an initial RF pulse of constant small amplitude (approximately zero) and constant phase ($\pi/4$). This results in a class of sinc-like pulse shapes that is reminiscent of, and appears to include, polychromatic pulses [18] as a subset. In addition to being easy to implement on a wide range of spectrometers, the shape of the new pulses depends in a very regular fashion on R for values in the range $0 \leq R \leq 1$.

3.4 Applications

3.4.1 Shorter broadband excitation

A hard pulse excites transverse magnetization M_{xy} with an approximately linear phase slope ($R = 2/\pi$ on resonance) that can be corrected in many useful applications. Although a hard pulse is probably the workhorse of NMR spectroscopy, the excitation profile is not uniform as a function of resonance offset, nor is the phase slope. At field strengths approaching 1 GHz and typical ^{13}C probe limits on peak RF amplitude of ~ 15 kHz ($T_p = 16.7 \mu\text{s}$), there is room for improvement, as shown in Fig. 3.1. An ideally calibrated pulse excites 95% of the attainable transverse magnetization over an offset range of ± 17 kHz, and excites less than 90% over ± 25 kHz. The phase is linear to within $\pm 2^\circ$ over the entire offset range of 50 kHz, but can be $3^\circ - 4^\circ$ over large parts of the spectrum, depending on RF inhomogeneity or miscalibration. Accumulated signal losses can be significant when large pulse trains are applied.

Previously, we derived a relatively short $125 \mu\text{s}$ pulse requiring no phase correction ($R = 0$) that uniformly excites 99% magnetization over 50 kHz bandwidth with tolerance to RF inhomogeneity of $\pm 10\%$ [13]. If the pulse is no longer required to be self-refocused, we find the $39 \mu\text{s}$, $R = 1/2$ pulse shown in Fig. 3.2. The excited M_{xy} is greater than 0.99 over the entire 50 kHz bandwidth used in the optimization, and also provides tolerance to RF miscalibration of $\pm 7\%$ ($> 98\%$ for $\pm 10\%$ miscalibration). Deviations in phase linearity (absolute value) are less than 1° over most of the optimization window of ± 25 kHz offset and $\pm 10\%$ RF inhomogeneity, rising to $3^\circ - 4^\circ$ only at the extreme edges of the window.

3.4.2 Coherence transfer

Consider the basic element of a coherence transfer experiment shown in Fig. 3.3A, a 90° pulse followed by a delay of length τ .

For a pulse that produces a linear phase slope in the transverse magnetization, the parameter R can be interpreted as the fraction of the pulse length in which the net chemical-shift (or coupling) evolution occurs, as discussed in Section 3.2. Hence, a pulse

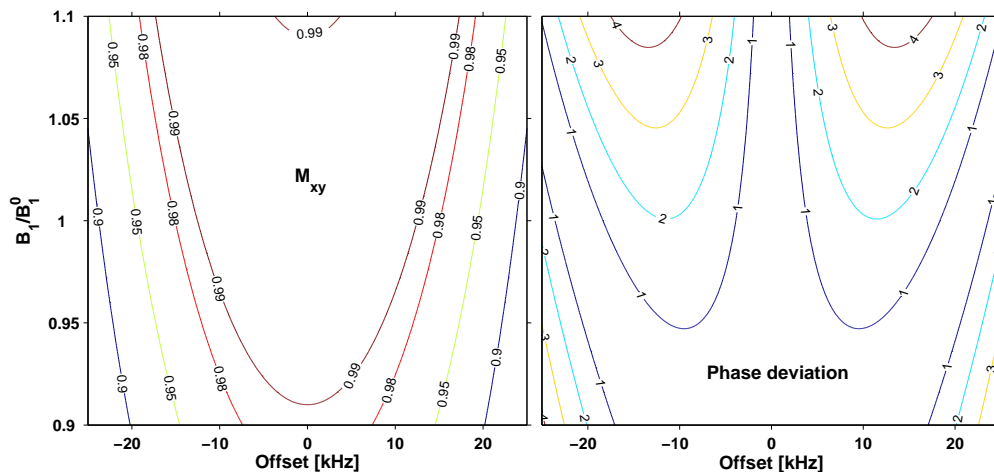


Figure 3.1: (Color online) Performance of a $16.7 \mu\text{s}$ hard pulse, peak RF amplitude = 15 kHz. Transverse magnetization M_{xy} (left panel) and absolute value of the phase deviation from linearity (right panel) are plotted as functions of resonance offset and RF miscalibration/inhomogeneity B_1/B_1^0 . B_1 is the variable RF amplitude and B_1^0 is the nominal RF amplitude.

of phase slope R and duration T_p produces the same phase evolution that would occur for transverse magnetization during a time-delay interval

$$T_{evol} = RT_p, \quad (3.3)$$

as illustrated in Fig. 3.3B. The remaining fraction of the pulse can be represented by a 90° excitation pulse of length

$$T_{exc} = T_p - T_{evol} = (1 - R)T_p, \quad (3.4)$$

in which no phase evolution occurs. Thus, the total time for the $90^\circ - \tau$ element of the sequence can be reduced by the time T_{evol} . The performance advantages of certain kinds of longer pulses, such as BEBOP or selective pulses, can then be more fully exploited if they are designed with large R to avoid increasing the experiment time to an unsatisfactory degree. This interpretation of R also provides additional insight into relaxation-compensated pulses, which can be idealized as excitation with no relaxation during T_{exc} followed by chemical-shift evolution and relaxation during T_{evol} [8].

3.4.3 Experimental

Comparison with hard pulse

Figure 3.4 shows the amplitude and phase of ICEBERG pulses with R from -0.5 to 0.95 and Figure 3.5 shows their excitation profile compared to hard pulse. All experiments were implemented on a Bruker 200 MHz AVANCE spectrometer equipped with SGU units for RF control and linearized amplifiers, utilizing a double-resonance 5 mm SEI probehead and gradients along the z -axis. Measurements are the residual HDO signal in a sample of 99.96% D_2O doped with CuSO_4 to a T_1 relaxation time of 280 ms at 298°K . Signals were obtained at offsets between -25 kHz to 25 kHz in steps of 100 Hz. To

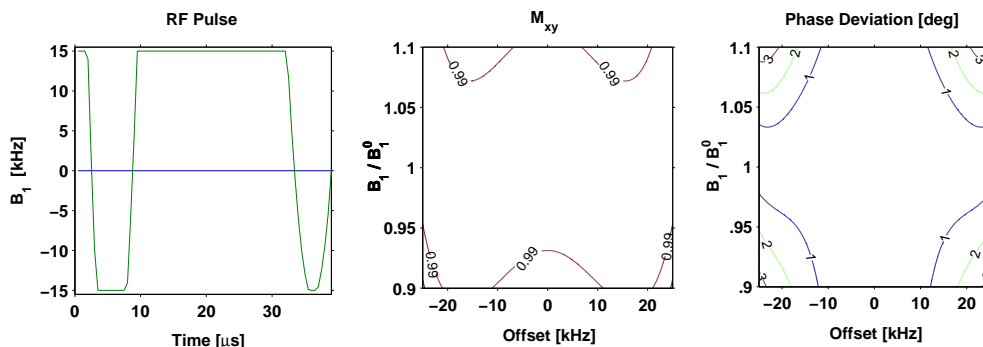


Figure 3.2: (Color online) Amplitude-modulated pulse of length $39 \mu\text{s}$ and peak RF amplitude = 15 kHz, optimized to excite transverse magnetization M_{xy} with linear phase slope $R = 1/2$ over resonance offsets of 50 kHz. The pulse serendipitously provides significant tolerance to RF miscalibration B_1/B_1^0 with small phase deviations (absolute value) from linearity, as shown in the middle and right panels. The 50 kHz, $\pm 10\%$ RF miscalibration window used for the simulations shows $M_{xy} > 0.99$ and phase deviations less than 1° over most of these ranges, with deviations of 3° at the extreme offsets and miscalibrations at the corners of the window.

reduce the effects of RF field inhomogeneity within the coil itself, approximately $40 \mu\text{l}$ of the sample solution was placed in a 5 mm Shigemi limited volume tube.

Coherence transfer in HMQC

The viability of employing relatively long ICEBERG pulses with improved excitation profile compared to a hard pulse is illustrated in Figure 3.7, using a ^{13}C excited and detected HMQC experiment as an example (Fig. 3.6). Although this experiment would realistically be performed using ^1H excitation and detection, the large ^{13}C chemical shift serves as a proxy for similar correlation experiments based on ^{19}F or ^{31}P excitation which will benefit from the ICEBERG scheme.

HMQC performance using a 1.428 ms ICEBERG pulse ($R = 0.95$), optimized to achieve uniform excitation over the full carbon chemical-shift range, is compared to the same experiment using a $35.7 \mu\text{s}$ hard pulse (i.e., RF amplitude equal to the peak RF of the ICEBERG pulse). Embedding the ICEBERG pulse in the delay period results in an effective excitation pulse length $T_{exc} = 71.4 \mu\text{s}$, according to Eq. 3.4. Thus, the duration of the entire experiment is practically identical in both cases. However, in contrast to the ICEBERG version, which provides uniform excitation across the entire offset range, signal intensity in the hard pulse version is reduced by as much as 38% at the edges of the carbon chemical-shift range. Further details are provided in Figure 3.7. The experiments were recorded on a Bruker AVANCE 750 MHz spectrometer using a triple resonance inverse detection room temperature probe head. 1024×128 data points were acquired with corresponding spectral widths of 200.8 ppm (^{13}C) and 8.5 ppm (^1H). Sixteen transients per increment gave an overall experiment time of 35 min for each of the two experiments.

3.5 Conclusion

The features of pulses which excite transverse magnetization with linear phase as a function of offset have been presented. A pulse with phase slope R at resonance offset

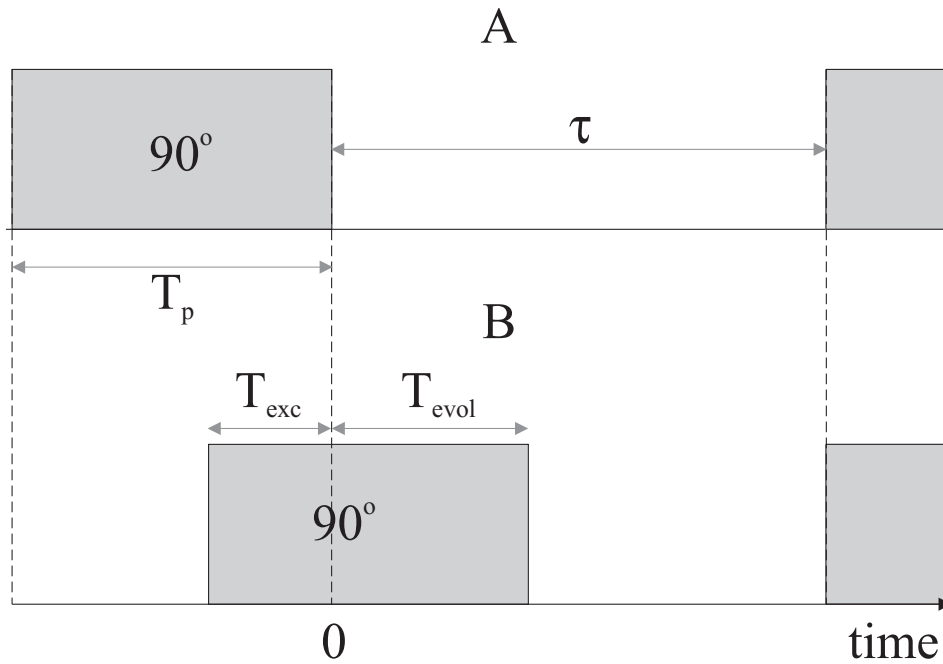


Figure 3.3: The use of a linear phase slope pulse to reduce the delay τ in selective coherence transfer in the case where T_p is relatively long. (A) $R = 0$, requiring $\tau = 1/(2J)$. (B) $R \geq 0$, with $T_{evol} = RT_p$ resulting in chemical shift evolution $\Delta\nu T_{evol}$ during the pulse and thus a coupling evolution $(J/2)T_{evol}$, reducing the delay correspondingly. The pulse can be represented by excitation with no phase evolution during the time T_{exc} followed by free precession during T_{evol} .

$\Delta\nu$ produces a net chemical-shift evolution $R\Delta\nu T_p$ during a pulse of length T_p . The linear phase evolution gives a J -coupling of RJ during the pulse. Large R then results in significant coupling evolution during the pulse, enabling the use of what might otherwise be prohibitively long pulses for coherence transfer.

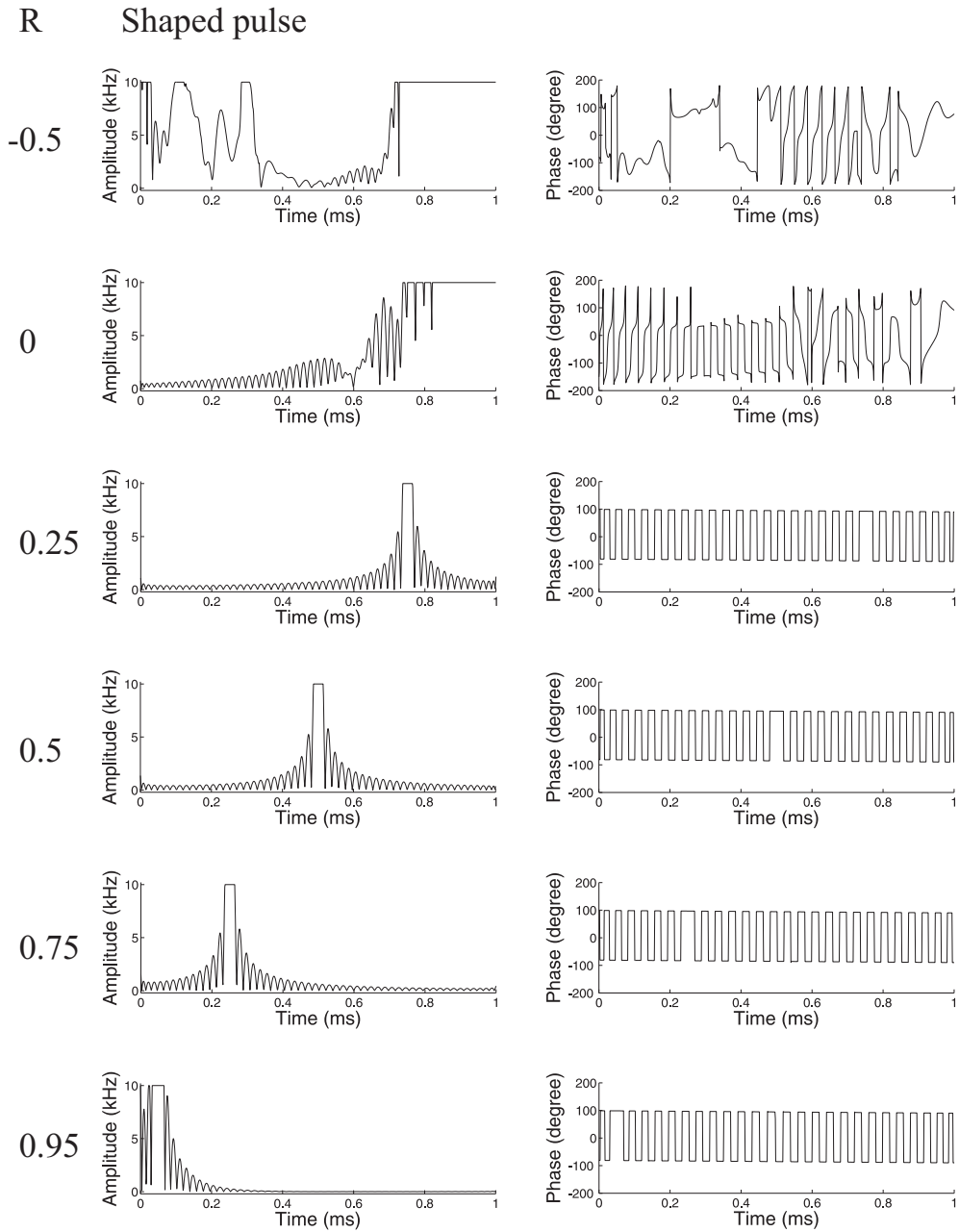


Figure 3.4: The RF amplitude and Phase are plotted as a function of time for a series of 1 ms pulses designed using different values of R and with RF_{lim} of 10 kHz to excite a bandwidth of $\Delta\nu = 50$ kHz.

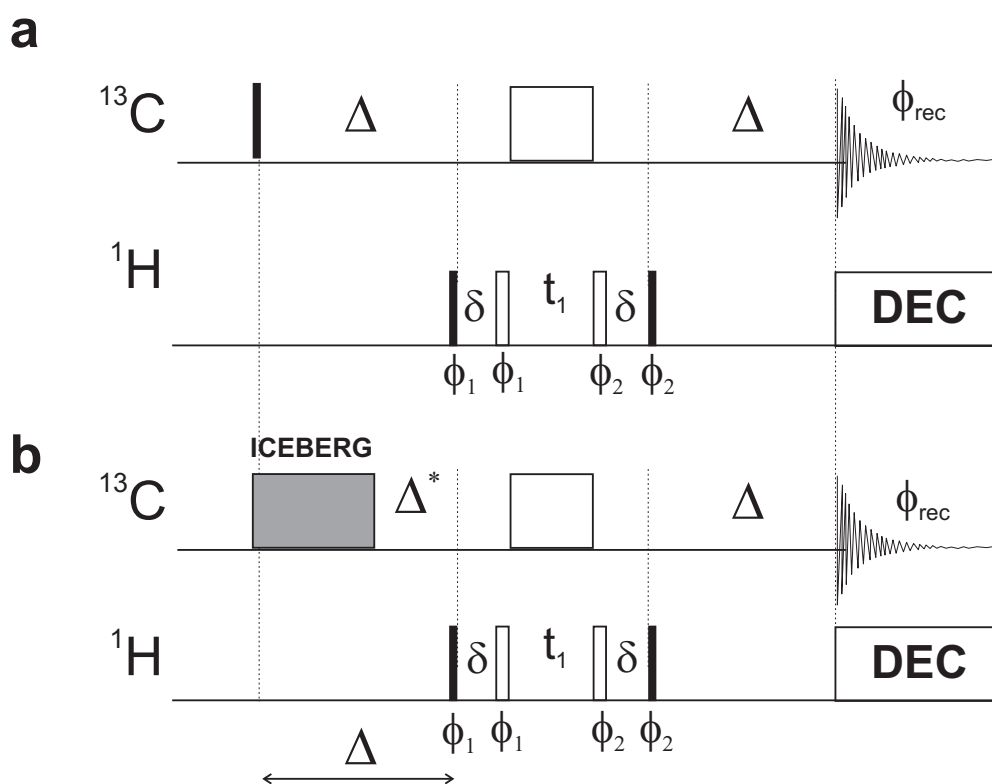


Figure 3.6: Carbon excited and detected HMQC experiment using a conventional 90° hard pulse (a) and an ICEBERG pulse for excitation (b). Filled rectangles correspond to 90° pulses while open rectangles indicate 180° pulses, with the wide box on ^{13}C representing a refocussing pulse constructed out of two phase-modulated excitation pulses [14] using the principle described in Ref. [19]. Phases are x with the exception of $\phi_1 = x, -x$; $\phi_2 = x, x, -x, -x$; and $\phi_{\text{rec}} = x, -x, -x, x$. Delays are $\Delta = 1/(2^1 J_{CH})$, with Δ^* reduced by the effective evolution period of the ICEBERG pulse, $R \cdot T_p$. Both experiments have practically identical overall sequence lengths but the offset-compensated ICEBERG HMQC provides higher sensitivity especially at the edges of the carbon chemical shift range.

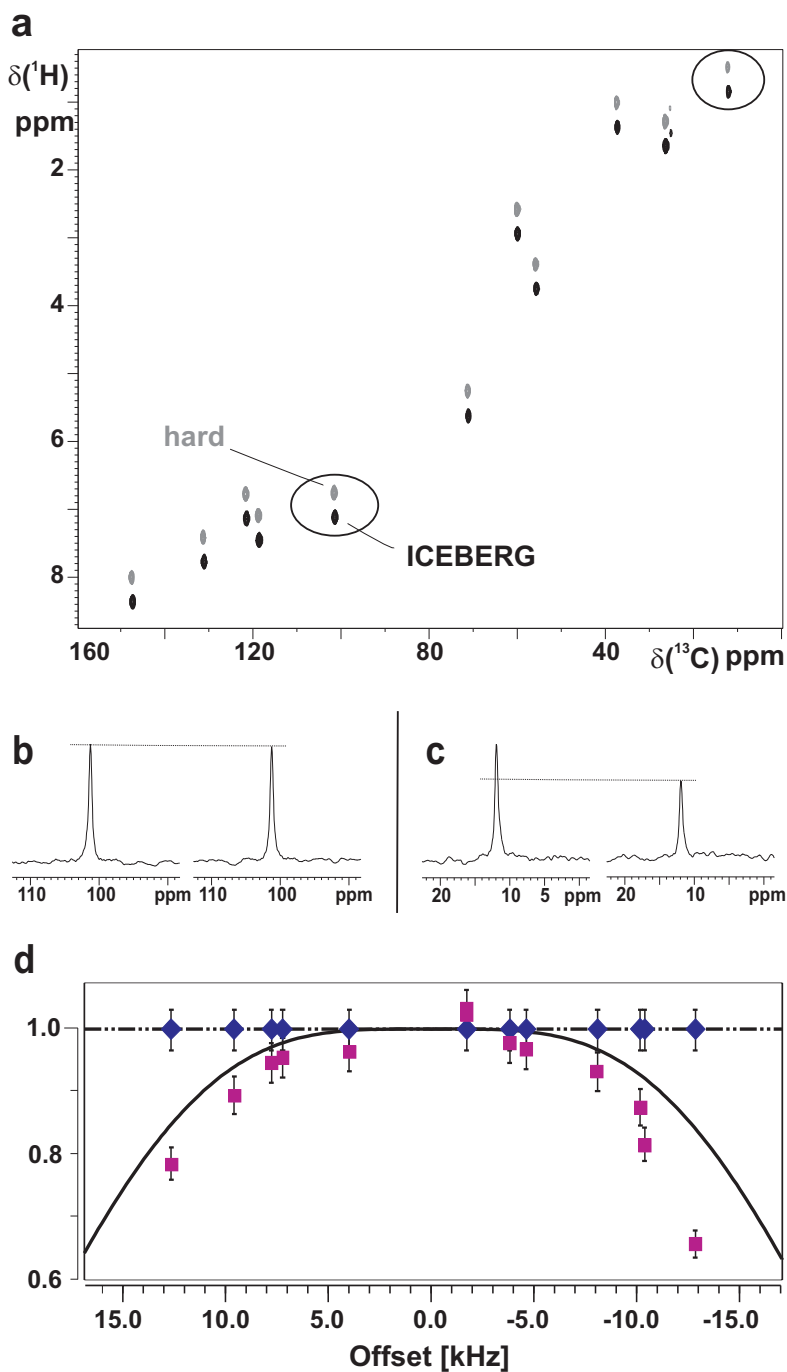


Figure 3.7: (Color online) Experimental data acquired on hydroquinidine in CDCl_3 are shown in (a), with the ICEBERG-HMQC cross peaks shown in black and the hard pulse version shown in gray with a slight shift in ^1H . Slices of the encircled cross peaks near $\delta(^{13}\text{C}) = 100$ ppm are compared in (b) for ICEBERG (left) and the hard-pulse version (right). A similar comparison showing the loss of signal in the hard-pulse version is shown in (c) near $\delta(^{13}\text{C}) = 12$ ppm. The experiment was implemented using a 1.428 ms ICEBERG pulse ($R = 0.95$, giving an effective contribution to the overall pulse sequence length of $1.428 \text{ ms} \times 0.05 = 71.4 \mu\text{s}$) and a hard pulse of $35.7 \mu\text{s}$ duration. The simulation of the offset profiles of the ICEBERG (dash-dotted line) and hard 90° pulse (solid line) are shown in (d) together with the experimental signal intensities (ICEBERG-HMQC signal intensities normalized to 1.0).

Chapter 4

Broadband 180° universal rotation pulses

4.1 Introduction

This chapter is a part of an article [20] and it focuses on applications, and experimental implementation and comparison of BURBOP pulses with Chirp80 [21]. Many NMR applications require refocusing of transverse magnetization, which is easily accomplished on resonance by any good inversion pulse sandwiched between delays, i.e., the standard Δ – 180° – Δ block. For broadband applications, a universal rotation (UR) pulse that rotates any orientation of the initial magnetization 180° about a given fixed axis is required to refocus all transverse magnetization components. A simple hard pulse functions as a UR pulse only over a limited range of resonance offsets that cannot be increased significantly due to pulse power constraints.

Although a great deal of effort has been devoted to increasing the bandwidth of inversion pulses, most broadband inversion pulses [22–37] execute only a point-to-point (PP) rotation for one specific initial state, magnetization $M_z \rightarrow -M_z$, and are not UR pulses. However, two PP inversion pulses with suitable inter-pulse delays can be used to construct a refocusing sequence [38,39], which is effectively a 360°_{UR} pulse. Alternatively, a 180°_{UR} refocusing pulse can be constructed from three adiabatic inversion pulses [40] with either pulse length or bandwidth of the adiabatic frequency sweep in the ratio 1:2:1. More generally, we have shown that one can construct a UR pulse of any flip angle from a PP pulse of half the flip angle preceded by its time- and phase-reversed waveform [41]. Thus, a 180°_{UR} pulse can be constructed from two 90°_{PP} pulses.

The reliance on composites of PP pulses to construct UR pulses highlights the perceived difficulty of creating stand-alone UR pulses. The de novo design of UR pulses for NMR spectroscopy has received comparatively little attention [30,42], so it is an open question whether the composite constructions using PP pulses achieve the best possible performance. Yet, the demonstrated capabilities of optimal control for designing PP pulses [43–56] are equally applicable to the design of UR pulses [57–59]. The required modifications to the basic optimal control algorithm are fairly straightforward [57,60,61] and maintain the same flexibility for incorporating tolerance to variations in experimentally important parameters, such as RF homogeneity or relaxation.

In this chapter, we design broadband refocusing pulses by optimizing the propagator for the required UR transformation. We introduce new optimal control strategies tailored to take advantage of specific opportunities available in the design of UR pulses. The

culmination of these efforts is a set of low-power, high-performance broadband refocusing pulses that satisfy the power constraints of widely available probeheads and complex multipulse sequences.

4.2 Optimal control algorithm for 180°_{UR} pulses

A general procedure for creating a desired unitary propagator in an arbitrary (closed) quantum system is given in [57, 60–62]. Time evolution proceeds according to a matrix exponential of the system Hamiltonian. For two-level systems, as in many NMR applications involving a single noninteracting spin-1/2 species, this evolution is well-known to be equivalent to a rotation of the 3D vector representing the state of the system about the effective applied field [63]. The relatively abstract general procedure for propagator optimization can be made considerably more transparent in this case.

4.2.1 Flavor I (basic vanilla)

The algorithm for generating UR pulses in the single-spin case is a straightforward modification of the PP algorithm. A 180°_{UR} pulse applied, for example, along the y -axis to magnetization \mathbf{M} effects the transformation $(M_x, M_y, M_z) \rightarrow (-M_x, M_y, -M_z)$. This is simply three separate PP transformations of the initial states $\mathbf{M}_1 = (1, 0, 0)$, $\mathbf{M}_2 = (0, 1, 0)$, $\mathbf{M}_3 = (0, 0, 1)$ to their respective target states $\mathbf{F}_1 = (-1, 0, 0)$, $\mathbf{F}_2 = (0, 1, 0)$, $\mathbf{F}_3 = (0, 0, -1)$. The cost function comparing the final states \mathbf{M}_{kf} ($k = 1, 2, 3$) at the end of an RF pulse to the target states is

$$\Phi = \mathbf{F}_1 \cdot \mathbf{M}_{1f} + \mathbf{F}_2 \cdot \mathbf{M}_{2f} + \mathbf{F}_3 \cdot \mathbf{M}_{3f}. \quad (4.1)$$

The algorithm proceeds in the standard fashion using this cost function. We will refer to this as algorithm A.

This simple intuitive modification to the cost is exactly equivalent to an analogous procedure given in [57] for optimizing the unitary propagator, which can be seen as follows. The rotation operator R_F in 3D corresponding to the target propagator that generates a 180° rotation about the y -axis is given by

$$R_F = \begin{pmatrix} -1 & 0 & 0 \\ 0 & 1 & 0 \\ 0 & 0 & -1 \end{pmatrix} = \begin{pmatrix} \vdots & \vdots & \vdots \\ \mathbf{F}_1 & \mathbf{F}_2 & \mathbf{F}_3 \\ \vdots & \vdots & \vdots \end{pmatrix}, \quad (4.2)$$

i.e., the i^{th} column is the corresponding PP target \mathbf{F}_i .

The actual rotation operator at the end of a pulse of length T_p is

$$\begin{aligned} R(T_p) &= R(T_p) \begin{pmatrix} 1 & 0 & 0 \\ 0 & 1 & 0 \\ 0 & 0 & 1 \end{pmatrix} \\ &= R(T_p) \begin{pmatrix} \vdots & \vdots & \vdots \\ \mathbf{M}_1 & \mathbf{M}_2 & \mathbf{M}_3 \\ \vdots & \vdots & \vdots \end{pmatrix} \\ &= \begin{pmatrix} \vdots & \vdots & \vdots \\ \mathbf{M}_{1f} & \mathbf{M}_{2f} & \mathbf{M}_{3f} \\ \vdots & \vdots & \vdots \end{pmatrix}, \end{aligned} \quad (4.3)$$

with the rotation transforming each column to its associated final state for the individual PP transformations.

The cost is again given by the projection of the final state onto the target state, with the inner product

$$\Phi_R = \langle R_F | R(T_p) \rangle = \text{Tr} [R_F^T R(T_p)], \quad (4.4)$$

where superscript \mathcal{T} denotes the transpose, and the operator Tr returns the trace (sum of diagonal elements) of its argument. We then have

$$R_F^T R(T_p) = \begin{pmatrix} \cdots \mathbf{F}_1 \cdots \\ \cdots \mathbf{F}_2 \cdots \\ \cdots \mathbf{F}_3 \cdots \end{pmatrix} \begin{pmatrix} \vdots & \vdots & \vdots \\ \mathbf{M}_{1f} & \mathbf{M}_{2f} & \mathbf{M}_{3f} \\ \vdots & \vdots & \vdots \end{pmatrix}. \quad (4.5)$$

The sum over diagonal elements of this matrix product gives Eq. [4.1].

4.2.2 Flavor II (symmetry principle)

For applications requiring high phase fidelity which can afford modest loss of signal intensity, we therefore incorporate the symmetry principle of the construction procedure into the optimal control algorithm. For RF pulse components u_x and u_y digitized in N time steps, the first half of the pulse is determined using the basic algorithm A. The second half of the pulse is then constructed using the time- and phase-reversed components of the first half. Phase zero for u_x leaves it unaffected, while u_y is inverted to give

$$\begin{aligned} u_x^{i+N/2} &= u_x^{N/2+1-i} \\ u_y^{i+N/2} &= -u_y^{N/2+1-i} \end{aligned} \quad (4.6)$$

for $i = 1, 2, 3, \dots, N/2$. We refer to this algorithm incorporating the symmetry of the construction principle as A_S . For more details refer to Ref. [20]

4.2.3 Flavor III (time-dependent RF limit)

Peak RF amplitude must remain below probe limits (e.g., available for ^{13}C spectroscopy), but larger RF amplitudes result in improved broadband performance. For sufficiently short time periods, we note that probe RF limits can be higher than conservative limits that protect the probe from arcing under any conditions. Enforcing a lower probe limit for an entire pulse duration can sacrifice performance unnecessarily. We therefore introduce a time-dependent RF field limit to allow increased RF amplitude for short time intervals and achieve improved performance. Empirically, we find that low RF limits force algorithm A to request higher RF amplitude in the middle of the pulse for improved performance. We therefore allow a higher RF limit for a short time during the middle of the pulse. We refer to this algorithm as A_T , or, if it is also combined with the symmetry principle, as $A_{S,T}$.

4.3 BURBOP compared to refocusing with PP pulses

In this section we compare the performance of a set of 180°_{BURBOP} pulses that utilize the higher RF power limits allowed for short time intervals to increase the maximum RF amplitude from 11 kHz to 15 kHz (16.7 μs hard pulse) in the middle of the pulse with the composite adiabatic pulse scheme [40] implemented as a smoothed Chirp pulse [21, 64] in standard Bruker software.

4.3.1 Algorithms A_T and $A_{S,T}$

Broadband refocusing bandwidths of ~ 50 kHz, sufficient for high-field ^{13}C spectroscopy, are readily achieved using any of the pulse schemes discussed so far. The peak RF power required for the pulses is well-within hard-pulse power limits for modern high resolution probes. However, in multipulse sequences, repeated application of what might be deemed a modest power level for a single pulse can be a problem if the total energy delivered to the sample (integrated power) is too high. There are also limits on the total energy that can safely be delivered to a given probe. For these reasons, the most general and widespread applications impose peak power levels that are more conservative than what might be necessary for broadband refocusing using a typical probe. We therefore incorporate a time-dependent RF limit into the optimal control algorithms to keep peak power low for most of the pulse, but allow short increases in this limit where it can have the most benefit. We utilize algorithms A_T and $A_{S,T}$ (defined in Section 4.2.3) to investigate the possibility of generic broadband refocusing pulses suitable for use with any standard probehead in any pulse sequence.

Three adiabatic inversion pulses

The best broadband refocusing performance available in the standard Bruker pulse library satisfying the required conservative pulse power limits is obtained using the pulse designated Chirp80 [21]. This pulse is constructed from three adiabatic inversion pulses with pulse lengths in the ratio 1:2:1 [40]. It utilizes for its shortest element a 500 ms smoothed chirp pulse [64] with 80 kHz sweep. The first 20% of the pulse rises smoothly to a maximum constant RF amplitude of 11.26 kHz according to a sine function before decreasing in the same fashion to zero during the final 20% of the pulse. The final pulse is thus 2 ms long (Fig. 4.1).

Maintaining this pulse length and mindful of the given conservative peak RF amplitude, we designed the set of four pulses listed in Table 1. For most of the pulse, the nominal RF amplitude is a constant 10 or 11 kHz. A maximum RF amplitude of 15 kHz is applied for 60 μs in the middle of the pulse, as illustrated in Fig. 4.2. This short increase in pulse amplitude provides significant improvement in pulse performance compared to Chirp80.

The amplitude profile shown in Fig. 4.2 is reminiscent of the hyperbolic secant pulse [27], which maintains a low amplitude for most of the pulse with a peak in the middle. All four pulses show excellent performance over the listed ranges in offset and RF field inhomogeneity/miscalibration. Performance is comparable to the performance shown in Fig. 4.3 for higher power, constant amplitude pulses with nominal peak RF of 15 kHz. Pulse 4 provides the most relevant comparison, since it has a similar range of tolerance to RF inhomogeneity. As expected from the earlier results for algorithms A and A_S , the best amplitude performance is obtained by algorithm A_T and the best phase performance by algorithm $A_{S,T}$. Figure 4.4 compares theoretical performance of pulses 1 and 4 from Table 1 to the Chirp80 pulse. The new pulses significantly improve phase performance over the targeted range of offsets and RF inhomogeneity/miscalibration. Additional quantitative comparison between pulse 4 and Chirp80 are provided in Figs. 4.5 and 4.6, 4.8 and 4.9, and 4.10, which also show the excellent agreement between simulations and experimental pulse performance. Improvements in lineshape and phase that are possible using the new pulses are shown in Fig. 4.7.

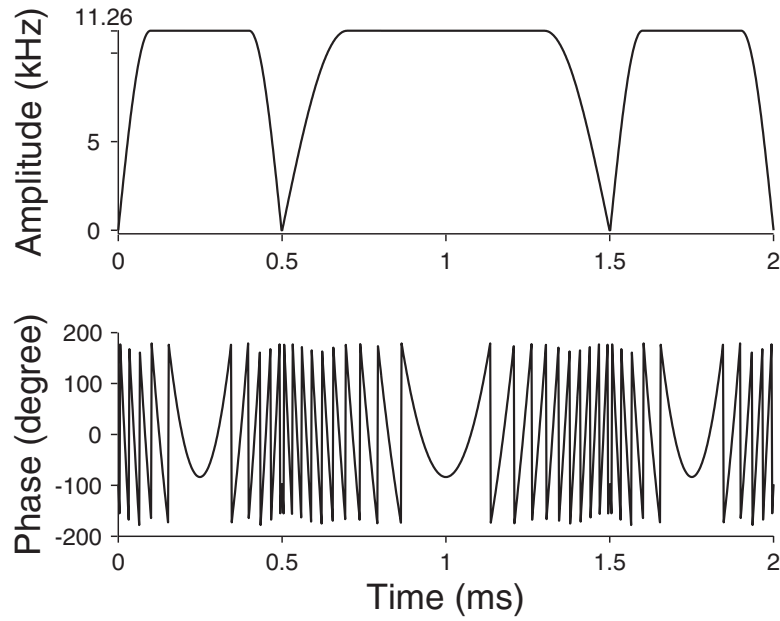


Figure 4.1: The amplitude and phase of adiabatic Chirp80 pulse from Bruker pulse library [21]. This pulse is constructed from three adiabatic inversion pulses with pulse lengths in the ratio 1:2:1 [40] utilizing shortest element with 500 ms smoothed chirp pulse [64] with 80 kHz sweep. The first 20% of the pulse rises smoothly to a maximum constant RF amplitude of 11.26 kHz according to a sine function before decreasing in the same fashion to zero during the final 20% of the pulse. The final pulse is thus 2 ms long.

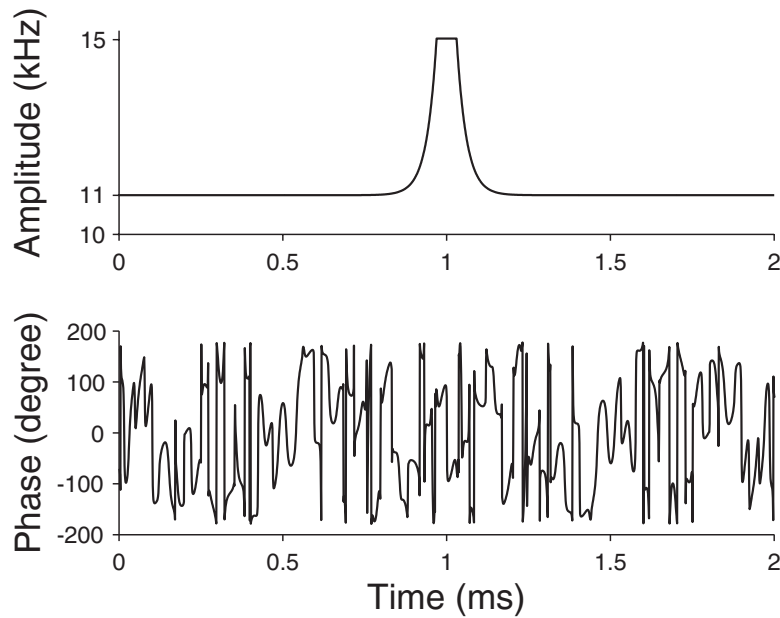


Figure 4.2: The amplitude and phase of 180°_{UR} pulse 4 from Table 1 obtained using algorithm $A_{S,T}$. A conservative limit of 11 kHz for the peak RF applied for 2 ms is relaxed to allow a safe peak of 15 kHz for 60 μ s. The pulse is amplitude-symmetric and phase-antisymmetric in time, incorporating the symmetry of the construction procedure from Ref. [41].

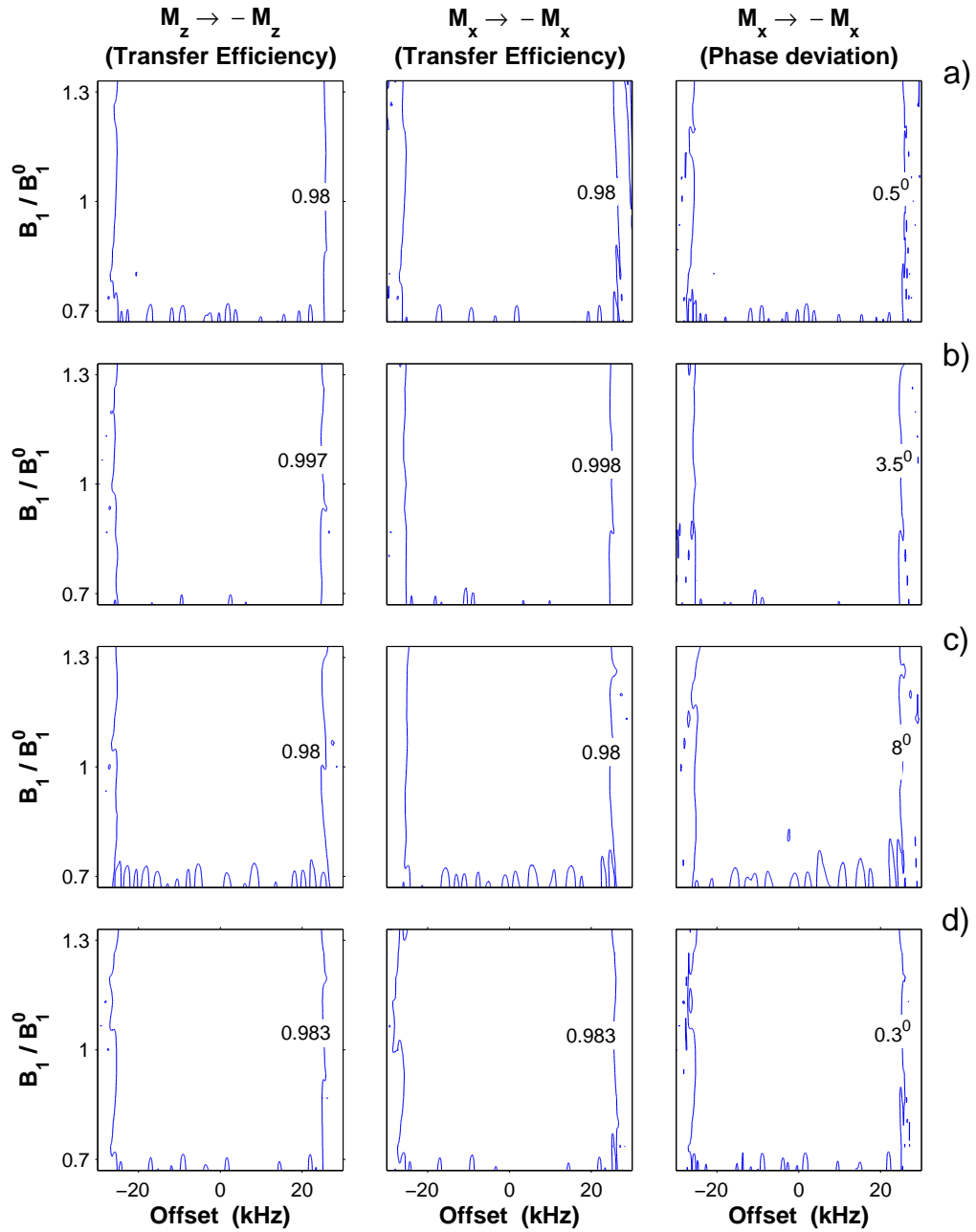


Figure 4.3: (Color online) Theoretical performance of four 180°_{UR} pulses for inversion of magnetization about the y -axis, designed using different algorithms. The first two columns show the transfer efficiency for the labeled transformations relative to ideal or complete transfer. The last column displays phase deviation in degrees relative to the labeled target state. The nominal peak RF amplitude for all the pulses is $B_1^0 = 15$ kHz, optimized to perform over a resonance offset range of 50 kHz and variation in RF homogeneity/calibration of $\pm 33\%$. All pulses are constant amplitude with the exception of pulse b), which deviates from the maximum for less than 10% of the pulse. **a)** constructed from the 1 ms 90°_{PP} pulse of Ref. [51] preceded by its time- and phase-reversed waveform [41], pulse length $T_p = 2$ ms. **b)** algorithm A, $T_p = 2$ ms. **c)** algorithm A, $T_p = 1$ ms. **d)** algorithm A_S , which incorporates the symmetry principle used in a), $T_p = 2$ ms. B_1 is the variable RF amplitude.

Pulse	Algorithm	RF _{nominal} (kHz)	RF _{max} (kHz)	Inhomogeneity optimization	Transformation Error	
					(amplitude)	(phase)
1	A _T	11	15	±10%	< 0.2%	< 2°
2	A _{S,T}	11	15	±15%	< 0.9%	< 0.3°
3	A _{S,T}	10	15	±15%	< 1.5%	< 0.5°
4	A _{S,T}	11	15	±25%	< 2%	< 0.8°

Table 4.1: Four pulses optimized to execute a 180° universal rotation about the y-axis over resonance offsets of 50 kHz and RF field inhomogeneity listed in column 5. All pulses are 2 ms long. For all but 60 μ s, pulse RF is constant at the value RF_{nominal}, increasing to RF_{max} in the middle of the pulse (see Fig. 4.2). Amplitude errors in the transformation are the maximum deviation from the target magnetization over the optimized ranges of resonance offset and RF inhomogeneity, expressed as a percent. Similarly, phase errors represent the maximum deviation from the target phase. Performance of pulses 1 and 4 are shown in more detail in Fig. 4.4.

4.4 Experiment

All experiments were implemented on a Bruker 750 MHz Avance III spectrometer equipped with SGU units for RF control and linearized amplifiers, utilizing a triple-resonance PATXI probehead and gradients along the z -axis. Measurements are the residual HDO signal in a sample of 99.96% D₂O doped with CuSO₄ to a T_1 relaxation time of 100 ms at 298° K. Signals were obtained at offsets between -25 kHz to 25 kHz in steps of 500 Hz. To demonstrate the tolerance of the pulses to RF inhomogeneity/miscalibration, the experiments were repeated with RF amplitude incremented by $\pm 15\%$ and $\pm 25\%$ relative to the nominal maximum RF amplitude for each pulse (15 kHz for pulse 4 of Table 1, 11.26 kHz for Chirp80). To reduce the effects of RF field inhomogeneity within the coil itself, approximately 40 μ l of the sample solution was placed in a 5 mm Shigemi limited volume tube.

4.5 Conclusion

We have presented three optimal control algorithms for the de novo design of universal rotation pulses, applied specifically to inversion. The most noteworthy innovations for NMR spectroscopy are inclusion of the construction principle discovered in [41] and a time-dependent or “floating” limit on the peak RF allowed during the pulse. The new algorithms result in improved performance compared to existing UR pulses constructed as composites of point-to-point pulses. The methodology is very general, and further improvements in the design of robust universal rotation pulses can be anticipated. The new pulses are implemented in the Bruker pulse library and will also be made available for downloading from the website

<http://www.org.chemie.tu-muenchen.de/glaser/Downloads.html>.

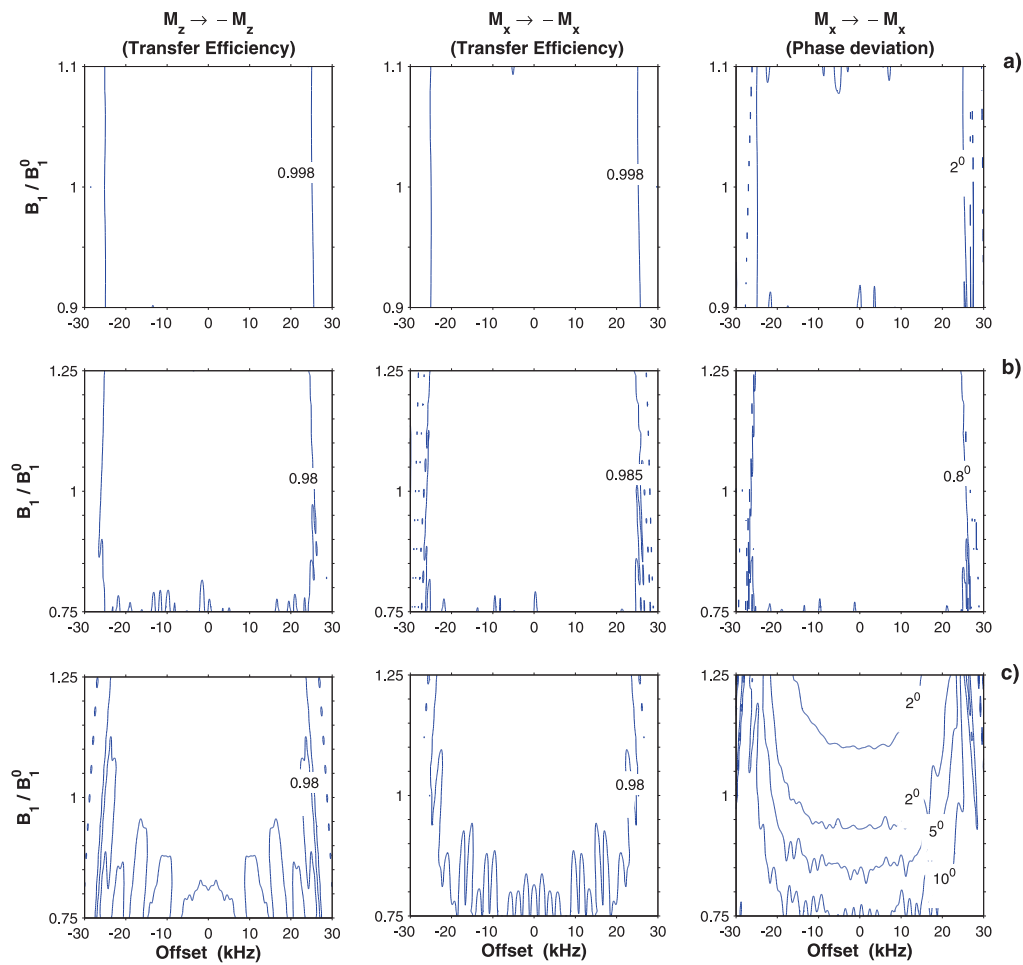


Figure 4.4: (Color online) Similar to Fig. 4.3, but the maximum RF amplitude is allowed to float for a sufficiently short time period, giving the reduced-power pulse in Fig. 4.2. All three pulses are designed to operate over a resonance offset of 50 kHz and a range of variation in RF homogeneity/calibration relative to the ideal B_1^0 , as given in Table 1. **a)** pulse 1 of Table 1, RF tolerance $\pm 10\%$. **b)** pulse 4 of Table 1, RF tolerance $\pm 25\%$. **c)** composite adiabatic refocusing [40] using pulse Chirp80 from the Bruker pulse library [21].

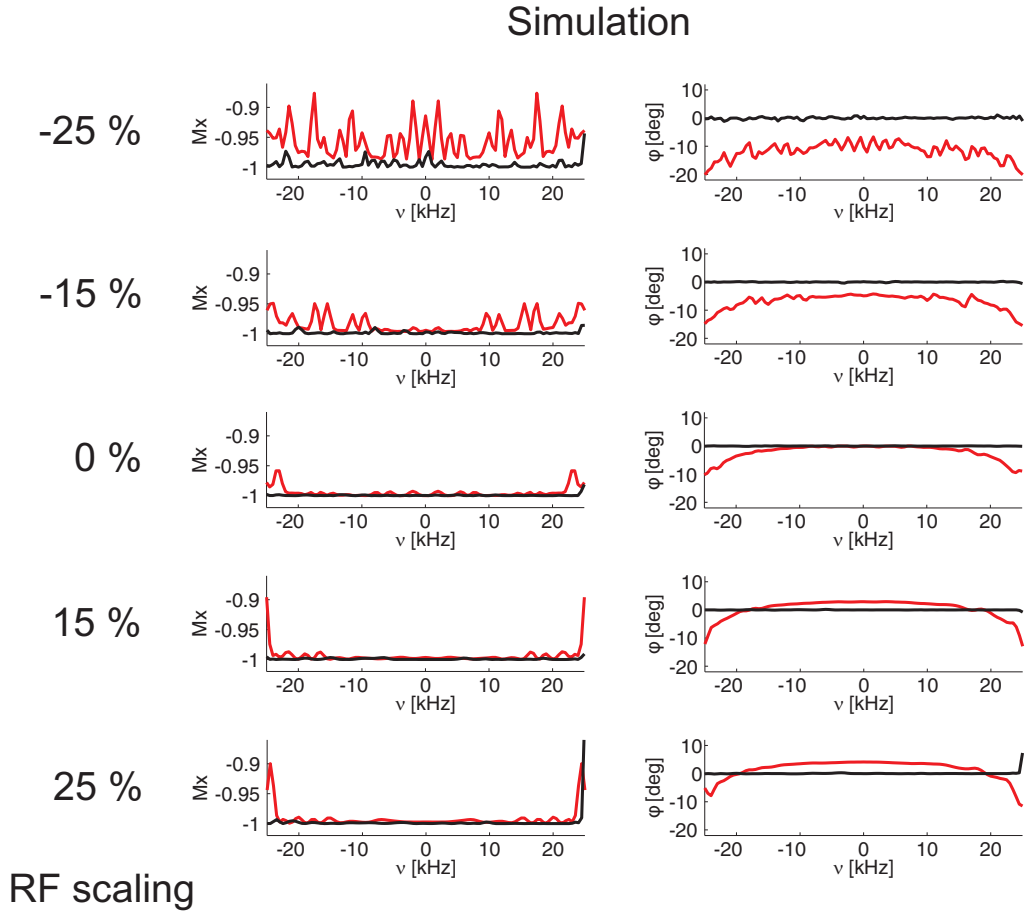


Figure 4.5: (Color online) Further quantitative detail for the $M_x \rightarrow -M_x$ transformation from Fig.4.4b for pulse 4 of Table 1 (black) and Fig.4.4c for Chirp80 (red), plotted for RF scalings of $\pm 15\%$ and $\pm 25\%$ relative to the nominal maximum RF amplitude at 0% (15 kHz, pulse 4 and 11.26 kHz, Chirp80). Theoretical values for the inversion profile are plotted on the left as a function of resonance offset, with phase deviation φ relative to the target $-M_x$ plotted on the right. Adiabatic Chirp80 produces significant phase errors within the bandwidth for all RF scalings, in contrast to the almost ideal performance of the optimal control 180°_{BURBOP} pulse.

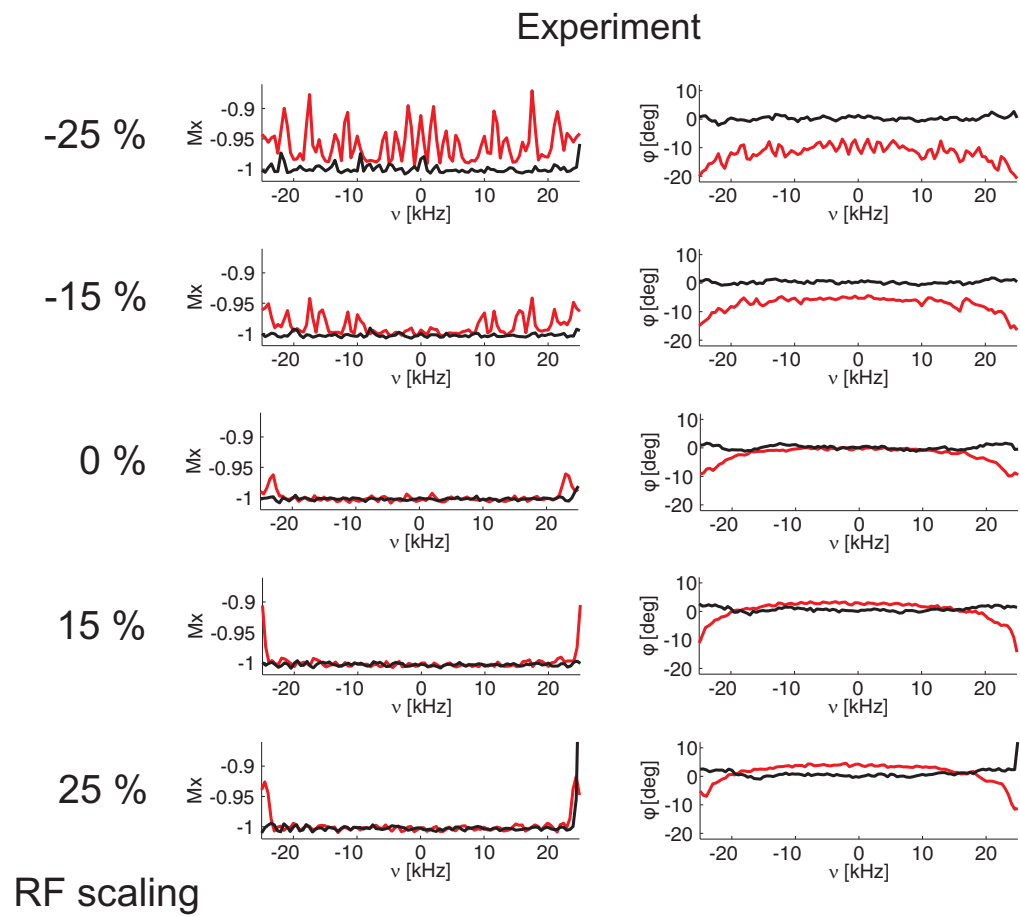


Figure 4.6: (Color online) Experimental measurements of the inversion profile (left) and phase deviation (right) corresponding to the simulations in Fig. 4.5, showing excellent agreement between the experimental and theoretical performance of the pulses.

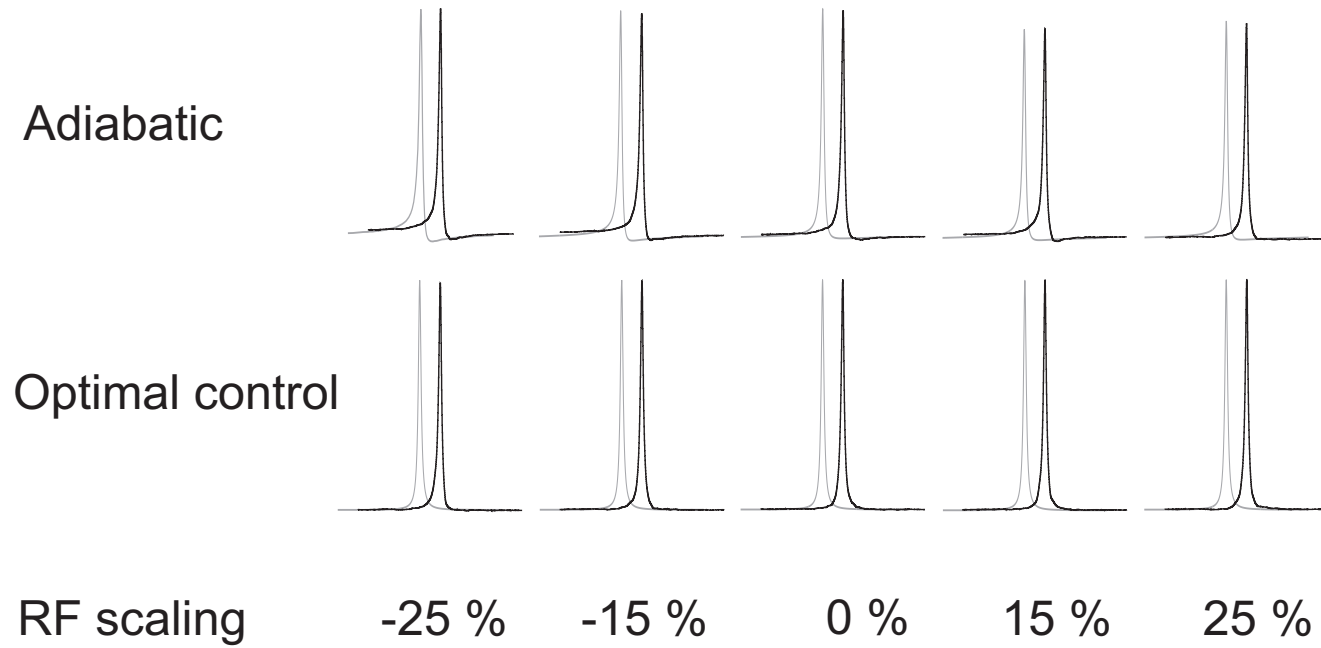


Figure 4.7: Experimental lineshapes (black) comparing optimal control 180_{UR}° pulse 4 of Table 1 and adiabatic Chirp80 at a resonance offset of -25 kHz for RF scalings of $\pm 15\%$ and $\pm 25\%$ relative to the nominal maximum RF amplitude of 15 kHz at 0% . Simulations (gray) are in excellent agreement with the experiments, as already shown in Figures 4.5 and 4.6. Chirp80 produces significant experimental phase errors of 20° , 15° , 9° , 11° , and 5° (reading left-to-right across the RF scalings in the figure) in contrast to the experimental performance of 0.7° , 0.7° , 0.9° , 2.6° , 2.5° for the optimal control 180_{BURBOP}° pulse.

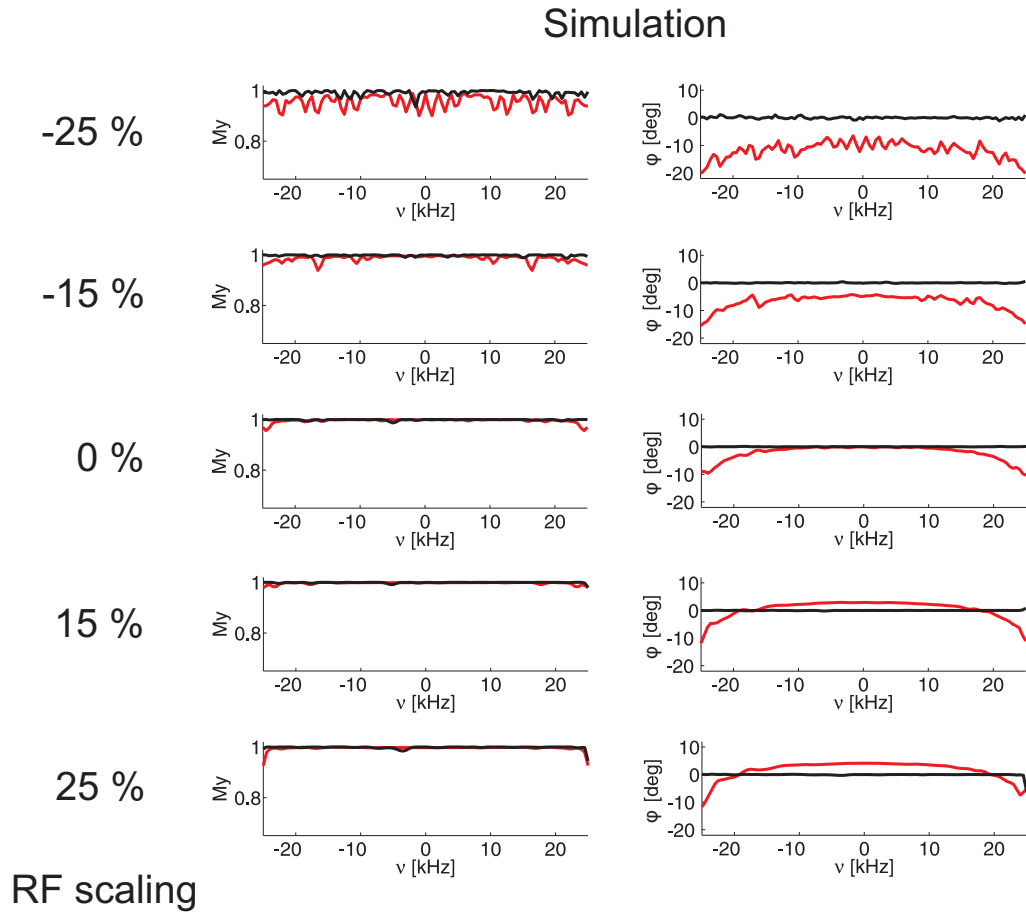


Figure 4.8: (Color online) Further quantitative detail for the $M_y \rightarrow M_y$ transformation for pulse 4 of Table 1 (black) and Fig. 4.4c for Chirp80 (red), plotted for RF scalings of $\pm 15\%$ and $\pm 25\%$ relative to the nominal maximum RF amplitude at 0% (15 kHz, pulse 4 and 11.26 kHz, Chirp80). Theoretical values for the inversion profile are plotted on the left as a function of resonance offset, with phase deviation φ relative to the target M_y plotted on the right. Adiabatic Chirp80 produces significant phase errors within the bandwidth for all RF scalings, in contrast to the almost ideal performance of the optimal control.

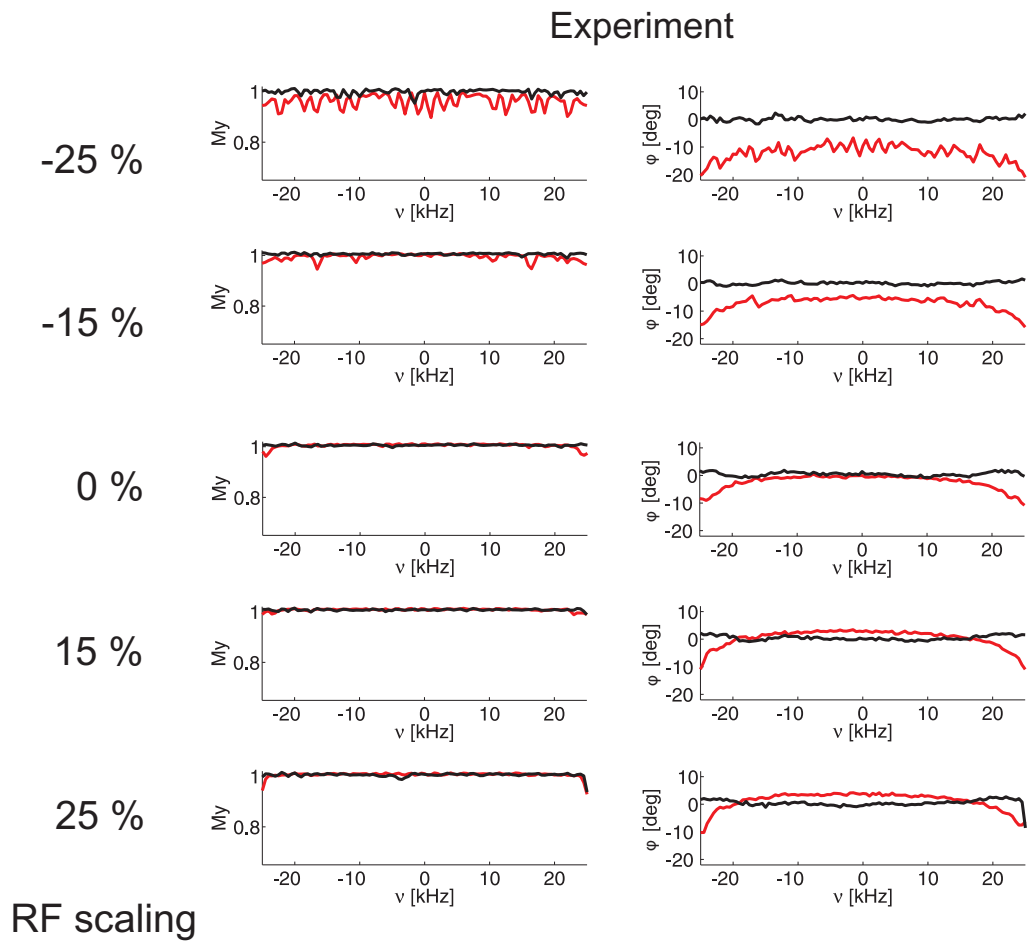


Figure 4.9: (Color online) Experimental measurements of the inversion profile (left) and phase deviation (right) corresponding to the simulations in Fig. 4.8, showing excellent agreement between the experimental and theoretical performance of the pulses.

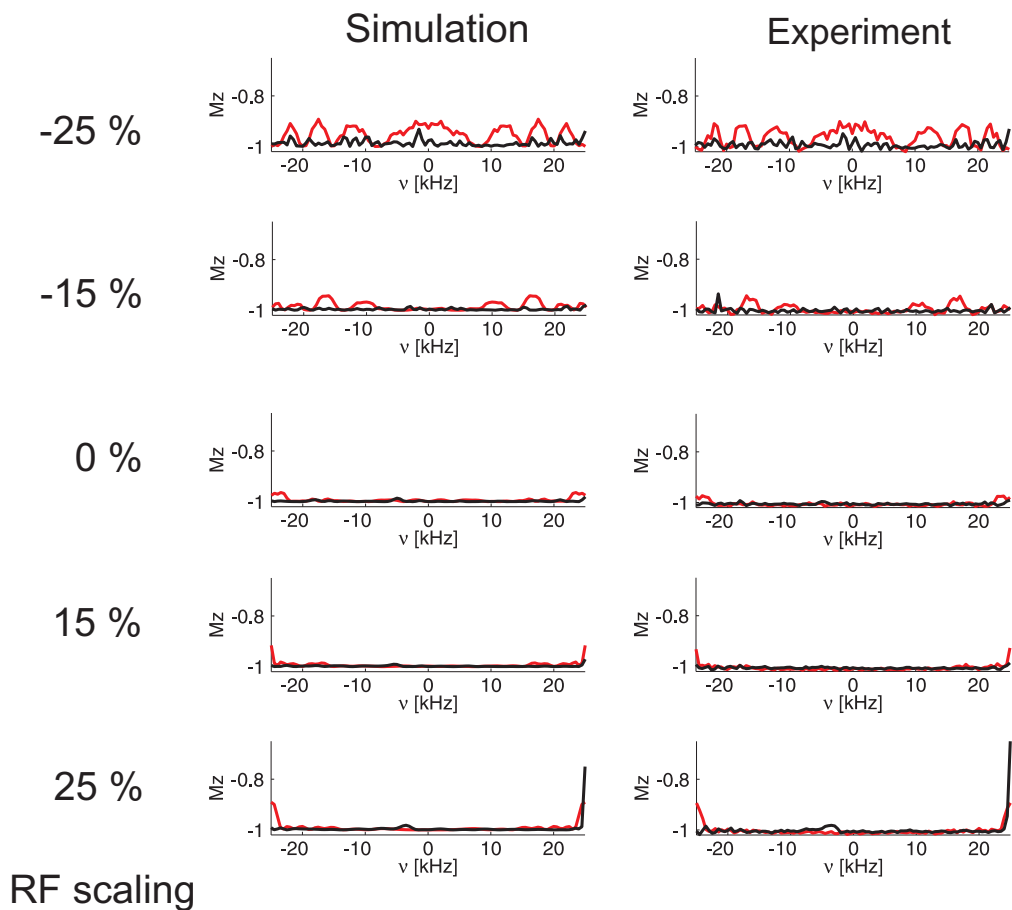


Figure 4.10: (Color online) Further quantitative detail for the $M_z \rightarrow -M_z$ transformation from Fig. 4.4b for pulse 4 of Table 1 (black) and Fig. 4.4c for Chirp80 (red), plotted for RF scalings of $\pm 15\%$ and $\pm 25\%$ relative to the nominal maximum RF amplitude at 0% (15 kHz, pulse 4 and 11.26 kHz, Chirp80). Theoretical and experimental values for the inversion profile are plotted as a function of resonance offset. Experimental measurements of the inversion profile corresponding to the simulations, showing excellent agreement between the experimental and theoretical performance of the pulses.

Chapter 5

Band-selective excitation pulses that accommodate relaxation and RF inhomogeneity

5.1 Introduction

This chapter is a part of an article [65] submitted to Journal of Magnetic Resonance. Frequency-selective pulses have widespread utility in magnetic resonance and have motivated significant efforts towards their design [66–111]. In many useful cases, the resulting methodologies can achieve the best approximation to the ideal rectangular profile for spin response as a function of frequency offset.

However, in all of these approaches to pulse design, performance criteria that can be included in the design protocol are restricted either by analytical procedures of highly specific scope or by numerical methods that are limited by the efficiency of the optimizations employed. As a result, pulse response is typically optimized only for the nominal ideal RF pulse values. In addition, although the length of pulses required for narrow-band applications can significantly reduce their effectiveness when relaxation times are comparable to the pulse length [112, 113], the solution to the problem—selective pulses which are less sensitive to relaxation effects—can also be demanding for standard design methods [97, 114–118].

To make these design challenges tractable, the space of possible pulse shapes is often reduced by forcing the solution to be a member of a particular family of functional forms (for example, finite Fourier series). Thus, potentially, there are important solutions that are missed. Over the past decade, we have shown optimal control theory to be an efficient and powerful method that can be applied to a wide range of challenging NMR pulse design problems without restricting the space of possible solutions [48–53, 56, 57, 119–129]. It is capable of designing broadband pulses [52] and selective pulses [130, 131] that are simultaneously tolerant to RF inhomogeneity and relaxation effects, which we develop further in the present chapter.

5.2 Selective pulse design

Optimal control (including similar, related optimization procedures) was originally introduced into magnetic resonance for the design of band-selective pulses, primarily for imaging [43, 44, 47, 132–135]. It was quickly supplanted by the efficient Shinnar-LeRoux (SLR) algorithm [82–85, 136], which establishes a correspondence between frequency-selective pulse design and digital filter design. There are fast, non-iterative algorithms for the ideal filter and, hence, the ideal pulse. Unfortunately, the algorithm does not accommodate additional criteria, such as tolerance to RF inhomogeneity (included in some of the earliest optimal control-related approaches [132, 134]) or relaxation effects. In addition, the most applicable and widely used form of the algorithm derives pulses which produce a specific linear phase dispersion in the spectral response. Pulses producing no phase dispersion, suitable for spectroscopy, are more problematic for the SLR algorithm.

We first provide an overview of well-known issues relevant to selective pulse design, since there is considerably less freedom in the choice of parameters compared to broadband pulses. For example, in designing broadband pulses, we have shown [122] there is at best only a marginal relation between the maximum amplitude, RF_{\max} , of a pulse and the achievable excitation or inversion bandwidth, as long as the pulse length, T_p , is allowed to increase sufficiently. Alternatively, increasing RF_{\max} for a given T_p can improve performance for a given bandwidth or increase the bandwidth. There can also be innumerable broadband pulses that provide approximately equal performance for a given RF_{\max} , T_p , and bandwidth.

Selective pulses are far more constrained, with a well-known relation between the selective bandwidth and T_p , and much tighter limits on the choice of RF_{\max} for a given product of bandwidth and T_p [136]. We provide only a simple overview of the optimal control methodology, emphasizing the modifications necessary for the present chapter. The basic algorithm for optimizing pulse performance over a range of resonance offsets and RF inhomogeneity is described fully in [48]. Details related to incorporating relaxation [52] and specific dispersion in the phase of the final magnetization [45, 50, 53], which we refer to as the phase slope, are provided in the associated references.

5.2.1 Phase slope

Following the Chapter 3, values of the phase slope, R , [53] at each offset characterize the net phase dispersion that accumulates during a pulse of length T_p . The phase slope is defined relative to the net precession of transverse magnetization that would be produced solely by chemical-shift evolution during the same time interval, T_p . A pulse that produces focused magnetization of fixed phase for all spins in the offset range of interest would have constant $R = 0$ (i.e., a self-refocused pulse). Many selective pulses are symmetric, $R = 1/2$ pulses [43, 72, 91, 93, 94, 136]. The symmetry of the resulting pulse provides an advantage in the development of various algorithms used in selective pulse design, such as SLR, inverse scattering [86, 91], polychromatic [93], and stereographic projection [94]. In fact, the standard form of the SLR algorithm [136] can only generate linear phase of this value. Sophisticated algorithms allowing for more general phase in selective pulses are described in the literature [90, 137, 138], but they are specific to this particular performance factor and cannot include tolerance to variations in other experimentally important parameters.

By contrast, including additional performance criteria, such as a general phase response, is straightforward for optimal control. Initial magnetization $\mathbf{M}(t_0)$ is driven by

the RF controls to a final magnetization \vec{F} that is defined for each resonance offset in the desired range. To excite transverse magnetization of linear phase slope R , we consider target states for each offset $\Delta\nu$ in the excitation bandwidth of the form [53]

$$\vec{F} = [\cos(\varphi), \sin(\varphi), 0] \quad (5.1)$$

Choosing $\varphi = R \Delta\nu T_p$ gives a linear phase slope, but any function can be considered to define a useful target phase, such as quadratic or higher order.

Selective excitation most simply requires changing the target to $\vec{F} = [0, 0, 1]$ for offsets outside the desired bandwidth. However, since the ideal rectangular offset response can not be excited by a finite-length pulse, there must be a transition connecting the excitation frequencies to the nulled frequencies. This is typically defined in terms of design parameters for finite impulse response (FIR) filters. An overview of the issues relevant to our optimal control implementation follows.

5.2.2 Selective pulses as digital filters

For design conditions employing ideal RF in the absence of relaxation, selective pulse performance is completely determined by the desired passband width B , pulse length T_p , transition width W joining the passband and stopband, and residual signal fluctuation or ripple δ_1 and δ_2 about the ideal target amplitude for the passband and stopband, respectively.

The passband frequency ν_p and stopband frequency ν_s are defined where the magnitude of the magnetization response becomes less than the associated fluctuations $1 - \delta_1$ and $|\delta_2|$, as illustrated in Fig. 5.1 (adopted from Ref. [136]). The frequency where the amplitude drops to one-half is approximately the average of these two frequencies. The full width of the filter is defined as twice this value, giving a bandwidth $B = \nu_s + \nu_p$ and a fractional transition width $W = (\nu_s - \nu_p)/B$.

More specifically (and again emphasizing the design conditions stated at the beginning of the section), selective pulse performance is constrained by relations for optimal FIR filters of the form [139]

$$WT_p B = f(\delta_1, \delta_2), \quad (5.2)$$

in terms of an empirically derived function $f(\delta_1, \delta_2)$. For a given value of $f = WT_p B$, smaller (larger) δ_1 gives larger (smaller) δ_2 . Alternatively, for fixed δ_1 or fixed δ_2 , values of f increase as δ_2 or δ_1 , respectively, decrease. Flexibility in selective pulse design is thus purchased at the cost of trade-offs among bandwidth, pulse length, transition width, and ripple amplitudes. Choosing any four of the set determines the fifth.

This relation appears to have been little used in the spectroscopic community. Although the precise form of the function $f(\delta_1, \delta_2)$ holds only for $R = 1/2$ pulses, we have found it to be a useful qualitative indicator for more general R . One important implication is that pulse performance for a given absolute transition width $BW = \nu_s - \nu_p$ can be made independent of the passband width, B . Fixed T_p results in the same performance in terms of residual signal (ripple) for different B as long as BW is constant. This was observed empirically and noted in [111]. We thus use Eq. 5.2 to inform our optimal control design.

5.2.3 Optimal control

The approximation to the ideal rectangular frequency response profile, as illustrated in Fig. 5.1, can be readily obtained using a variety of methods—among them, the Parks-McClellan (PM) algorithm for linear-phase FIR digital filters [139]. After calculating the

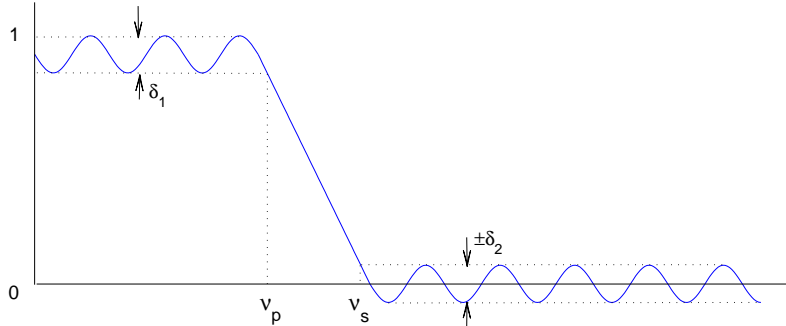


Figure 5.1: (Color online, Adapted from Ref. [136]) A finite length selective pulse can only approximate the ideal rectangular frequency response. Residual signal or ripple amplitude in the selected frequency spectrum (passband) is denoted by δ_1 , with δ_2 representing the ripple over the frequency range where the signal should be nulled (stopband). The positive frequencies ν_p and ν_s define the passband and stopband, respectively. The plotted response is symmetric about the zero frequency.

PM polynomial, the standard SLR algorithm effectively inverts the frequency response to produce a linear phase ($R = 1/2$) RF pulse. The equivalent optimal control approach would be to use the polynomial response function as the target response and efficiently modify the RF controls to achieve the allowed performance.

However, as noted already, the target response derived using the PM algorithm applies only to $R = 1/2$, using the ideal RF amplitudes, in the absence of relaxation. More significantly, optimal control does not need to know the polynomial response. One can simply define the ideal passband/stopband frequency response, and the algorithm will find the response allowed by the particular choice of bandwidth, pulse length, and transition width. Different functional forms can be defined for the response in the transition region to provide additional flexibility. The response at each frequency can also be given weights to fine-tune the final excitation profile.

We now proceed with the design of more robust selective excitation pulses. In what follows, we let the frequency response to the pulse (ie, the target function) be undefined in the transition region. The pulse has the flexibility to do anything it wants there. An important addition to the algorithm is an adjustable weight function, which changes the weight for each particular offset depending on the deviation of intermediate results from the desired performance. During a given iteration, if the deviation of magnetization from the target for a particular offset is larger than the allowed ripple amplitude, then the weight for this offset increases; otherwise it decreases.

5.3 Results and Discussion

We present several examples illustrating the advantages of selective excitation by optimized pulses (SEBOP). As discussed, possible performance improvements include increased tolerance to RF inhomogeneity and compensation for relaxation effects.

5.3.1 Tolerance to RF inhomogeneity

As a first example, consider a representative imaging pulse from Ref. [136], designed using the SLR algorithm to selectively excite a bandwidth $B = 2$ kHz with a transition width $W = 0.18$, pulse length $T_p = 4$ ms, and stopband ripple $\delta_2 = 1\%$, resulting in a passband ripple $\delta_1 = 1\%$ from the relation referenced in Eq. 5.2. The amplitude-modulated pulse and its theoretical spectral response are shown in Fig. 5.2. RF inhomogeneity in the range $\pm 20\%$ results in signal variations in the passband of $\sim 10\text{--}15\%$.

Tolerance to RF inhomogeneity is considerably more difficult to achieve for selective compared to broadband pulses, due to the much tighter constraints required for selectivity. Nonetheless, allowing $\pm 20\%$ pulse miscalibration in the optimal control algorithm results in the two-component amplitude- and phase-modulated SEBOP pulse shown on the right in Fig. 5.2. For an average power equal to 95% of the SLR pulse average power and the same phase slope $R = 1/2$, SEBOP reduces passband signal variation due to the specified RF inhomogeneity to less than $\sim 5\%$. Stopband ripple, which corrupts image fidelity due to signal outside the selected frequencies (out-of-slice signal), is also reduced considerably.

In contrast to imaging, selective pulses for high resolution NMR are of greatest utility if they are refocused pulses, which produce no phase gradient in the spectrum (phase slope $R = 0$ in our terminology). This will be the case for all the examples which follow.

5.3.2 Compensation for relaxation and RF inhomogeneity

The algorithm for generating relaxation compensated broadband pulses (RC-BEBOP) has already been developed [52]. It only needs inclusion of the modified target functions described in Section 5.2.1 for application to selective pulses (RC-SEBOP). The primary result of that work is that substantial signal gains are possible relative to expected losses from short T_1 , T_2 by finding trajectories for the transformed magnetization that minimize these losses, even if this requires a longer pulse length. Relaxation losses are minimized by keeping spins near the z -axis and orienting them so that all offsets can be transformed to the transverse plane in a very short time at the end of the pulse. This solution not only mitigates the effects of transverse relaxation, but short T_1 becomes an advantage due to repolarization of z -magnetization during the relatively long time the spins are aligned close to the longitudinal axis. The net affect is that almost all the RF power is applied at the end of our relaxation compensated pulses [52]. This is fortunately also consistent with a particular family of solutions for broadband $R = 0$ (refocused) pulses [53].

There are also solutions for refocused selective excitation pulses [111] that employ significant RF power throughout the pulse and therefore do not lend themselves to relaxation compensation. On the other hand, these pulses do an excellent job of minimizing the residual off-axis magnetization in both the passband and stopband. Consistent with this result, we find empirically that minimizing relaxation losses for selective pulses competes with minimizing residual off-axis magnetization. The trajectories that reduce relaxation effects are not compatible with those that achieve good refocusing. We therefore consider a strategy that maximizes x -magnetization in the passband, minimizes it in the stopband, i.e., the standard procedure, but removes any explicit restrictions on residual y -magnetization. This allows the optimal control algorithm to emphasize relaxation compensation and find solutions with considerably enhanced performance compared to those that give highest priority to minimizing the y -component. As we will show, this undesirable residual magnetization can be eliminated after the pulse without significantly affecting performance.

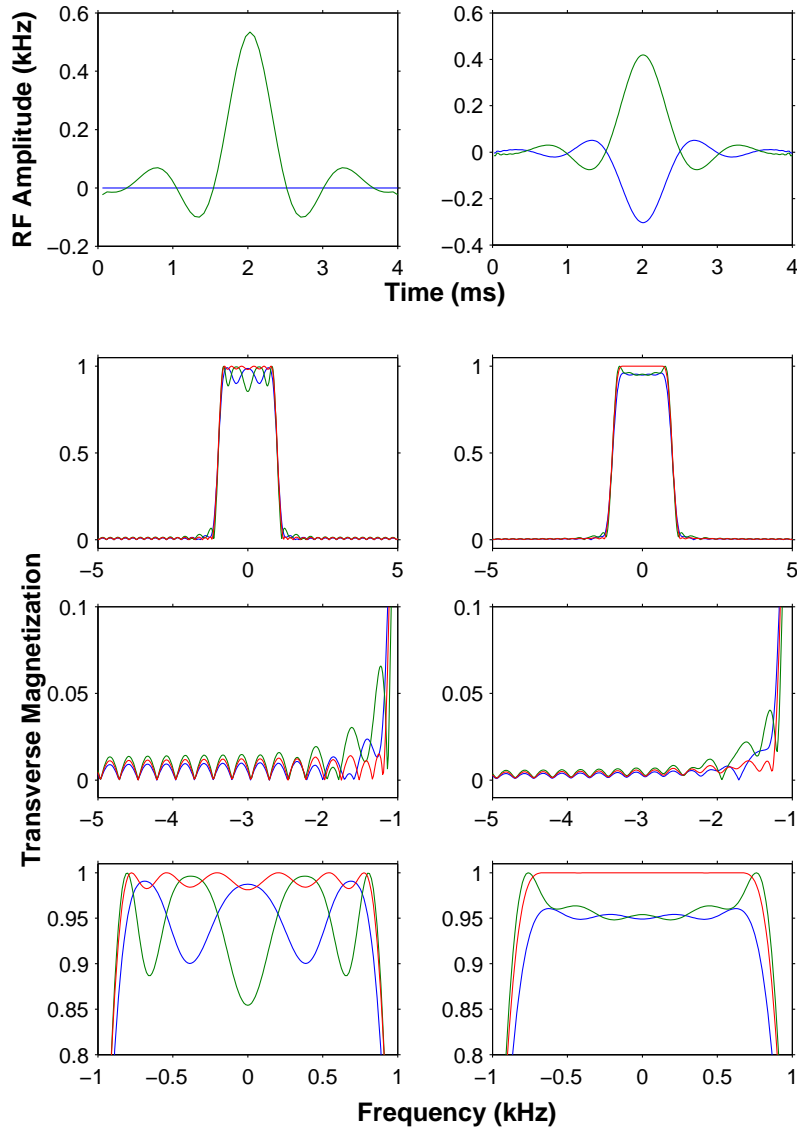


Figure 5.2: (Color online) Panels on the left show an amplitude modulated selective pulse produced by the SLR algorithm, which can not explicitly incorporate tolerance to RF inhomogeneity, followed below by its theoretical frequency response, a magnified view of the stopband, and a magnified view of the passband. Values of the simulated RF miscalibration/inhomogeneity are -20% (blue), 0% (green), and $+20\%$ (red). Similarly, panels on the right show the x-phase (blue) and y-phase (green) RF components of an amplitude- and phase-modulated SEBOP pulse, followed by its frequency response. Design parameters and average power (see Section 5.3.1) are the same for both pulses.

Excitation profile effects

In addition to causing signal losses, relaxation can also degrade the uniformity of the excitation profile [112]. SLURP pulses [114] were developed specifically to obtain more uniform response over the selected bandwidth while accepting attenuation due to short T_1, T_2 . SLURP-1 pulses address the particular case $T_1 = T_2$, and were derived for various values of the ratio T_2/T_p .

For the demanding case $T_p = T_1 = T_2 = 1$ ms, theoretical performance of SLURP-1 is compared to RC-SEBOP in Fig. 5.3 for RF miscalibrations of -10% , 0% , and $+10\%$, displayed left to right. For the ideal RF shown in the middle panel, RC-SEBOP provides a signal gain of 60% , uniformly preserving greater than 90% of the x -magnetization over the optimized bandwidth of 4 kHz, in spite of short T_1, T_2 equal to the pulse length. It is relatively insensitive to RF inhomogeneity of $\pm 10\%$. In all cases, there is improved signal suppression from M_x magnetization in the stopband, and a narrower transition width.

Analogous investigations have optimized relaxation-compensated pulses by applying simulated annealing to RF waveforms represented using finite Fourier series (~ 8 frequency components or less) and no compensation for RF inhomogeneity [115,118]. They achieve signals of $< 80\%$ for the case $T_p = T_1 = T_2$ over a less selective bandwidth than obtained here. Some of our performance gains may be due to a more efficient optimization procedure that does not restrict the solution space. However, we expect the largest gains are due to the flexibility of allowing residual y -magnetization, M_y , which can be quite large, as shown in the bottom panel of Fig. 5.3. This is easily eliminated, as shown later, and allows a much more ideal, rectangular excitation profile than previously considered possible for short T_1, T_2 [112], with minimal loss of signal. Alternatively, if we choose to minimize the residual M_y during the optimization, this requires trajectories that sacrifice signal enhancement and selectivity of the passband, consistent with the other cited studies.

Excitation using small time-bandwidth product pulses

A simple strategy for reducing relaxation effects is to reduce the pulse length, but according to Eq. 5.2, achieving acceptable performance for a narrow excitation bandwidth then becomes more problematic. A given time-bandwidth product requires trade-offs in the sharpness of the excitation profile (transition width) and the signal variation (ripple) in both the passband and the stopband. Still, one can optimize performance for a desired low value of the time-bandwidth product, as accomplished in the SNOB family of pulses [97]. Including relaxation compensation beyond what is accomplished by a short pulse length alone and including tolerance to RF inhomogeneity provide additional opportunities for improved performance.

For e-SNOB, $T_p = 1$ ms, selective bandwidth ± 1.5 kHz, we designed a RC-SEBOP pulse incorporating relaxation times $T_1 = T_2 = T_p$ and tolerance to RF inhomogeneity of $\pm 10\%$. Pulse shapes are shown in Fig. 5.4 along with theoretical performance. Signal gains of a factor of 2 are obtained with the relaxation-compensated pulse, with a sharper excitation profile and improved suppression of M_x magnetization in the stopband. To minimize relaxation losses, RC-SEBOP delivers most of its RF power at the end of the pulse. As in the previous example, these enhanced performance features are purchased at the cost of a larger residual M_y compared to e-SNOB. In the next section, we present methods for selecting only the desired M_x magnetization while maintaining the performance advantages of RC-SEBOP.

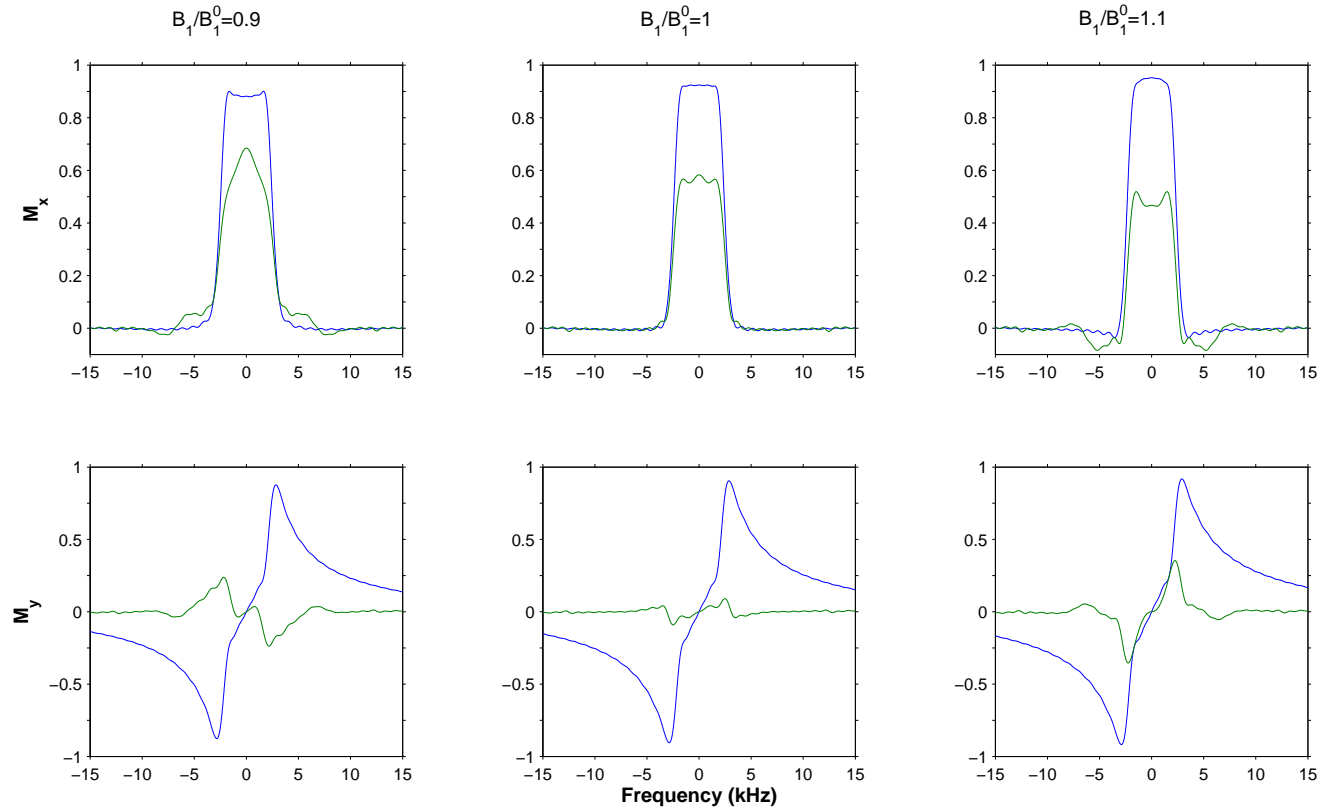


Figure 5.3: (Color online) Excited magnetization M_x (top panels) and M_y (bottom panels) is plotted as a function of resonance offset for SLURP-1 (green) and RC-SEBOP (blue) for $T_p = T_1 = T_2 = 1$ ms and RF inhomogeneity/miscalibration of -10% , 0% , $+10\%$ reading left to right. Despite these fast relaxation rates, RC-SEBOP preserves $>90\%$ of the desired M_x while achieving a nearly rectangular profile that is relatively insensitive to $\pm 10\%$ RF inhomogeneity over the optimized excitation bandwidth of 3 kHz. The signal gain on resonance for the nominal ideal RF is a factor of 1.6. Minimal relaxation losses are achieved by allowing large residual M_y , particularly in the stopband. This unwanted signal can be subsequently eliminated without affecting performance, as described in the text (see Fig. 5.5).

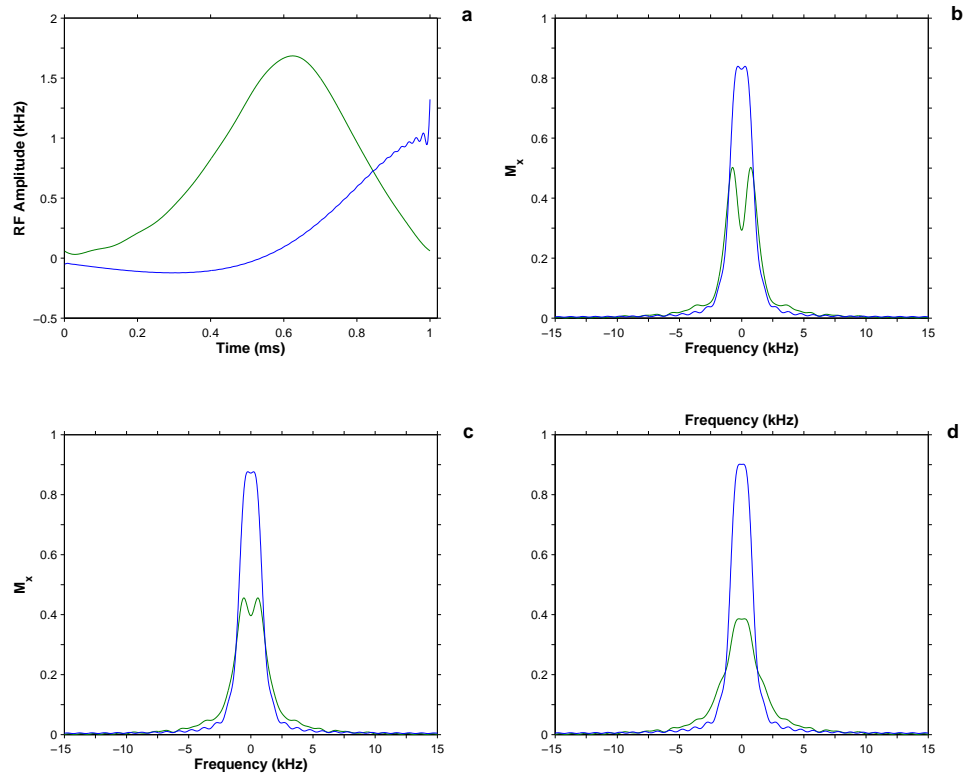


Figure 5.4: (Color online) Selective pulses eSNOB (green) and RC-SEBOP (blue) of length $T_p = 1$ ms are plotted in panel a. RC-SEBOP utilizes less RF power, which is applied primarily at the end of the pulse to reduce relaxation losses, as described in the text. Panels b, c, and d show the frequency response of the pulses for RF miscalibration/inhomogeneity of -10% , 0% , and $+10\%$, respectively, for $T_1 = T_2 = 1$ ms. RC-SEBOP significantly reduces relaxation losses and provides a sharper and more rectangular selectivity profile over the designed excitation bandwidth of 3 kHz. The signal gain in this example is a factor of 2.

5.4 Experimental

All the selective pulses considered so far produce significant residual M_y magnetization in the passband at non-ideal RF calibration. Methods for removing this unwanted signal therefore have more general applicability.

To destroy undesired M_y after selective excitation in a single-acquisition experiment, a hard 90_{-y}° flip-back pulse can be applied to store M_x along the z -axis. A gradient pulse is then employed to dephase the M_y component, followed by a hard 90_y° pulse for acquisition of the signal due to M_x . This “crusher” sequence, implemented in Fig. 5.5a as a more general phase-cycled sequence (to be discussed below), was first tested for the case of unlimited-bandwidth hard pulses by applying the hard pulses on resonance. The transmitter frequency was shifted only for the RC-SEBOP pulse to measure its off-resonance performance. This sequence is insensitive to the actual T_2 of the sample, since there is minimal relaxation during the short hard pulses and no T_2 relaxation of magnetization stored along the z -axis during the gradient pulse. In addition, for typical samples with $T_1 \gg T_2$, there are minimal T_1 effects as a result of the sequence. However, for very short T_1 , repolarization of stopband magnetization during the gradient pulse can lead to slightly more M_x magnetization in the stopband than expected from the theoretical selectivity profile of RC-BEBOP, previously illustrated in Fig. 5.4.

To eliminate extra stopband signal in cases where T_1 is too short for ideal performance of the original crusher sequence, it can be phase-cycled as shown in the figure. The two acquisitions add constructively in the passband. Repolarization at stopband frequencies leads to $+z$ -magnetization after the first hard pulse in each cycle which is canceled by addition of the two acquisitions after the second hard pulse. As a general strategy, this sequence works very well for the case of ideal hard pulses with no bandwidth limitations. It therefore also works well over a bandwidth of ~ 8 kHz for a 25 kHz hard pulse, where the performance of the hard pulse is sufficiently ideal, and may be useful for applications that require only a relatively narrow range of stopband frequencies compared to the available RF amplitude of the hard pulse.

More realistically, all pulses have to be applied at the same transmitter frequency to measure the performance of the sequence at larger resonance offsets. The effective field of the hard pulses will then have a significant z -component, and the y -magnetization will no longer remain untouched. However, the gradient still dephases the transverse magnetization remaining after the first hard pulse. To a first approximation, there is only z -magnetization prior to the second hard pulse, and the phase cycle produces transverse components of opposite sign that cancel on addition.

Experimental off-resonance performance of RC-SEBOP and the phase-cycled crusher sequence is demonstrated in Fig. 5.6 for the residual HDO signal in a sample of 99.96% D_2O , doped with $CuSO_4$ to relaxation times of $T_1 = 1.345$ ms and $T_2 = 1.024$ ms at 298° K. Signals were obtained at offsets between -15 kHz to 15 kHz in steps of 200 Hz. The sequence was first implemented using 10 μs hard pulses, which resulted in stopband signal of 5% relative to the centerband. It was then fine-tuned by increasing the hard-pulse length to 10.68 μs in the first cycle. The resulting selectivity profile is in very good agreement with the simulations for eSNOB and RC-BEBOP performance in Fig. 5.4. We obtain a signal of 0.83 on resonance using the nominal ideal RF values for RC-SEBOP compared to the theoretical value 0.89. All values are relative to an ideal signal of 1 for the case of no relaxation. The small disagreement between experiment and simulation can be attributed to RF inhomogeneity/miscalibration in the flip-back pulse, which will leave some small fraction of the desired passband signal in the transverse plane to be destroyed by the gradient.

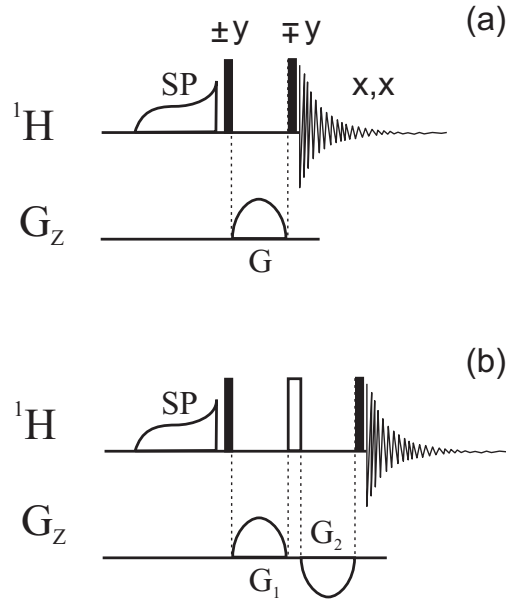


Figure 5.5: (a) Phase-cycled sequence consisting of excitation by selective pulse (SP), hard 90° pulse, gradient pulse, hard 90° pulse, and acquisition. The sequence is designed to eliminate residual y -magnetization produced either by standard selective pulses in the presence of RF inhomogeneity or produced by design in the case of RC-SEBOP (b) a single-acquisition sequence designed as an alternative to (a).

Since relaxation compensation functions by keeping spins close to the z -axis as long as possible during the pulse, the performance of RC-SEBOP is not highly specific to particular T_1 , T_2 values. Although optimized for $T_1 = T_2 = 1$ ms, the $T_p = 1$ ms RC-SEBOP pulse of Fig. 5.4 performs well for much shorter relaxation of $T_1 = 708 \mu\text{s}$ and $T_2 = 527 \mu\text{s}$, as shown in Fig. 5.7. A signal of 0.75 is obtained on resonance using the nominal ideal RF values for the pulse and the phase-cycled crusher sequence compared to a theoretical value of 0.81 for on-resonance excitation by RC-SEBOP alone. The pulse could also be optimized for faster relaxation to improve performance further. A signal of 0.68 is obtained using the single-acquisition sequence of Fig. 5.5b.

If a single-acquisition sequence is preferred, the sequence of Fig. 5.5b can be used to more completely eliminate stopband signal for the case of short T_1 . The first gradient is followed by a hard 180°_y pulse. M_z is flipped to $-z$ where any additional magnetization repolarized during the first gradient pulse can relax to zero during a subsequent delay of the same length as the first. This extra delay can also be used for additional dephasing of unwanted transverse magnetization by a gradient pulse of opposite sign to the first gradient. The sequence ends with a hard 90°_y pulse followed by signal acquisition. However, performance depends more sensitively on any RF inhomogeneity or miscalibration of the hard pulses, since there are now two opportunities to destroy leftover transverse magnetization due to imperfect rotation and storage along the z -axis. Off-resonance effects of the hard pulses, which now include a 180° pulse, further degrade performance. The scheme is included as an option for narrow passband applications. In addition, one might want to explore possibilities using broadband, shaped 90° and 180° pulses. These could also be incorporated into a simpler sequence that eliminates the gradient in Fig. 5.5a and cycles according to $[\pm y, y, \text{Acq}(x, -x)]$.

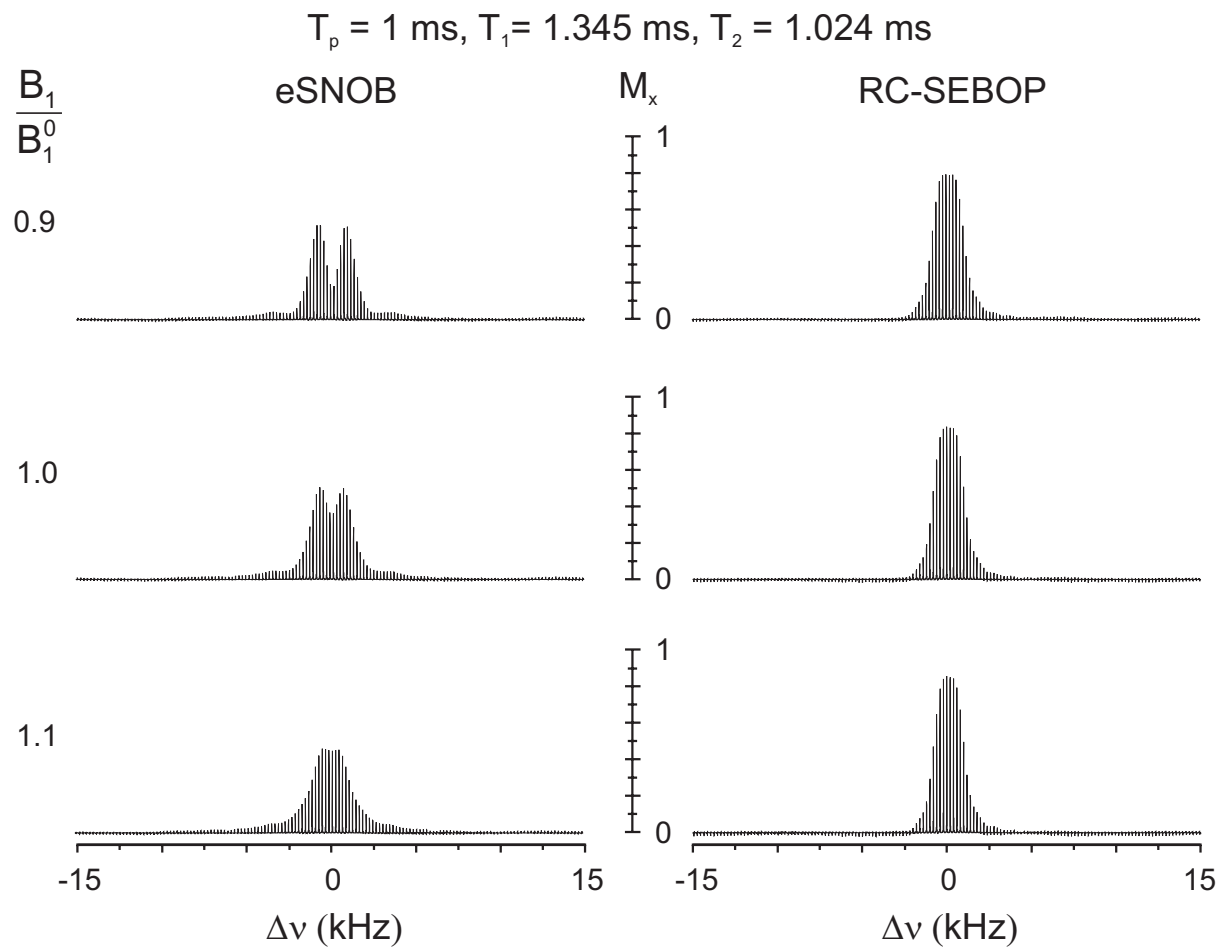


Figure 5.6: Experimental selectivity profiles of RC-BEBOP (right) and eSNOB (left), pulse length $T_p = 1 \text{ ms}$, using the phase-cycled crusher sequence of Fig. 5.5a applied to a strongly relaxing sample with $T_1 = 1.345 \text{ ms}$ and $T_2 = 1.024 \text{ ms}$. Further experimental details are in the text. Results are shown for three values of the RF calibration relative to the ideal value B_1^0 for each pulse, showing insensitivity of RC-SEBOP to RF miscalibration of $\pm 10\%$. Passband signal gains of a factor of 2 are obtained with RC-SEBOP compared to eSNOB. The combined sequence for relaxation compensation and elimination of M_y preserves 83% of the initial magnetization on-resonance for the case $B_1/B_1^0 = 1$ compared to the theoretical value of 89% for M_x alone shown in Fig. 5.4.

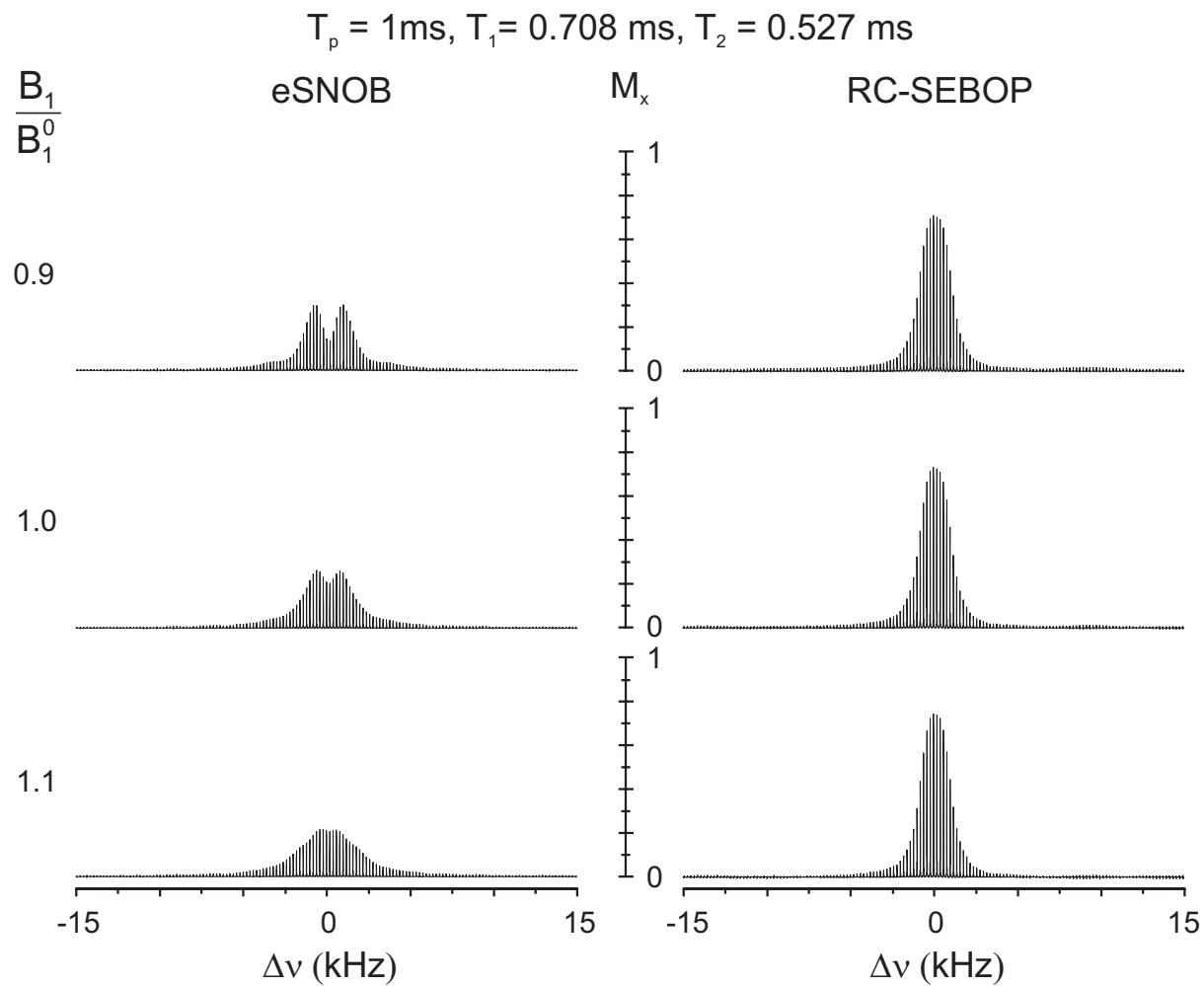


Figure 5.7: Same as Fig. 5.6, but applied to a faster-relaxing sample with $T_1 = 708\ \mu\text{s}$, $T_2 = 527\ \mu\text{s}$. Although RC-SEBOP was optimized for $T_1 = T_2 = T_p = 1\ \text{ms}$, it provides excellent resistance to relaxation for much shorter values, preserving 75% of the initial magnetization on-resonance for the case $B_1/B_1^0 = 1$.

5.5 Conclusion

Pulses which provide robust and enhanced performance despite RF inhomogeneity or miscalibration and relaxation effects are highly desirable. The optimal control approach to designing refocused selective excitation pulses with these compensatory mechanisms has been presented. The examples considered the standard selectivity profile comprised of a passband, transition region, stopband, and variations (ripple) in signal uniformity, as illustrated in Fig. 5.1. Constraints and trade-offs in the performance among these fundamental parameters were emphasized. In particular, we found relaxation compensation and null excitation of magnetization in the stopband to be competing goals. Considerable improvements in selectivity and relaxation-compensation for short T_1 , T_2 were obtained by allowing residual unrefocused magnetization in both the passband and stopband. This residual magnetization can be readily eliminated without significantly diminishing performance using additional pulse elements.

Chapter 6

Time optimal pulses for multiple-spin coherence transfer

6.1 Introduction

This chapter is a part of an article [140]. The control of spin dynamics in chains of coupled spins-1/2 is a topic of both theoretical and practical interest [141–152]. On the one hand, the use of spin chains is considered for the efficient transfer of information in future quantum computing devices [153, 154]. On the other hand, coherence transfer between remote spins is the basis of many multi-dimensional experiments for the assignment of complex spectra [155–157] in nuclear magnetic resonance (NMR) spectroscopy. In addition to linear spin chains with only nearest neighbor couplings, in realistic settings also long-range couplings between non-adjacent spins must be considered. For example in ^{13}C and ^{15}N labeled proteins, the nuclei in the protein backbone form a chain of coupled spins-1/2 with dominant next neighbor 1J (single bond) couplings and smaller 2J and 3J couplings (via two or three chemical bonds) between non-adjacent spins in the chain [157].

Here we focus on the efficient creation of multi-spin operators from a single-spin operator in a spin chain, such as the creation of multiple-spin order from polarization of the first spin

$$I_{1z} \rightarrow 2^{n-1} I_{1z} I_{2z} \cdots I_{(n-1)z} I_{nz}. \quad (6.1)$$

The transfer shown in Eq. (6.1) is just a prototype example of a general transfer of the form

$$I_{1\delta} \rightarrow 2^{n-1} I_{1\epsilon_1} \cdots I_{n\epsilon_n}, \quad (6.2)$$

where $\delta, \epsilon_k \in \{x, y, z\}$ for $k = 1, \dots, n$. Note that the transformations in Eqs. (6.1) and (6.2) are identical up to local spin rotations. Hence, in the limit where the time for selective rotations of individual spins is negligible (compared to $1/(2J_{max})$, where J_{max} is the largest spin-spin coupling constant in the chain), the transformations in Eqs. (6.1) and (6.2) can be achieved in the same amount of time. (This situation is typical for heteronuclear NMR experiments in liquid state, where the control amplitudes for single spin operators are orders of magnitude larger than the largest coupling constants.) In Eq. (6.2), the initial single-spin state is not limited to longitudinal magnetization (polarization I_{1z}) but may also be transverse magnetization (in-phase coherence I_{1x} or

I_{1y}) [157, 158]. Examples of multi-spin target operators in Eq. (6.2) containing one or several transverse operators include states of the form $2^{n-1}I_{1z}I_{2z}\cdots I_{(n-1)z}I_{nx}$ (corresponding to anti-phase coherence of spin n with respect to spins 1 to $n-1$), and $2^{n-1}I_{1x}I_{2x}\cdots I_{(n-1)x}I_{nx}$ (corresponding to multi-quantum coherence), which are relevant in so-called “out and back” transfer schemes [157, 159, 160] and in the creation of multiple-quantum coherence [158, 161], respectively.

We consider the case of Ising-type spin chains [162, 163], corresponding to the weak coupling limit [158]. In this limit, which is an excellent approximation for hetero-nuclear NMR experiments, the coupling Hamiltonian for a pair of spins k and l has the form

$$H_{kl}^{\text{weak}} = 2\pi J_{kl}I_{kz}I_{lz},$$

where J_{kl} is the coupling constant in units of Hertz (Hz). In conventional experiments, the standard methods to achieve transfer in Eq. (6.2) are based on COSY- or RELAY-type transfer steps [157, 158], which are realized in hetero-nuclear experiments by a series of INEPT building blocks [164] (see Sec. 6.2). The transfer time is determined by the size of the coupling constants J_{kl} in a given spin system. For example, in a linear spin chain with only next-neighbor couplings, the total duration is given by

$$T_{\text{conv}} = (J_{12}^{-1} + J_{23}^{-1} + \cdots + J_{(n-1)n}^{-1})/2.$$

We are interested in finding the shortest possible time to achieve the transfer in Eq. (6.2) or conversely, the maximum transfer amplitude for any given time, which remains an open question up to now.

For relatively simple spin systems, consisting of up to three spins, time-optimal [165–171] and relaxation-optimized [172–177] pulse sequences have been recently found analytically based on methods of optimal control theory [178–182], establishing rigorous physical limits of minimal transfer times or minimal relaxation losses, respectively. In addition to powerful analytical tools, optimal control theory also provides efficient numerical algorithms for the optimization of pulse sequences, such as the gradient ascent pulse engineering (GRAPE) algorithm, exploiting the known equation of motion for the spin system [183–186]. With this algorithm it is possible to optimize tens of thousands of pulse sequence parameters and the resulting pulse sequences are not limited to previously known transfer schemes. However, in contrast to analytical methods proving global optimality of a given pulse sequence, there is no guarantee that numerical optimal control algorithms like GRAPE will converge to the global optimum [187]. Never-the-less, in cases where the theoretical limits are known, the GRAPE algorithm closely approached these limits [183, 188]. This motivated its use also in cases for which analytical results on the global optimum are presently unknown in order to explore the physical limits of the maximum possible transfer efficiency as a function of transfer time, resulting in so-called TOP (time-optimal pulse) curves [127, 181, 189–192]. Furthermore, additional effects such as relaxation [193, 194], radiation damping [195], and experimental constraints and imperfections—such as limited control amplitudes and control field inhomogeneities [196–198]—can be taken into account to find highly robust pulses suitable for practical applications under realistic conditions.

Assuming a restricted pulse structure (see Secs. 6.3.1 and 6.4.1) analytic pulses were derived in Refs. [151] and [152], respectively, for the case of equal and unequal couplings. This results in significantly shorter transfer times compared to conventional approaches, however it was not clear how closely the performance of the derived pulse sequences converges to the time-optimal performance.

In this chapter, we summarize the analytic approach of Refs. [151, 152] (see Sections 6.3.1 and 6.4.1) and explore its time-optimality by conducting a systematic nu-

numerical study of the considered coherence transfer (see Sections 6.3.2 and 6.4.2). Focusing on the case of linear Ising spin chains with three and four qubits we compare the duration of pulse sequences for arbitrary pulse structures with the restricted pulse structure motivated by the analytic pulses. We also numerically analyze linear Ising spin chains for up to six spins (see Section 6.7). In addition, our numerical approach makes it also possible to investigate more realistic spins systems with more general coupling topologies (see Section 6.5).

In Sec. 6.6, we show how to make the pulse sequences robust with respect to off-resonance effects using the DANTE (Delays Alternating with Nutations for Tailored Excitation) approach [169, 199, 200]. Finally, we present experimental results for model spin chains consisting of three and four hetero-nuclear spins-1/2, demonstrating good performance of the new sequences under experimental conditions and comparing the results to conventional pulse sequences.

6.2 Coherence transfer in linear Ising spin chains

Throughout this chapter we mostly consider linear Ising spin chains which have only direct couplings between neighboring spins [162, 163]. (Later we will also allow additional couplings between non-neighboring spins.) Assume that a chain of n spins is placed in a static external magnetic field along the z -direction and that neighboring spins are coupled by an Ising interaction where the coupling strengths $J_{\ell, \ell+1}$ are fixed but may depend on the position $1 \leq \ell \leq n-1$ in the chain. Without any control, the system evolves freely under its drift Hamiltonian

$$H_d = 2\pi \sum_{\ell=1}^{n-1} J_{\ell, \ell+1} I_{\ell z} I_{(\ell+1)z}.$$

The drift Hamiltonian is given in a suitably chosen multiple rotating frame, which rotates simultaneously at the resonance frequency of each spin. We use the product-operator basis $I_{\ell\nu} = \bigotimes_j I_{a_j}$ where $a_j = \nu$ for $j = \ell$ and $a_j = 0$ otherwise (see Ref. [158]). The matrices $I_x := (\begin{smallmatrix} 0 & 1 \\ 1 & 0 \end{smallmatrix})/2$, $I_y := (\begin{smallmatrix} 0 & -i \\ i & 0 \end{smallmatrix})/2$, and $I_z := (\begin{smallmatrix} 1 & 0 \\ 0 & -1 \end{smallmatrix})/2$ are the Pauli spin matrices and $I_0 := (\begin{smallmatrix} 1 & 0 \\ 0 & 1 \end{smallmatrix})$ is the (2×2) -dimensional identity matrix. In addition to the free evolution, we assume that individual spins can be selectively excited using radio-frequency (RF) pulses, which is the case if the Larmor frequencies of the spins are well separated as compared to the coupling strengths $J_{\ell, \ell+1}$. Thus controls on individual spins can be applied on a much faster time scale as compared to the free evolution w.r.t. the drift Hamiltonian.

We derive explicit controls for the amplitude and phase of the external RF fields implementing a unitary evolution which transforms an initial polarization I_{1x} on the first spin to a multiple-spin state $2^{n-1} (\prod_{\ell=1}^{n-1} I_{\ell y}) I_{nz}$ while minimizing the pulse duration t_p . In the following, we often compare control pulses with the *conventional strategy*, which consists of $n-1$ steps of free evolution ($1 \leq m \leq n-1$)

$$2^{m-1} I_{1y} \cdots I_{m-1, y} I_{mx} \xrightarrow{H_d} 2^m I_{1y} \cdots I_{my} I_{m+1, z}$$

where each individual step—besides the final one—is followed by one hard $\frac{\pi}{2}$ -pulse on the $(m+1)$ th spin along the y -direction. As each period of free evolution is of length $1/(2J_{\ell, \ell+1})$ where $J_{\ell, \ell+1}$ is given in Hz, the total evolution time is given by $t_p = \sum_{\ell=1}^{n-1} 1/(2J_{\ell, \ell+1})$.

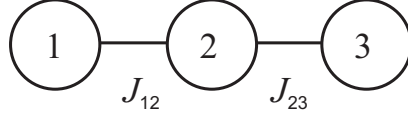


Figure 6.1: A linear three-spin chain has only direct couplings J_{12} and J_{23} between neighboring spins.

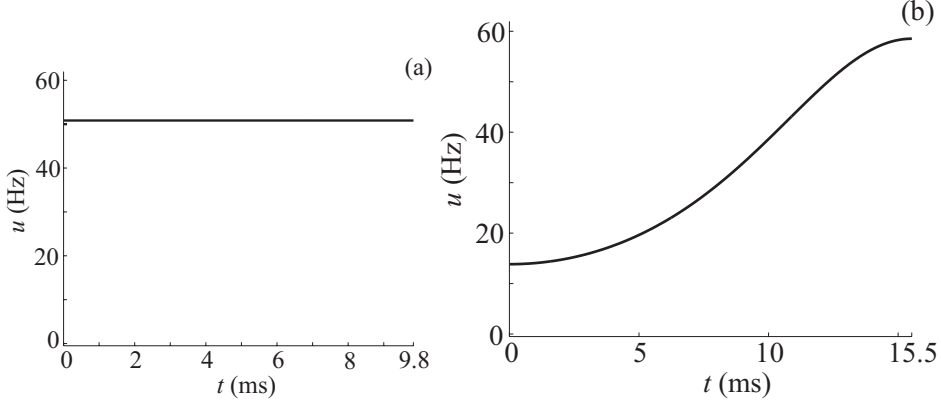


Figure 6.2: Analytic pulses for linear three-spin chains are given in the cases of (a) $k = J_{23}/J_{12} = 88.05/88.05 = 1$ and (b) $k = 1.59 \approx J_{23}/J_{12} = 73.1/46$.

6.3 Linear three-spin chains: analytic and numerical approaches

6.3.1 Analytic approach

In this section, we consider the model of Sect. 6.2 in the case of linear three-spin chains (see Fig. 6.1). In the most general case, one could allow independent controls on each of the three spins along both the x - and y -direction. But in order to simplify the control problem we allow only one control on the second spin along the y -direction. This might not lead to time-optimal controls. But even using this restricted model, controls which are shorter as compared to the conventional strategy were obtained in Ref. [152] (see also [151]). In the following, we summarize the analytical approach of Ref. [152].

Starting from an initial state I_{1x} and using only one control on the second spin along the y -direction, we can analyze the control problem on the subspace spanned by the operators I_{1x} , $2I_{1y}I_{2z}$, $2I_{1y}I_{2x}$, and $4I_{1y}I_{2y}I_{3z}$ as compared to the full 63-dimensional space of operators. Using the notation $\langle O \rangle := \text{Tr}(O\rho)$ for the expectation value and Tr for the trace, we denote the corresponding expectation values by $x_1 = x_1(t) = \langle I_{1x} \rangle$, $x_2 = x_2(t) = \langle 2I_{1y}I_{2z} \rangle$, $x_3 = x_3(t) = \langle 2I_{1y}I_{2x} \rangle$, and $x_4 = x_4(t) = \langle 4I_{1y}I_{2y}I_{3z} \rangle$. We obtain the differential equation

$$\begin{pmatrix} \dot{x}_1 \\ \dot{x}_2 \\ \dot{x}_3 \\ \dot{x}_4 \end{pmatrix} = \pi \begin{pmatrix} 0 & -1 & 0 & 0 \\ 1 & 0 & -u & 0 \\ 0 & u & 0 & -k \\ 0 & 0 & k & 0 \end{pmatrix} \begin{pmatrix} x_1 \\ x_2 \\ x_3 \\ x_4 \end{pmatrix}, \quad (6.3)$$

where $u = u(t)$ denotes the amplitude of the control on the second spin along the y -direction and $k = J_{23}/J_{12}$. Using the coordinates $(x_1, x_2, x_3, x_4)^T$ we aim to time-efficiently transfer $(1, 0, 0, 0)^T$ to $(0, 0, 0, 1)^T$.

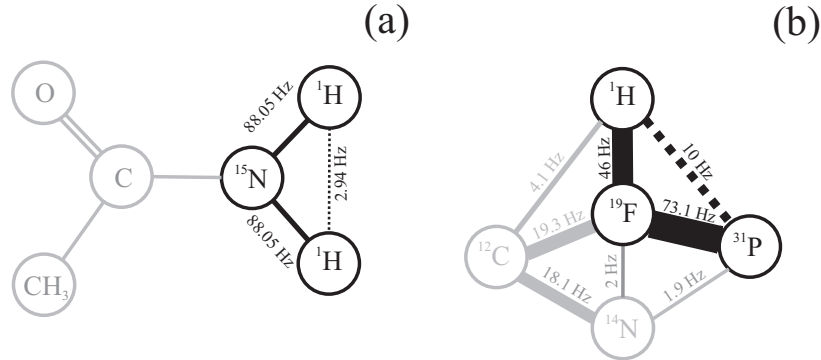


Figure 6.3: The schematic coupling topologies of (a) ethanamide and (b) diethyl-(dimethylcarbonyl)fluoromethylphosphonate (see [201, 202]) result in experimental three-spin systems with coupling ratios (a) $k = 1 = 88.05/88.05$ and (b) $k = 1.59 \approx 73.1/46$. Larger couplings are shown as solid-black lines, and smaller couplings are shown as dashed-black lines. Decoupled spins are given in gray color.

Now, we change from the coordinates $(x_1, x_2, x_3, x_4)^T$ to the coordinates

$$(r_1, r_2, r_3)^T = (x_1, \sqrt{x_2^2 + x_3^2}, x_4)^T$$

on the sphere where $\theta = \theta(t)$ is given by $\tan \theta = x_3/x_2$. This transforms Eq. (6.3) to

$$\begin{pmatrix} \dot{r}_1 \\ \dot{r}_2 \\ \dot{r}_3 \end{pmatrix} = \pi \begin{pmatrix} 0 & -\cos \theta & 0 \\ \cos \theta & 0 & -k \sin \theta \\ 0 & k \sin \theta & 0 \end{pmatrix} \begin{pmatrix} r_1 \\ r_2 \\ r_3 \end{pmatrix}.$$

In the new coordinates, we want to time-efficiently transfer $(1, 0, 0)^T$ to $(0, 0, 1)^T$.

In order to find the time-optimal controls, Euler-Lagrange equations were set up and solved in Ref. [152] leading to the differential equation

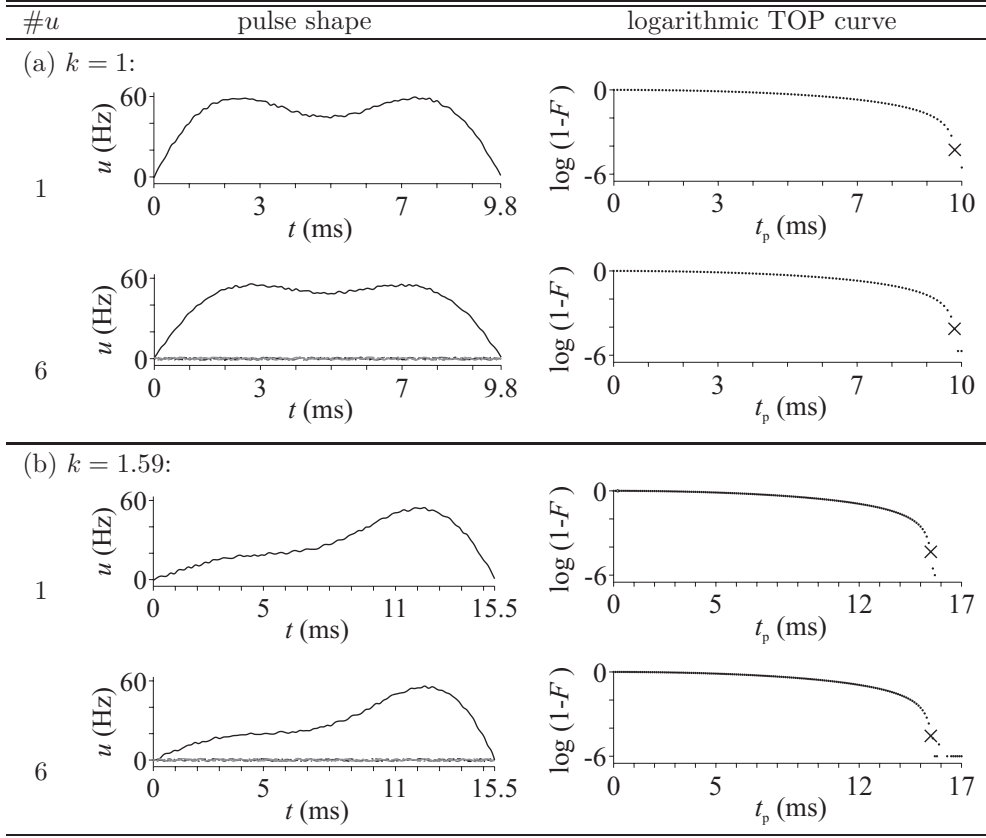
$$\ddot{\theta} = \frac{k^2 - 1}{2} \sin 2\theta \quad (6.4)$$

for the variable θ . The differential Eq. (6.4) can be numerically integrated if the initial values $\theta(0)$ and $\dot{\theta}(0)$ are known. Using the results of Ref [152] one can determine conditions on the initial values: In the case of $(r_1(0), r_2(0), r_3(0))^T = (1, 0, 0)^T$ one can deduce that $\theta(0) = 0$, but $\dot{\theta}(0)$ is undetermined. In Ref. [152] combinations of one-dimensional searches were used to determine the optimal $\theta_{\text{opt}}(t)$ and the time-optimized control as $u_{\text{opt}}(t) = J_{12}\dot{\theta}_{\text{opt}}(t)$. Examples for the corresponding (semi-)analytic pulses are shown in Fig. 6.2. The values are motivated by the experimental systems given in Fig. 6.3.

6.3.2 Numerical approach

We numerically optimize pulse shapes by employing the GRAPE algorithm [183] which was developed by employing principles of optimal control theory. Using a gradient-based optimization we obtain RF controls which steer an initial state (or unitary transformation) to a final state (or unitary transformation) while minimizing (e.g.) the duration of the pulse. Both the amplitude and the phase of the resulting pulse can be smoothly- or noisy-shaped depending on e.g. the initial pulse or bounds on the control strength (see, e.g. [197]).

Table 6.1: We compare the duration t_p , the logarithmic fidelity F , and the shape of numerically-optimized pulses for a linear three-spin chain with coupling ratios (a) $k = 1$ and (b) $k = 1.59$. The number of controls $\#u$ is given in the first column. In the third column we present the corresponding logarithmic TOP curves. The second column shows an example of a shaped pulse, whose position is denoted with an x in the logarithmic TOP curve. The RF control on the middle spin along the y -axis is plotted using a solid-black line. Other RF controls are plotted using dashed or solid-gray lines.



We treat three different levels of RF controls: First, we use only one RF control operating on the second spin along the y -direction. Second, we use two different RF controls operating on the second spin along both the x - and y -direction. Third, we use a total of six RF controls operating on each of the three spins along both the x - and y -direction. We remark that employing RF controls on one spin along both the x - and y -direction gives complete (local) control on that spin. Let k denote the ratio between the couplings J_{23} and J_{12} . We determine the numerically-optimized pulses and plot the logarithmic fidelity F vs. the duration t_p of different shaped pulses for the coupling ratios $k = 1$ and $k = 1.59$ which are motivated by the experimental scenarios of Fig. 6.3. The numerical results are given in Table 6.1: We show examples of shaped pulses with short duration t_p and high fidelity $F \geq 0.9999$. In addition, we present logarithmic time-optimal (TOP) curves where we plot the logarithmic transfer efficiency (i.e. $\log(1-F)$ where F is the fidelity) versus the optimal transfer time. Comparing the different cases suggests that only one RF control on the second spin is sufficient for a time-optimal pulse. For high fidelities ($F \geq 0.9999$), the durations of the analytic and numerically-optimized pulses are identical (in the given accuracy) while the pulse forms differ. In Table 6.2, we compare the duration of pulses on linear three-spin systems for

Table 6.2: For coherence transfers in linear three-spin chains ($k = 1$ and $k = 1.59$), we give the numerically-optimized times t_p and the fidelities F in the case of one, two, and six RF controls (see text). The duration t_p is independent of the number of controls which suggests that only one RF-control on the middle spin is sufficient for the time-optimal coherence transfer.

k	$\#u$	t_p (s)	F
1	1	0.0098	0.9999
1	2	0.0098	0.9999
1	6	0.0098	0.9999

k	$\#u$	t_p (s)	F
1.59	1	0.0155	0.9999
1.59	2	0.0155	0.9999
1.59	6	0.0155	0.9999

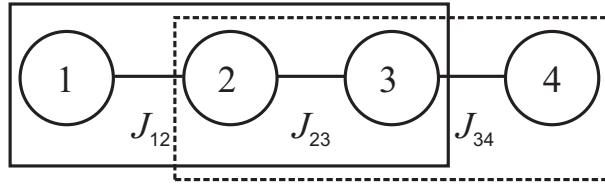


Figure 6.4: A linear four-spin chain has only direct couplings J_{12} , J_{23} , and J_{34} between neighboring spins. We split the corresponding four-spin chain control problem into two subproblems for three-spin chains.

different values of k .

Conjecture 1 Consider a linear three-spin chain with local controls on each spin. One can time-optimally transfer coherence from I_{1x} to $4I_{1y}I_{2y}I_{3z}$ using only one control on the second spin along the y -direction. In addition, the analytical pulses of Refs. [151, 152] are time-optimal in the case of linear three-spin chains even if one allows arbitrary local controls.

6.4 Linear four-spin chains: analytic and numerical approaches

6.4.1 Analytic approach

In this section, we consider linear spin chains with four spins. We follow Sect. IV of Ref. [152] (see also [151]) and split the control problem for four spins into two subproblems for three spins (see Fig. 6.4): The first subproblem is given on the first three spins by the time-optimal transfer from $(1, 0, 0)^T$ to $(0, \cos \gamma, \sin \gamma)^T$, where we are again using the coordinates $(r_1, r_2, r_3)^T$ of Sect. 6.3.1. Then, we apply certain (arbitrarily fast) hard pulses which can be easily determined by numerical methods. The second subproblem is given on the last three spins by the time-optimal transfer from $(\cos \gamma, \sin \gamma, 0)^T$ to $(0, 0, 1)^T$. In addition, we have to simultaneously search for the value of γ which minimizes the pulse duration. This approach might not lead to time-optimal controls but simplifies the control problem significantly.

The optimization of the considered subproblems can be reduced to time-optimal transfers from $(\cos \alpha, \sin \alpha, 0)^T$ to $(0, \cos \beta, \sin \beta)^T$ for $\alpha, \beta \in [0, \pi/2]$ generalizing the transfer of Sect. 6.3.1 from $(1, 0, 0)^T$ to $(0, 0, 1)^T$. Using methods of Ref. [152] we can find the optimal controls for the transfers using combined one-dimensional searches for the optimal initial values $\theta(0)$ and $\dot{\theta}(0)$ of Eq. (6.4). Both $\theta(0)$ and $\dot{\theta}(0)$ are undetermined but related by $\dot{\theta}(0) = \sin[\theta(0)] \cot \alpha$ for the case of $(r_1(0), r_2(0), r_3(0))^T = (\cos \alpha, \sin \alpha, 0)^T$.

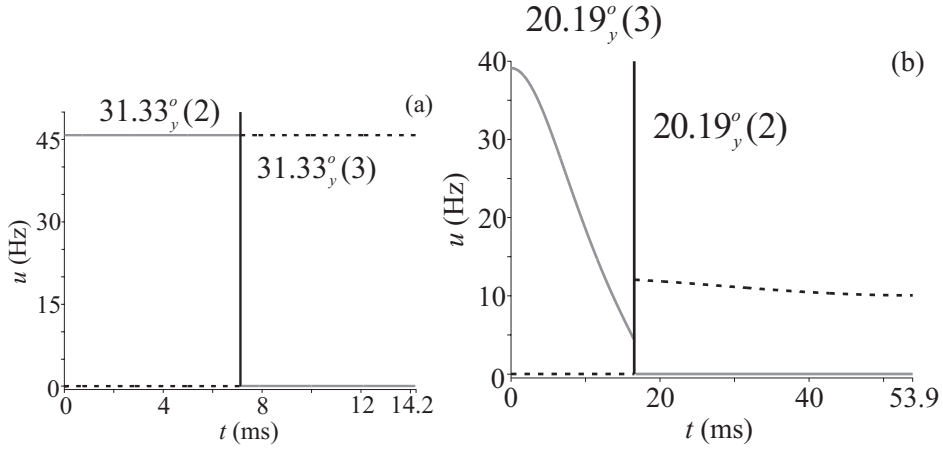


Figure 6.5: Analytic pulses for linear four-spin chains are given in the cases of (a) $k_1 = k_2 = 1$ as well as (b) $k_1 = 2.38$ and $k_2 = 0.94$. The pulses on the second and third spin along the y -direction are given, respectively, as solid and dashed line. The corresponding two hard pulses on the second and third spin are depicted by a vertical line where the flip angles are given above. The hard pulses in the left figure can be implemented by applying a pulse of 5000 Hz for 17.40 microseconds. The hard pulses in the right figure can be implemented by applying a pulse of 5000 Hz for 11.21 microseconds.

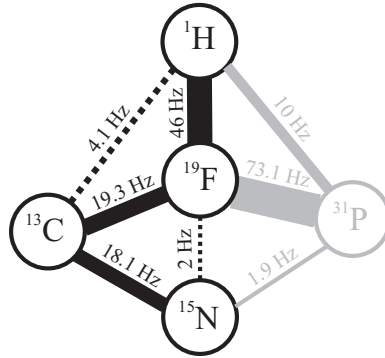


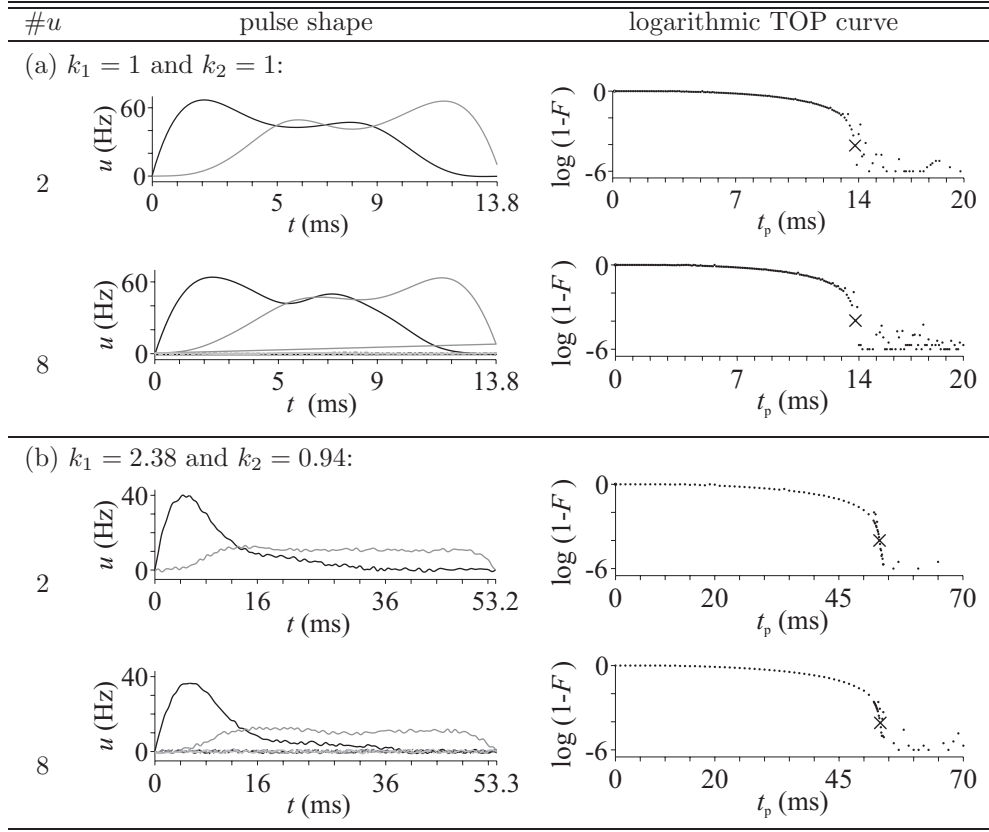
Figure 6.6: The topology of the ^{13}C - ^{15}N -diethyl(dimethylcarbonyl)fluoromethylphosphonate (see [201, 202]) results in coupling ratios $k_1 = 2.38$ and $k_2 = 0.94$. Compare to Fig. 6.3.

The corresponding (semi-)analytic pulses are shown in Fig. 6.5. The values are motivated by the experimental system given in Fig. 6.6.

6.4.2 Numerical approach

Motivated by the analytical approach, we numerically treat the control problem on four spins with two cases of coupling ratios (a) $k_1 = 1$ and $k_2 = 1$ ($J_{12} = J_{23} = J_{34} = 88.05$ Hz), and (b) $k_1 = 2.38 \approx J_{12}/J_{23}$ and $k_2 = 0.94 \approx J_{34}/J_{23}$ (refer to Fig. 6.6 for the coupling values). The coherence transfer is numerically optimized considering the following three levels of RF controls: First, we use only two different RF controls (one on each spin) operating on the second and third spin along the y -direction. Second, we use a total of four different RF controls (two on each spin) operating on the second and third spin along both the x - and y -direction. Third, we use a total of eight different RF controls (two on each spin) operating on each of the four spins along both the x - and y -direction. The pulse shapes and the logarithmic TOP curves corresponding to two

Table 6.3: For linear four-spin chains with coupling ratios (a) $k_1 = 1$ and $k_2 = 1$ as well as (b) $k_1 = 2.38$ and $k_2 = 0.94$, the RF controls on the second and third spin along the y -axis are plotted using solid-black and solid-gray lines, respectively. Other RF controls are plotted using a dashed-black line or in shades of gray. Compare to Table 6.1.



and eight RF controls (see Table 6.3) indicate that we do not gain a higher fidelity or a shorter duration from using more than the two controls (Table 6.4). This is consistent with the analytic results, but the numerically-optimized pulses appear to be a little shorter than the analytical ones (cp. Fig. 6.5).

Conjecture 2 Consider a linear four-spin chain with local controls on each spin. One can time-optimally transfer coherence from I_{1x} to $8I_{1y}I_{2y}I_{3y}I_{4z}$ using only two controls along the y -direction which operate on the second and third spin, respectively.

6.5 More generally-coupled spin systems of three and four spins

In more generally-coupled spin systems, indirect couplings can strongly impede or enhance the coherence transfer. In this section we present detailed numerical optimizations and compare them to the case of linear spin chains.

Table 6.4: For coherence transfers in linear four-spin chains ($k_1 = k_2 = 1$ as well as $k_1 = 2.38$ and $k_2 = 0.94$), we give the numerically-optimized times t_p and the fidelities F in the case of two, four, and eight RF-controls. The duration t_p is independent of the number of controls which suggests that only two RF-control on the second and third spin along the y -axis is sufficient for the time-optimal coherence transfer.

k_1	k_2	$\#u$	t_p (s)	F
1	1	2	0.138	0.9999
1	1	4	0.138	0.9999
1	1	8	0.138	0.9999

k_1	k_2	$\#u$	t_p (s)	F
2.38	0.94	2	0.532	0.9999
2.38	0.94	4	0.532	0.9999
2.38	0.94	8	0.533	0.9999

6.5.1 Three-spin system

Along the lines of Section 6.3.2, we numerically optimize pulses for more generally-coupled three-spin systems keeping $J_{12} = J_{23} = 88.05$ Hz constant while varying the additional coupling strength J_{13} . By comparing the TOP curves for different values of J_{13} , we conclude that for a larger coupling strength J_{13} the fidelity of the coherence transfer is smaller in the cases of one [Fig. 6.7(a)] and two (results are not shown) RF controls on the second spin. (As in Section 6.3.2, we obtain shorter pulse sequences as compared to the conventional pulse sequence for $J_{13} = 0$.) However, using the RF controls on each of the three spins allows for a coherence transfer with higher fidelity while keeping the pulses short [Fig. 6.7(b)]. Table 6.5 shows examples of shaped pulses and the corresponding logarithmic TOP curves for the coupling ratios $k = 1$ and $k = 1.59$. The coupling strengths are taken from the spin systems shown in Fig. 6.3. Detailed values are given in Table 6.7.

6.5.2 Four-spin system

Following Section 6.4.2, we numerically optimize the shaped pulses for a more generally-coupled four-spin systems. Analyzing the numerical results (see Table 6.6), we can say that this system needs all eight RF controls on each spin along both the x - and y -direction in order to achieve the coherence transfer with minimum duration and maximal fidelity. Table 6.7 summarizes and compares the duration t_p and fidelity F of shaped pulses for more generally-coupled spin systems.

6.6 Experimental results

Analytic and numerically-optimized pulses are usually optimized for on-resonance cases. We follow the DANTE approach [199, 200, 203] in order to obtain pulses which are broadband, i.e. invariant with respect to the change of the chemical shift in a given offset range (Fig. 6.8). First, a shaped pulse is converted into a sequence of short hard pulses and delays. We used hard pulses with constant flip angles (see below), and the delays between the hard pulses correspond to the time required by the shaped pulse to accumulate this flip angle [199, 200, 203]. Then, a refocusing element (i.e. π -pulse) [169, 200] is inserted between two hard pulses. The offset bandwidth covered by a refocused DANTE sequence is directly proportional to the RF amplitude of the hard pulses and the π -pulses used in the sequence.

All the experiments are implemented on a Bruker AVANCE III 600 MHz spectrometer at 298 Kelvin: We use a triple resonance TXI probe head with Z-gradient in the case of the three-spin system with $k = 1$. For the three spin system with $k = 1.59$ and

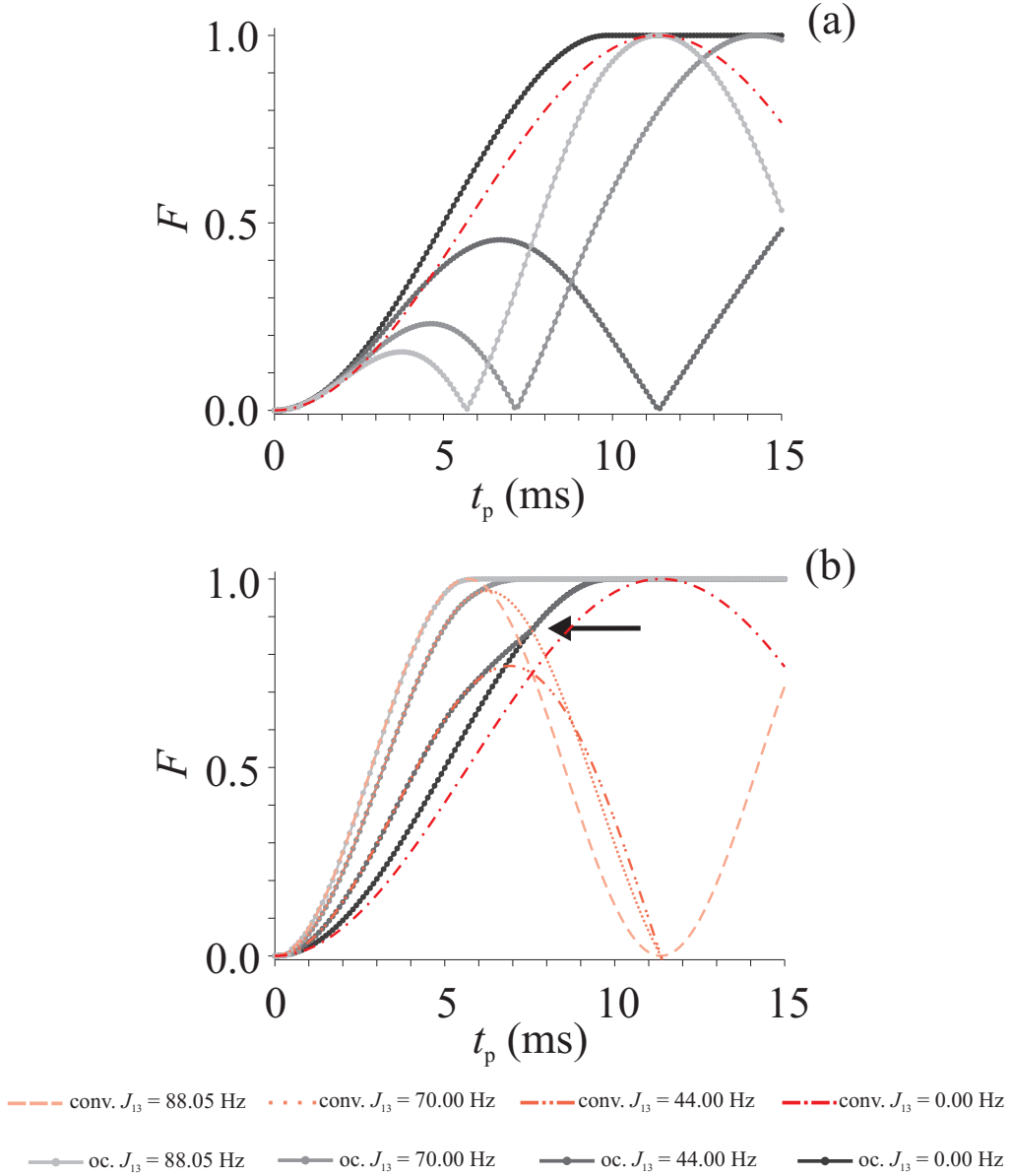


Figure 6.7: (Color online) We compare numerically-optimized TOP curves (in shades of gray) for three-spin systems with one [Subfigure (a)] and six [Subfigure (b)] RF controls keeping $J_{12} = J_{23} = 88.05$ Hz constant while varying J_{13} . At the same time we compare their performance with conventional pulse sequences (in shades of red) where both of the couplings J_{12} and J_{13} evolve simultaneously. The limiting case of $J_{13} = 0$ corresponds to the conventional pulse sequence of Sec. 6.2. Using all six RF controls [Subfigure (b)] we can see higher fidelities F for smaller times and larger J_{13} compared to the case of only one RF control [Subfigure (a)]. A black arrow denotes where the numerically-optimized TOP curves for $J_{13} = 44$ Hz and $J_{13} = 0$ Hz merge.

the four spin system with $k_1 = 2.38$ and $k_2 = 0.94$ we use a custom-made 6-channel probe head with Z-gradient addressing all nuclei ^{19}F , ^1H , ^{31}P , ^{12}C (or ^{13}C), and ^{14}N (or ^{15}N) (see [201,202]). In the experiments for three spins we use the molecules shown in Fig. 6.3. The experiment for the coupling ratio $k = 1$ uses the first molecule (see

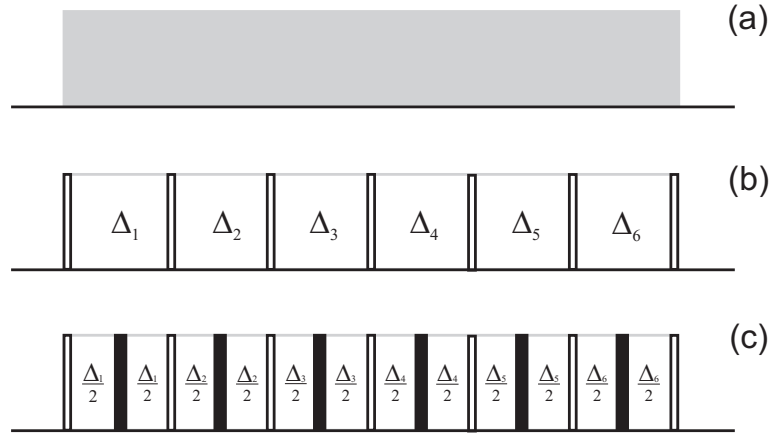


Figure 6.8: In the DANTE approach an on-resonance shaped pulse (see (a)) is converted to a series of short hard pulses and delays Δ_i (see (b)). Then, the pulse can be converted to a broadband pulse by inserting a refocusing element (i.e. π -pulse) represented by solid bars between two hard pulses (see (c)).

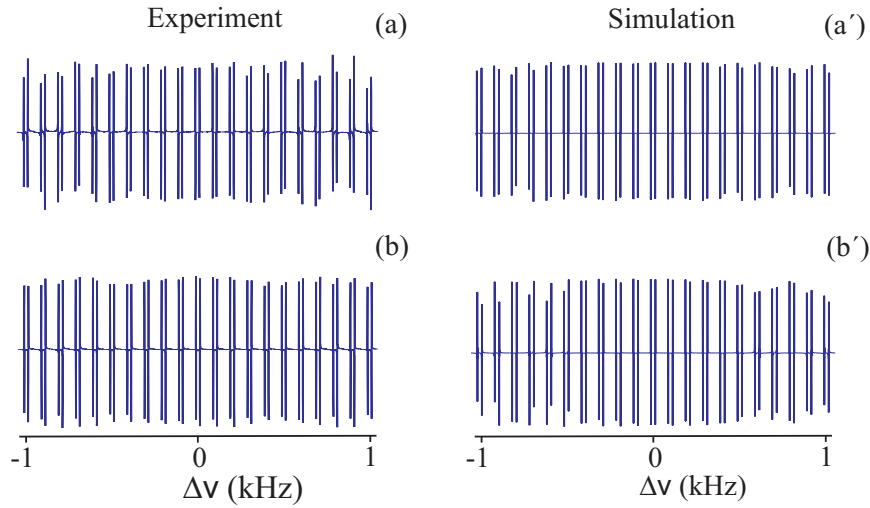


Figure 6.9: (Color online) We compare for a three-spin system the offset ($\Delta\nu$) profile for ± 1 kHz of the anti-phase signal (see text) resulting from a conventional pulse sequence ($t_p = 11.4$ ms) in the case of experiment (see (a)) and simulation (see (a')) with broadband versions of the analytic pulses ($t_p = 9.8$ ms, see (b) and (b')) for the case of coupling ratio $k = 1$ of three spins.

Table 6.5: Numerical results for more generally-coupled three-spin systems with (a) coupling ratio $k = 1$ (i.e. $J_{12} = J_{23} = 88.05$ Hz) and additional coupling $J_{13} = 2.935$ Hz as well as (b) coupling ratio $k = 1.59$ (i.e. $J_{12} = 73.1$ Hz and $J_{23} = 46$ Hz) and additional coupling $J_{13} = 10.0$ Hz. Compare to Table 6.1.

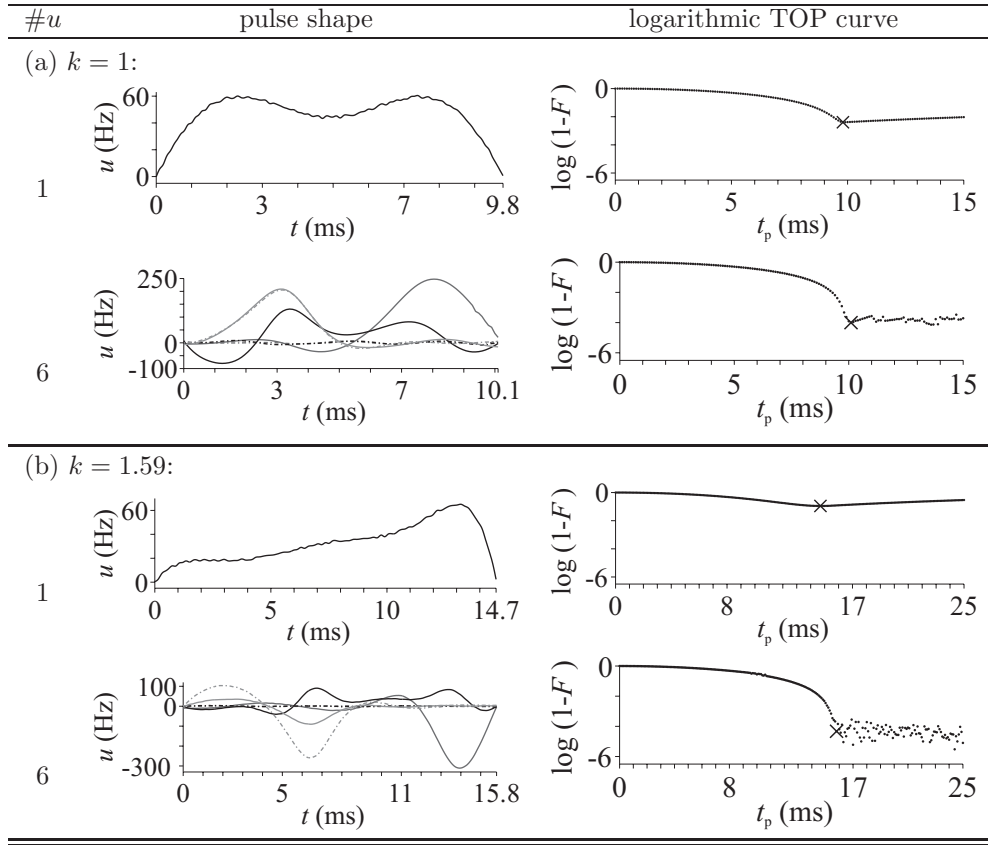


Fig. 6.3(a)) which is dissolved in deuterated water D_2O . For $k = 1.59$ we use the second molecule (see Fig. 6.3(b)) dissolved in deuterated methanol CD_3OD . The simulated and experimental offset profiles are shown in Figs. 6.9 and 6.10. We emphasize that the duration of the broadband versions of the analytic or the numerically-optimized pulses is shorter than for the conventional pulse sequence while keeping its robustness.

We first discuss two three-spin systems: In the case of $k = 1$, we start from the initial polarization I_{1z} of 1H (which models the first spin) and apply a $\frac{\pi}{2}$ -pulse along $+y$ -direction in order to obtain the coherence I_{1x} . By applying a broadband version of our shaped pulse of ^{15}N (which models the second spin) we get the three-spin coherence $4I_{1y}I_{2y}I_{3z}$. The broadband version of this shaped pulse is divided into four hard pulses with an amplitude of 4145.936 Hz, a flip angle of 45.00 degrees, and zero phase; it also contains refocusing π -pulses where the phases are chosen according the MLEV-4 cycle [204]. Next, we apply $\frac{\pi}{2}$ -pulse on ^{15}N along the x -direction and we obtain the coherence $4I_{1y}I_{2z}I_{3z}$. In the end, we can detect an anti-phase signal of 1H (first spin) with respect to the spins of ^{15}N and 1H (which models the third spin). Similarly, in the case of $k = 1.59$, we start from the initial coherence I_{1z} on the spin of 1H (which models the first spin) and apply a $\frac{\pi}{2}$ -pulse along $+y$ -direction in order to obtain the coherence I_{1x} . Then, we apply the broadband version of our shaped pulse on the spin

Table 6.6: Numerical results for a more generally-coupled four-spin systems with coupling ratios $k_1 = 2.38 \approx J_{12}/J_{23}$ and $k_2 = 0.94 \approx J_{34}/J_{23}$ (i.e. $J_{12} = 46$ Hz, $J_{23} = 19.3$ Hz, and $J_{34} = 18.1$ Hz) as well as additional couplings $J_{13} = 4.1$ Hz and $J_{24} = 2$ Hz. Compare to Table 6.3.

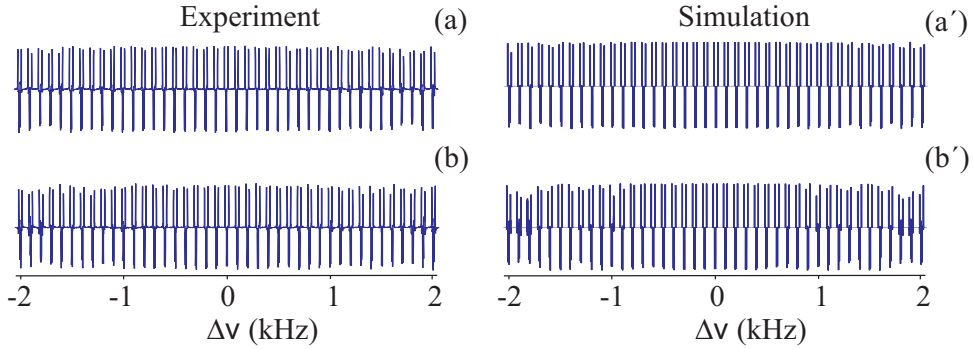
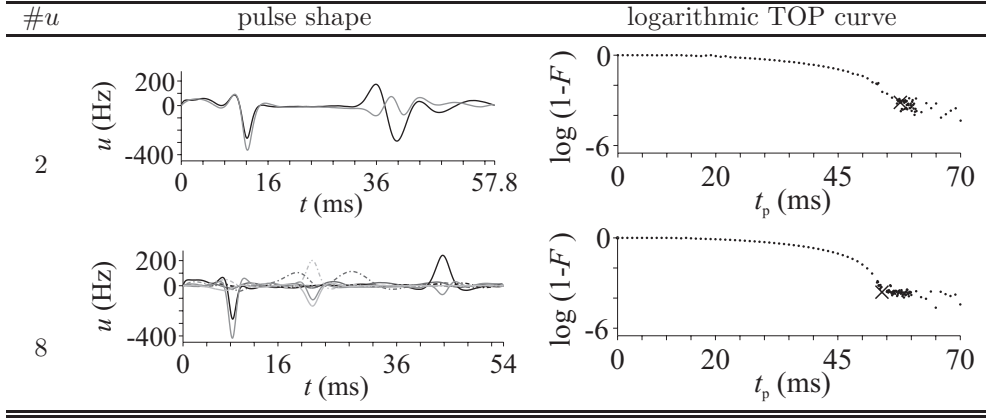
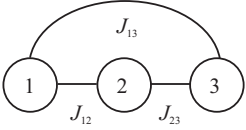
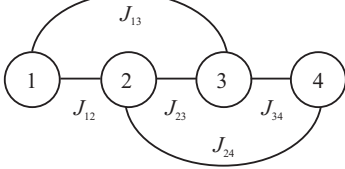


Figure 6.10: (Color online) We compare for a three-spin system the offset (Δv) profile for ± 2 kHz of the anti-phase signal (see text) resulting from a conventional pulse sequence ($t_p = 17.7$ ms) in the case of experiment (see (a)) and simulation (see (a')) with broadband versions of the analytic pulses ($t_p = 15.5$ ms, see (b) and (b')) for the case of coupling ratio $k = 1.59$.

of ^{19}F in order to produce the three-spin coherence $4I_{1y}I_{2y}I_{3z}$. The broadband version of this shaped pulse is divided into four hard pulses with an amplitude of 10000 Hz, a flip angle of 45.03 degrees, and zero phase; it also contains refocusing π -pulses where the phases are chosen according the MLEV-4 cycle [204]. In the next step, we apply a $\frac{\pi}{2}$ -pulse on the spin of ^1H and we end up with the coherence $4I_{1z}I_{2y}I_{3z}$. Finally, we detect an anti-phase signal on the spin of ^{19}F with respect to the spins of ^1H and ^{31}P .

In the four-spin system, we show on-resonance simulations and experiments for numerically-optimized shaped pulses comparing the conventional approach with analytical and numerically-optimized pulses (see Fig. 6.11). The corresponding experiments are implemented on the molecule of Fig. 6.6, which is dissolved in deuterated acetonitrile. Figures 6.11(b) and (c) show a reduction in signal intensity for the simulation if we compare the effect of the pulse on the abstract linear spin chain (shown in gray) with the effect on the more realistic and more generally-coupled spin system (shown in black) as the corresponding pulses were only optimized for the abstract linear spin chain. We remark that the pulse of Fig. 6.11(d) is optimized for a more generally-coupled spin system while using RF-controls on all spins. Thus, we conclude—using also the data of

Table 6.7: We compare the duration t_p and fidelity F of numerically-optimized shaped pulses in the case of three- and four-spin systems allowing a varying number of RF controls u . Using only one RF control we show the effect of indirect couplings—which are usually present in experiments—on the fidelity of optimized pulses. Hence more RF controls are necessary for higher fidelities. The J -values are taken from the actual spin systems shown in Figs. 6.3 and 6.6.

graph	J_{13} (Hz)	J_{24} (Hz)	$\#u$	t_p (ms)	F
	$k = 1$				
	0.0	–	1	9.8	0.9999
	2.9	–	1	9.8	0.9959
	2.9	–	6	11.5	0.9999
	$k = 1.59$				
	0.0	–	1	15.5	0.9999
10.0	–	1	15.5	0.8837	
10.0	–	6	15.8	0.9999	
	$k_1 = 2.38$ and $k_2 = 0.94$				
	0.0	0.0	2	53.2	0.9999
	4.1	2.0	2	53.2	0.9859
	4.1	2.0	8	54.0	0.9999

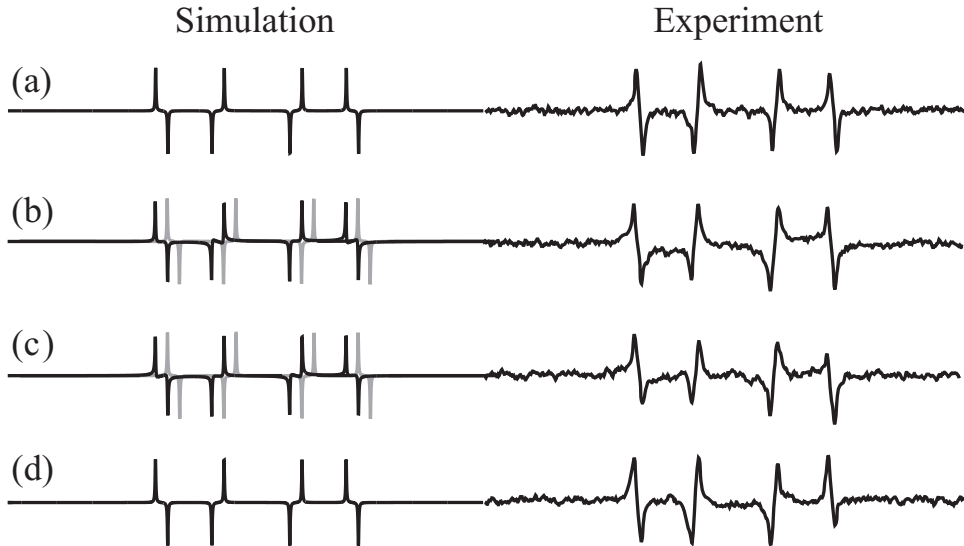


Figure 6.11: We show the anti-phase signal of the spin of ^{19}F with respect to the spins of ^1H , ^{13}C , and ^{15}N of a four-spin system corresponding to the simulation (left) and experiment (right). We use the conventional pulse sequence (a) ($t_p = 64.4$ ms), an analytical pulse sequence (b) ($t_p = 53.9$ ms), a pulse which was numerically-optimized for the abstract linear spin chain with RF controls on the second and third spin (c) ($t_p = 53.2$ ms), and a pulse which was numerically-optimized for the more generally-coupled spin system with RF controls on all spins (d) ($t_p = 54.0$ ms). The simulation for the abstract linear spin chain is given in gray color. All the other plots for the more realistic case of a more generally-coupled spin system are given in black color.

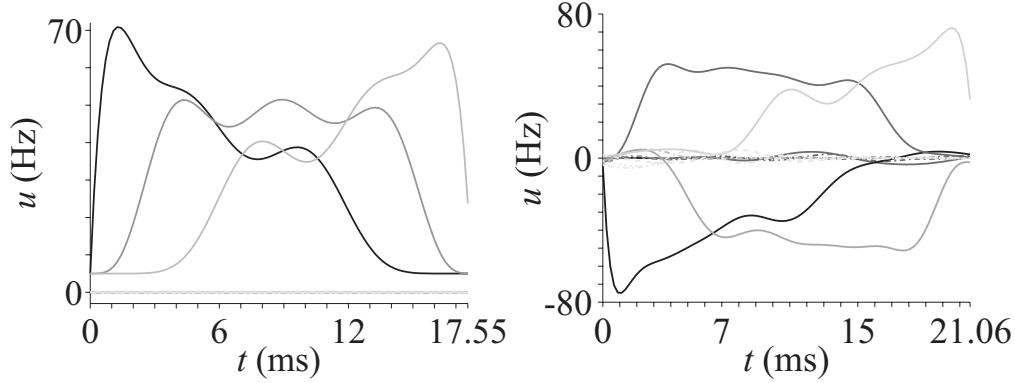


Figure 6.12: Using all ten (or twelve) RF controls we determined numerically-optimized pulse shapes for linear spin chains of length five (or six) in the case of $k = 1$. We remark that most control strengths are very small.

Table 6.7—that the pulse of Fig. 6.11(d) shows a higher fidelity when compared to the pulses of Figs. 6.11(b) and (c). Furthermore, the pulse corresponding to Fig. 6.11(d) is shorter (by 14%) than the conventional pulse sequence corresponding to Fig. 6.11(a) while maintaining its robustness to additional couplings (see also Table 6.8).

6.6.1 Conventional pulse sequences

For $k = 1$, the conventional pulse sequence implemented on the spectrometer is,

$$\text{H}_{1z} + \text{H}_{2z} \xrightarrow{H 90_y} \text{H}_{1x} + \text{H}_{2x} \xrightarrow{\Delta} \text{H}_{1x} + \text{H}_{2y} \xrightarrow{90_{-y}} \text{H}_{1z} + {}^1\text{H}_{2y} \xrightarrow{G_z} \text{H}_{1z} \quad (6.5)$$

$$\text{H}_{1z} \xrightarrow{H 90_y} \text{H}_{1x} \xrightarrow{\Delta_1} 2\text{H}_{1y}\text{N}_z \xrightarrow{N 90_y} 2\text{H}_{1y}\text{N}_x \xrightarrow{\Delta_2} 4\text{H}_{1y}\text{N}_y\text{H}_{1z} \xrightarrow{N 90_x} 4\text{H}_{1y}\text{N}_z\text{H}_{1z} \quad (6.6)$$

where, $\Delta = 1/(v_1 - v_2)$, $(v_1 - v_2)$ is the chemical shift difference between H_1 (which models the first spin) and H_2 (which models the third spin), $\Delta_1 = 1/(2J_{H_1N})$, and $\Delta_2 = 1/(2J_{H_2N})$. For $k = 1.59$, the conventional pulse sequence implemented on the spectrometer is,

$$\text{H}_z \xrightarrow{H 90_y} \text{H}_x \xrightarrow{\Delta_1} 2\text{H}_y\text{F}_z \xrightarrow{H 90_x + F 90_y} 2\text{H}_z\text{F}_x \xrightarrow{\Delta_2} 4\text{H}_z\text{F}_y\text{P}_z \quad (6.7)$$

where, $\Delta_1 = 1/(2J_{HF})$ and $\Delta_2 = 1/(2J_{FP})$.

6.7 Linear spin chains with more than four spins

In this section, we generalize the numerical optimization of shaped pulses to linear spin chains of five and more spins. Figure 6.12 shows two examples of the optimized pulse shapes with coupling ratios $k_\ell = 1$ and coupling strengths $J_{\ell, \ell+1} = 88.05$ Hz. These examples suggest that time-optimal controls can be obtained on multiple spins even while irradiating only on the spins two to $\ell - 1$ along the y -direction (cp. Sec. IV of Ref. [152]). We obtain shorter pulses for the numerically-optimized pulses compared to the conventional pulse sequences as summarized in Table 6.8.

Table 6.8: We compare the minimum time t_p required for a coherence transfer by numerically-optimized (oc) and conventional (conv) pulse sequences for different number n of spins and coupling ratios k . ^aFor $n = 3$ we have $k = 1.59$. And for $n = 4$ we have $k_1 = 2.38$ and $k_2 = 0.94$.

n	t_p (s)					
	$k = 1$			$k \neq 1^a$		
	oc	conv	oc/conv	oc	conv	oc/conv
3	0.0098	0.0114	0.8596	0.0155	0.0177	0.8757
4	0.0138	0.0170	0.8118	0.0532	0.0644	0.8261
5	0.0177	0.0227	0.7797	–	–	–
6	0.0216	0.0284	0.7605	–	–	–

6.8 Conclusion

In the case of linear three-spin chains we reproduced numerically the previous analytical results [151, 152] obtaining the same family of restricted controls by applying pulses only on the second spin along the y -axis. The same holds for linear four-spin chains where we also obtain the analytical family of restricted controls by applying pulses only on the second and third spin along the y -axis; but the numerically-optimized pulses appear to be a little shorter than the analytical ones. Both for three and four spins no gain in pulse duration is found if arbitrary pulse structures are allowed. These observations are summarized in Conjectures 1 and 2. Even for longer spin chains (consisting of up to six coupled spin-1/2) there is some numerical evidence suggesting that the same restricted controls motivated by Refs. [151, 152] lead to time-optimal pulses (in the case of unrestricted controls) for linear spin chains of arbitrary length.

Further numerical results are presented for more general and more realistic coupling topologies, for which so far no analytical results are known. Compared to linear spin chains we obtain different pulse structures depending on the number of available controls. We hope that the presented results and conjectures will motivate further analytical work in order to develop a better understanding of time-optimal control sequences for the generation of multi-spin coherence.

Note that the minimum times for the transfers $I_{1\delta} \rightarrow 2^{n-1}I_{1\epsilon_1} \dots I_{n\epsilon_n}$ and $2^{n-1}I_{1\epsilon_1} \dots I_{n\epsilon_n} \rightarrow I_{1\delta}$ are identical ($\delta, \epsilon_k \in \{x, y, z\}$ for $k = 1, \dots, n$), which is directly relevant for “out and back” experiments and the reconversion of multiple-quantum coherence to detectable single quantum operators. In the experimental part, we demonstrated that the optimized pulse sequences work in realistic settings under relaxation and experimental imperfections (e.g. inhomogeneity of the control field, miscalibrations, and phase transients). In addition, the pulses can be made broadband (i.e. robust with respect to frequency offsets) using the DANTE approach.

Here we assumed for simplicity that each spin-1/2 can be selectively addressed, which is directly relevant to heteronuclear spin systems but the optimal transfer scheme can also be adapted to homonuclear spin systems. The presented sequences can be directly applied to small molecules and peptides, which is in particular true for the broadband versions. The minimum pulse sequence durations for complete transfer are reduced by up to 24% compared to conventional approaches (see Table 6.8). Conversely, for a fixed transfer time significantly improved transfer amplitudes are possible, e.g., for a linear three-spin chain we gain approximately 23% in transfer efficiency when we allow only for half of the transfer time necessary for a complete transfer (cp. Fig. 6.7). For large proteins, further gains in efficiency are expected if relaxation-optimized pulse sequences can be developed for the specific relaxation super operator given in the system. Although

such sequences are beyond the scope of the present work, the results on time-optimal sequences presented here provide an important benchmark for relaxation-optimized sequences.

Chapter 7

The Fantastic Four: A plug ‘n’ play set of optimal control pulses

7.1 Introduction

Hard rectangular pulses are the fundamental element of all multi-dimensional NMR pulse sequences. They are simple to use and extremely versatile. The transformations required for multi-dimensional spectroscopy—excitation, flip-back, inversion, and refocusing—are all possible using this simplest of pulses. Moreover, the performance of a single hard pulse is approximately ideal over a reasonable range of resonance offsets (proportional to the RF amplitude of the pulse) and variation in RF homogeneity ($\pm 10\%$) relevant for high resolution spectroscopy [205–217].

However, there is considerable room for improving pulse sequence performance. RF amplitude is limited in practice and cannot be increased to match the increased pulse bandwidth needed at higher field strengths. The problem of large chemical shift can be solved by dividing the spectral region and performing multiple experiments. But, this is time consuming, and unstable samples can create problems. Even at lower field strengths, relatively small errors produced by a single pulse can accumulate significantly in multipulse sequences.

The use of shaped pulses that address particular limitations of hard pulses can improve performance [179], but complex multipulse sequences are masterpieces of timing and synchronized spin-state evolution. Replacing a given hard pulse in a sequence with a better performing, but longer, shaped pulse typically requires a nontrivial redesign of the pulse sequence. Additional pulses and delays are required to reestablish the timing and refocusing that achieve the goals of the original hard-pulse sequence (see Fig. 7.1).

The goal of the present work is to provide a fundamental set of better-performing pulses that can simply replace, in a one-to-one fashion, all the hard 90° and 180° pulses in any existing NMR two-spin sequence. This includes important sequences such as HSQC, HMBP, HMQC, INADEQUATE, COSY, and NOESY, which are some of the most basic pulse sequences used for finding correlations between nuclei within a given molecule. Each hard pulse performs a universal rotation (UR), either 90° or 180° , of all magnetization components about a fixed axis, with an approximately ideal performance over the bandwidth of the pulse. As a replacement for hard pulses, better-performing UR

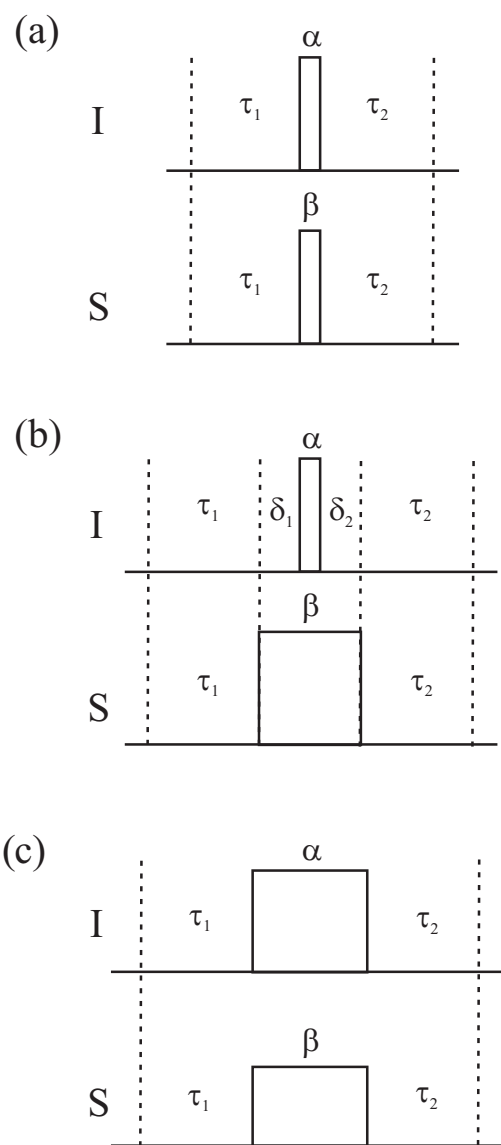


Figure 7.1: This schematic demonstrates a simple block of hard pulses with flip angles α and β , and delays τ_1 and τ_2 (Fig. (a)) in an any given pulse sequence. Hard pulses can be easily replaced by identical duration Fanta4 pulses with corresponding flip angles (Fig. (c)) without altering the delays τ_1 and τ_2 . To accommodate long duration shaped pulses on ^{13}C with respect to ^1H hard pulses, delays need to be adjusted by δ_1 and δ_2 in order to account for the extra duration and possible J coupling evolution (Fig. (b)).

pulses therefore minimize the number of pulses needed. However, UR pulses are only necessary for refocusing or combined excitation/flip-back. Point-to-point (PP) pulses are sufficient for excitation, flip-back, or inversion of a given initial state to a given final state, and these can be designed more easily and with better performance for their specific task than UR pulses.

We used the optimal control based GRAPE algorithm [183] to design UR 90° and 180°, and PP 90° and 180° pulses with bandwidths and pulse length suitable for ¹H and ¹³C spectroscopy of small-to medium-sized molecules at 600 MHz, which is currently a generally accessible and widely utilized spectrometer field strength. This results in a total of four pulses, which we whimsically refer to as Fanta4 due to the significant improvement they provide in pulse sequence performance. All pulses are of the same length, allowing each hard pulse in a sequence to be replaced by the corresponding UR or PP pulse without any further modification of the sequence.

7.2 Optimization

For the first generation of Fanta4 pulses we consider applications to ¹³C and ¹H on a 600 MHz spectrometer. In order to universally implement shaped pulses on any available probe-head, we limit the maximum RF amplitude for ¹³C spins to 10 kHz and numerically optimize shaped pulses for ¹³C nuclei that cover 35 kHz (233.33 ppm) chemical shift bandwidth and are robust to ±10% RF inhomogeneity/miscalibration. For ¹H nuclei, 18 kHz maximum RF amplitude was allowed and we optimized shaped pulses, which cover 20 kHz (33.33 ppm) chemical shift bandwidth and are robust to ±15% RF inhomogeneity/miscalibration. The duration used in numerical optimization of all shaped pulses is 1 ms. This is the minimum duration needed to optimize a UR 180° ¹³C shaped pulse [189, 218] in the presence of the above mentioned constraints of sufficient fidelity.

We know that $R = 0$ pulses [182] have no heteronuclear J coupling evolution during a pulse when applied to a single spin. However, when applied simultaneously to ¹H and ¹³C, we have to account for J coupling evolution (e.g., Hartmann-Hahn transfer). This can be solved by optimizing shaped pulses for a coupled two spin-1/2 system simultaneously. However, optimization of shaped pulses for coupled two spin systems with the mentioned constraints is computationally expensive. Details of coupled two spin-1/2 optimizations are provided in the appendix 7.7.1.

We simplify the coupled two spin-1/2 problem by approximating it as two independent, non-interacting single spin-1/2 problems, each of which demands less computation power by several orders of magnitude. We simulate their performance on a coupled two spin-1/2 system with a J coupling of 197 Hz.

For example, a PP 90° shaped pulse along x axis should bring magnetization along z to -y axis. In the case of a coupled two spin system, a combination of PP 90° pulse on ¹H and ¹³C should rotate e.g. initial zz magnetization to yy with a minimum of unwanted terms, yz or zy, with maximum fidelity. The best shaped pulses which fell within the threshold value of fidelity were included in the Fanta4 pulse set. More details of Fanta4 pulse selection and simulation are given in appendix 7.7.2.

However, if only one pulse is applied to either of the spins, transverse magnetizations of the other spin can evolve under the chemical shift Hamiltonian. This can be avoided by a “Do-Nothing” pulse, which create an effective rotation which is an arbitrary multiple of 360°, which can be e.g. realized by two identical PP inversion pulses with a duration of 500 μs each.

Numerical optimization were performed using the GRAPE (GRadient Ascent Pulse Engineering) algorithm (Chapter 2).

7.3 Experiments

We chose the HSQC (Fig. 7.2) and HMBC (Fig. 7.3) experiments to demonstrate the implementation of Fanta4 pulses. HSQC is widely used for recording one-bond correlation spectra between two heteronuclei and HMBC is mostly used for correlating heteronuclei connected by multiple bonds, mostly 2-4 bonds. Hard pulses are replaced by corresponding Fanta4 pulses in these pulse sequences (Fig. 7.2 and Fig. 7.3). Sodium formate and Hydroxycitronellal (Fig. 7.4 a and b) were used to test the performance of Fanta4-HSQC against conventional-HSQC and an intermediate molecule (Fig. 7.4c) from a reaction published in Ref. [219] is used to test Fanta4-HMBC against conventional-HMBC. All experiments were performed on Bruker AVANCE III 600 MHz spectrometer with a triple resonance TXI probehead and Z-gradient at 298°K.

7.4 Results

7.4.1 HSQC: Testing with Sodium Formate

^{13}C -labeled Sodium formate (Fig. 7.4a), with one proton and one carbon spin, and a large J coupling (197 Hz), dissolved in D_2O was used to check the performance of the Fanta4-HSQC sequence (Fig. 7.2 b) compared to the conventional-HSQC (Fig. 7.2a) at different chemical shifts and RF miscalibrations. A proton excited and detected HSQC (coupled during acquisition) gives doublet of a proton with respect to a carbon. We performed 1D-HSQC experiments by changing the carrier frequency in the ^{13}C dimension, a) with ideal RF amplitude on ^1H and ^{13}C (Fig. 7.5a and b), and b) by miscalibrating the RF amplitude on ^1H and ^{13}C by -15% and -10% (Fig. 7.5c and d).

The conventional-HSQC (Fig. 7.2a) shows reduced signal intensity at a large offset frequencies (Fig. 7.5a). In addition to offset effect, RF inhomogeneity/miscalibration on ^1H and ^{13}C pulses deteriorated the signal intensity (Fig. 7.5c). Small errors in the RF pulse accumulate during the pulse sequences are responsible for reduced signal intensity with considerable phase errors. We performed similar experiments using Fanta4-HSQC (Fig. 7.2b). It shows consistent signal intensity over large chemical shift range with an ideal RF amplitude (Fig. 7.5b) and with a miscalibrated RF amplitude (Fig. 7.5d) on ^1H and ^{13}C compared to the relatively small robustness of conventional-HSQC. For more details see Figure 7.5.

7.4.2 HSQC: Testing with Hydroxycitronellal

We implemented the above sequences on a more complex molecule, Hydroxycitronellal (Fig. 7.4b). It consists of a long chain of hydrocarbons with a hydroxyl group on one end and an aldehyde moiety at other end. Hydrocarbons resonate around 19 ppm and a carbon bonded to oxygen (aldehyde moiety) resonates at 202 ppm, which corresponds to total offset bandwidth of 27.3 kHz on a 600 MHz spectrometer. The conventional-HSQC experiment with an ideal RF amplitude is unable to excite the ^{13}C nuclei at very large offsets and resulted in a poor signal to noise ratio (S/N)(Fig. 7.6a). This task is even more difficult when the RF amplitude is miscalibrated on both nuclei (Fig. 7.6c). The Fanta4-HSQC showed better signal to noise ratios at large offsets both with ideal

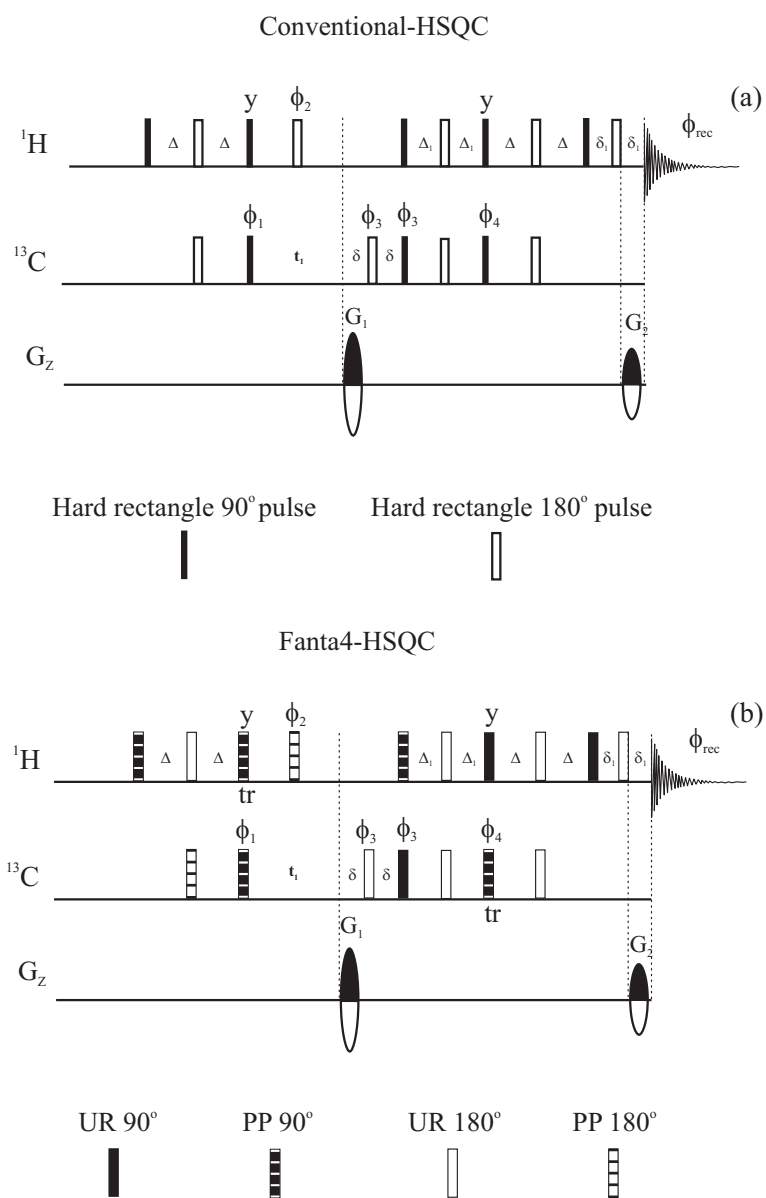


Figure 7.2: Proton excited and detected HSQC [220–222] experiment using conventional 90° and 180° hard pulses (conventional-HSQC, Fig. (a)) and Fanta4 pulses (Fanta4-HSQC, Fig. (b)). Phases are x with the exception of $\Phi_1 = x-x$, $\Phi_2 = x-x-x-x$, $\Phi_3 = x-x-x-x$, $\Phi_4 = y-y-y-y$, $\Phi_{rec} = x-x-x-x$. Delays are $\Delta = 1/(4J)$ for CH groups and $\Delta_1 = 1/(8J)$ for all multiplicities. δ and δ_1 are delays for gradients (G_1 and G_2) including recovery time. ‘tr’ is a time reverse shaped pulse. Both pulse sequences are practically of identical lengths but the offset-compensated and RF robust Fanta4-HSQC provides higher sensitivity.

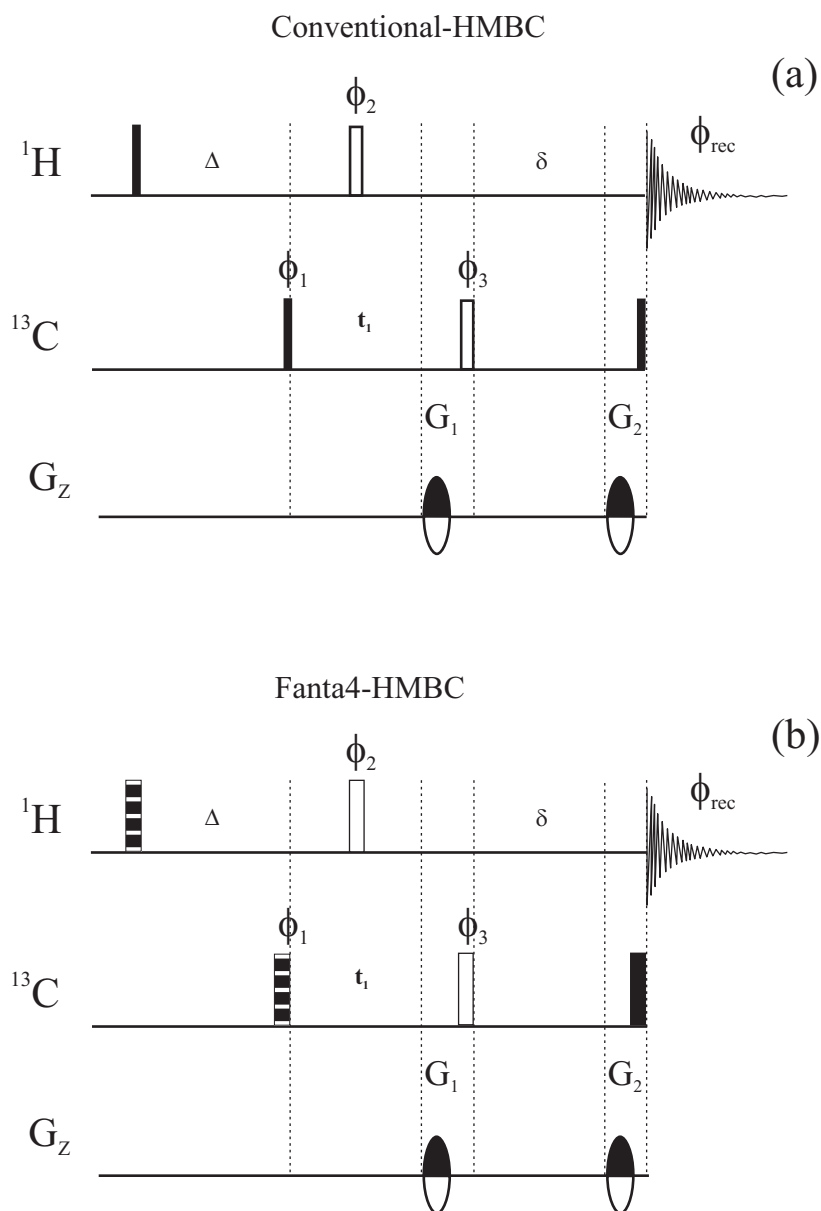


Figure 7.3: Proton excited and detected HMBC experiment [223] using conventional 90° and 180° hard pulse (conventional-HMBC (Fig. (a))) and Fanat4 pulses (Fanta4-HMBC (Fig. (b))). Phases are x with the exception of $\Phi_1 = x-x$, $\Phi_2 = x-x-x-x$, $\Phi_3 = x-x-x-x-x-x-x-x$, $\Phi_{rec} = x-x-x-x-x-x-x-x$. Delays are $\Delta = 1/2J$ for evolution of long range couplings. δ is delay for gradients (G_1 and G_2) including recovery time. Both pulse sequences are practically of identical lengths but the offset-compensated and RF robust Fanta4-HMBC provides higher sensitivity.

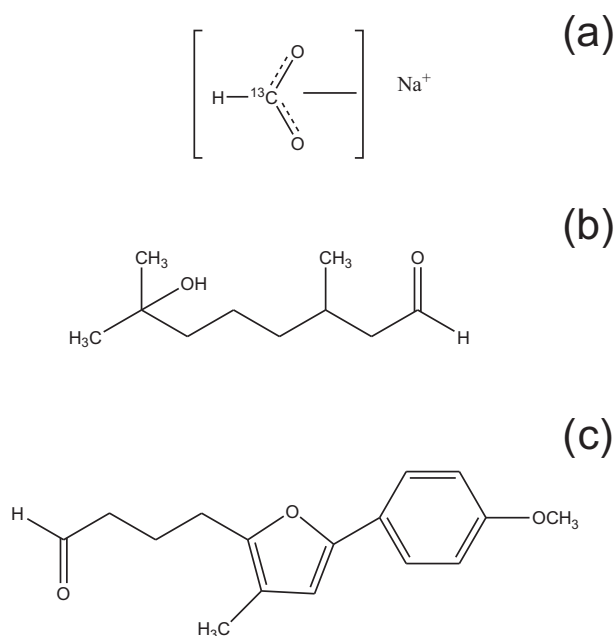


Figure 7.4: (a) Sodium formate, (b) Hydroxycitronellal, and (c) an intermediate from Ref. [219] are used for comparison of conventional HSQC and HMBC pulse sequences, and Fanta4 -HSQC and -HMBC pulses sequences.

RF amplitudes (Fig. 7.6b) and with miscalibrated RF amplitudes (Fig. 7.6d). For more details see Figure 7.6.

7.4.3 HMBC: Testing on Real molecule

We used an intermediate molecule (Fig. 7.4c) of a reaction published in Ref. [219] (Table 3, entry 2) to test the HMBC pulse sequence (Fig. 7.3). It is a relatively small molecule with large number of long-range J couplings between ^1H and ^{13}C spins. ^{13}C covers 28.8 kHz of offset range on a 600 MHz spectrometer. The conventional-HMBC pulse sequence with hard pulses (gray) shows poor performance at large offsets compared to the Fanta4-HMBC (dark) (Fig. 7.7.). Traces from the 2D HMBC spectrum acquired with hard pulses and with Fanta4 pulses are compared in Figure 7.8.

7.5 Discussion

The robustness of Fanta4 pulses with respects to a large frequency offsets and RF miscalibration renders them superior compared to hard pulses. However, the long duration (1 ms) of current Fanta4 pulses renders them vulnerable to relaxation, possible homonuclear and heteronuclear J coupling evolution. It limits the use of the current version of Fanta4 pulses to small and medium sized molecules with moderate relaxation values.

Fanta4-HSQC gives reduced signal intensity (about 10%) with ideal RF amplitude over the given offset range, when compared with the HSQC sequence which accommodate refocusing and/or inversion conventional shaped pulses on ^{13}C . However, with RF inhomogeneity/miscalibration on ^1H and ^{13}C Fanta4-HSQC outperforms the latter by more than 25% signal intensity gain.

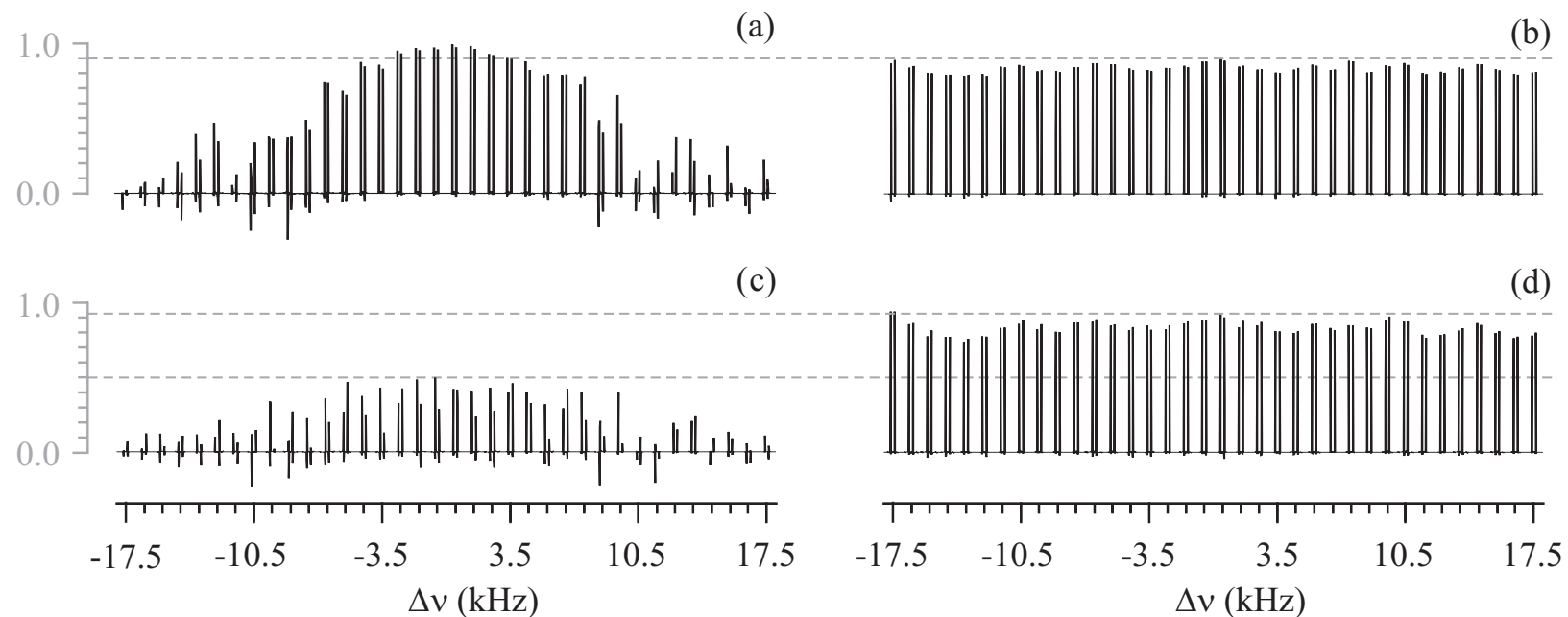


Figure 7.5: Chemical shift ($\Delta\nu$) excitation profile comparison of the conventional-HSQC (Fig. (a) and (c)) and the Fanta4-HSQC (Fig. (b) and (d)) acquired on a ^{13}C labeled Sodium formate dissolved in D_2O . HSQC (coupled during acquisition) gives doublet of a proton with respect to a carbon. Figures (a) and (b) compare signal intensity at different ^{13}C resonance offsets with ideal RF amplitude, and Figures (c) and (d) show the effect of RF inhomogeneity/miscalibration for ^1H (-15%) and ^{13}C (-10%) pulses for different ^{13}C offsets. In conventional-HSQC, the ideal RF amplitude on ^1H pulses was 29.59 kHz and ^{13}C pulses was 19.53 kHz. In case of Fanta4-HSQC, shaped pulses on ^1H had a maximum amplitude of 18 kHz, while on ^{13}C 10 kHz.

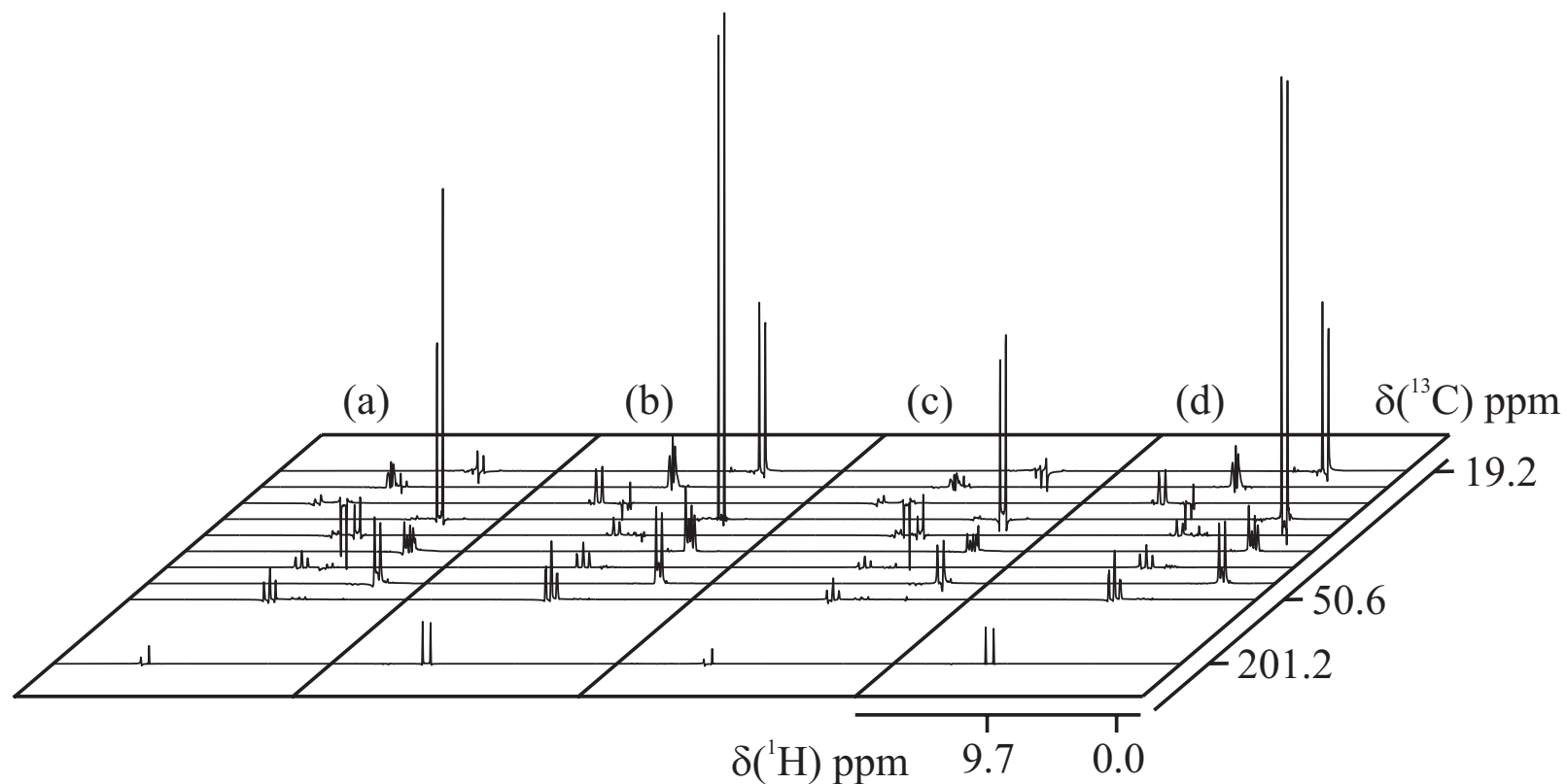


Figure 7.6: 2D HSQC projection acquired on ^{13}C natural abundant Hydroxycitronellal, dissolved in deuterated tetrahydrofuran, using conventional (Fig. (a) and (c)) and Fanta4 (Fig. (b) and (d)) -HSQC. Figure (a) shows the loss in signal intensity at edge of the ^{13}C dimension compared to Fig. (b) with ideal RF amplitude. It is worst in case of -15% RF miscalibration on ^1H and -10% on ^{13}C pulses (compare Fig. (c) and (d)). Amplitude on ^1H pulses was 29 kHz and ^{13}C pulses was 19.53 kHz in conventional-HSQC. While Fanta4 pulses were with 18 kHz and 10 kHz on ^1H and ^{13}C respectively. Peaks in ^1H and ^{13}C dimension are shifted for clear distinction. Their lower and upper limits are mentioned in a plot. 1024×256 data points were acquired with corresponding spectral widths of 201.2 ppm (^{13}C) and 9.7 ppm (^1H). The carrier frequency on ^1H was 4.5 ppm and on ^{13}C was 100 ppm. Two transients per increment gave an overall experiment time of 25 min for each of the two experiments.

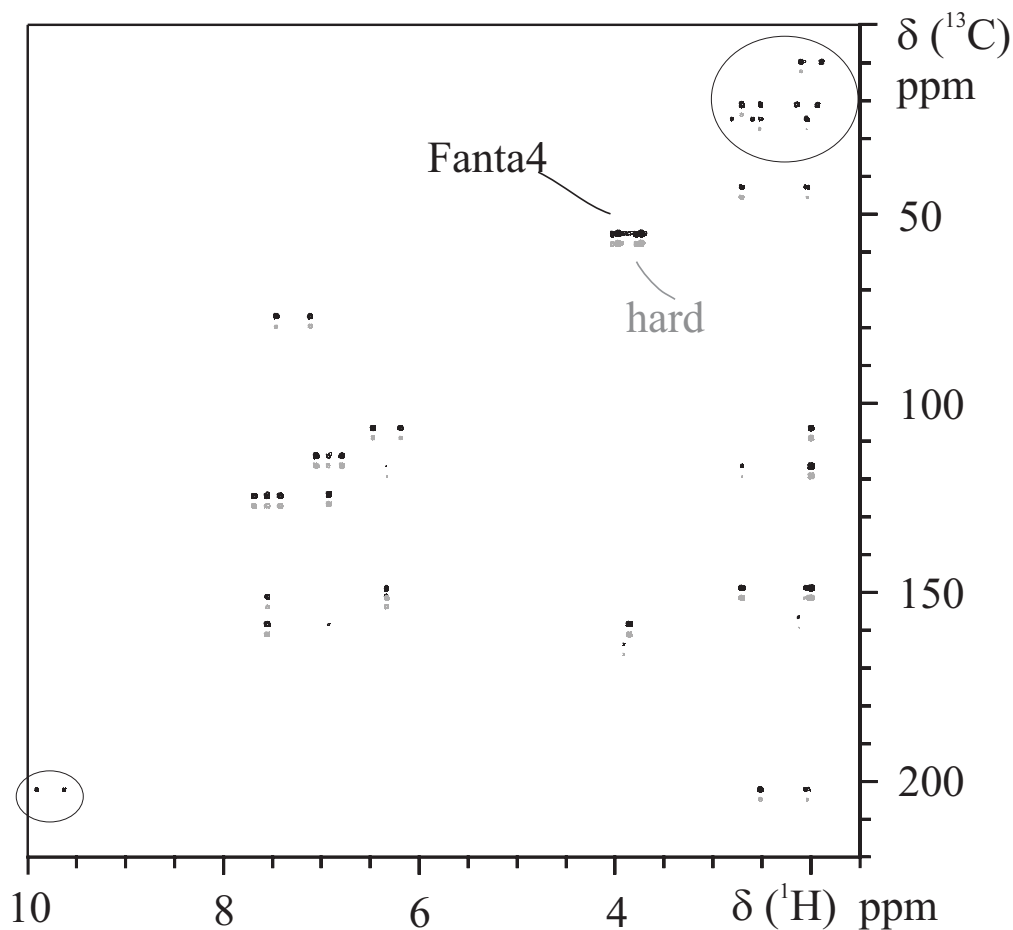


Figure 7.7: A magnitude mode 2D HMBC acquired on an intermediate molecule in a reaction published in Ref [219], dissolved in CDCl_3 , is shown in the figure using conventional-HMBC (gray) and Fanta4-HMBC (black) with a slight shift in ^{13}C dimension. The hard pulse version show loss in signal intensity compare to Fanta4-HMBC near $\delta^{13}\text{C} = 10$ to 30 ppm and at $\delta^{13}\text{C} = 202$ ppm (encircled). 1024×256 data points were acquired with corresponding spectral widths of 201.2 ppm (^{13}C) and 9.7 ppm (^1H). The carrier frequency on ^1H was 4.5 ppm and on ^{13}C dimension was 100 ppm. Forty transients per increment gave an overall experiment time of 6 hrs 25 min for each of the two experiments. For amplitude of pulses compare Figure 7.6.

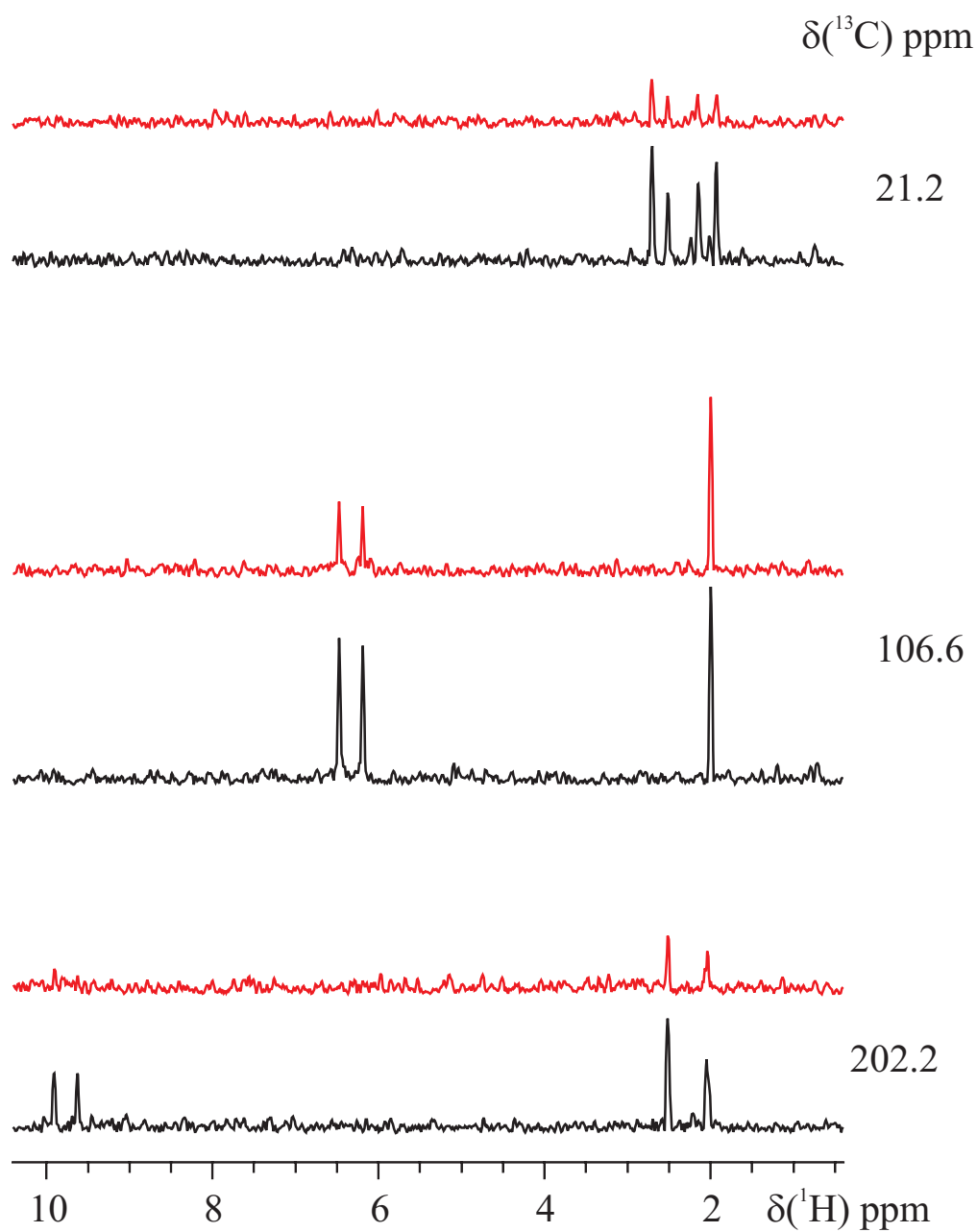


Figure 7.8: (Color online) Traces through cross signals at 21.2, 106.6 and 202.2 ppm are compared for conventional-HMBC (red, top) and Fanta4-HMBC (black, bottom) (Fig. 7.7). The Fanta4-HMBC sequence gives improved S/N ratio compared to the conventional-HMBC sequence.

7.6 Conclusion

We show that experimentally it is easy to replace each hard pulse with a corresponding Fanta4 shaped pulse without further modifying the sequence of an existing pulse sequence. The duration of the current version of Fanta4 shaped pulse is 1 ms, which renders them suitable for small and medium sized molecules. For Fanta4 pulses, there is signal loss of about 10% compared to the conventional sequence on resonance due to relaxation effects. However signal gains over large offset ranges and RF inhomogeneity/miscalibration are substantial.

7.7 Appendix

7.7.1 Optimization of pulse pairs for two coupled heteronuclear spins-1/2

Transfer from single initial to single final state

For the optimal control problem considered here, which involves two coupled spins-1/2 nuclei with defined J-coupling; with a given initial sets of product operators and final state, the goal is to find a RF pulse which steers the trajectory from the initial $I(0)_\alpha S(0)_\beta$ to the final state $I(\tau)_\gamma S(\tau)_\delta$. This is done by optimizing a suitably chosen cost function Φ , where α, β, γ , and δ correspond to x, y , and z component of magnetization. The state for the spin system is characterized by the density operator $\rho(t)$ at time point t , and its equation of motion is the Liouville-von Neuman equation defined in Section 2.3 of Chapter 2.

Transfer from two initial to two final states

Now let us consider that the goal is to find a RF pulse which steers the trajectory of two initial $I(0)_\alpha S(0)_\beta$ and $I(0)_\gamma S(0)_\delta$ to the two final states $I(\tau)_\epsilon S(\tau)_\zeta$ and $I(\tau)_\eta S(\tau)_\theta$ for a given spin system, $\alpha, \beta, \gamma, \delta, \epsilon, \zeta, \eta$, and θ correspond to x, y , and z components. Each state of the spin system is characterized by the density operator $\rho_1(t)$ and $\rho_2(t)$ at time point t . The Liouville-von Neuman equation for each state is given by

$$\dot{\rho}_n(t) = -i[(H_0 + \sum_{k=1}^m u_k(t)H_k), \rho_n(t)], \quad (7.1)$$

where $n = 1, 2, \dots, P$, labels the states. The standard inner product to measure the maximum overlap of given initial states to corresponding final states is

$$\langle F_n | \rho_n(T) \rangle = \text{tr}\{F_n^\dagger \rho_n(T)\}. \quad (7.2)$$

Hence, the performance index Φ_n of the each transfer process can be defined as

$$\Phi_n = \langle F_n | \rho_n(T) \rangle. \quad (7.3)$$

and the overall performance index Φ_{avg} will be

$$\Phi_{avg} = \frac{\sum_{n=1}^P \Phi_n}{P}. \quad (7.4)$$

At time step j the density operators are ρ_{1j} and ρ_{2j} and its corresponding backward propagators are λ_{1j} and λ_{2j} . Following the steps 1. through 3. from algorithm of Section 2.3 in Chapter 2, calculate the gradients G_{nj} by

$$G_{nj} = \frac{\delta\Phi_n}{\delta u_k(j)} = -\langle \lambda_{nj} | i\Delta t [H_k, \rho_{nj}] \rangle. \quad (7.5)$$

and the overall gradient for all states at time j will be

$$G_{avg}(j) = \frac{\sum_{n=1}^P G_{nj}}{P}. \quad (7.6)$$

Using $G_{avg}(j)$ controls $u_k(j)$ at time step j can be improved

$$u_k(j) \rightarrow u_k(j) + \epsilon G_{avg}(j). \quad (7.7)$$

Similarly we can calculate gradients for each time steps in a given control to get gradient vector over all n transfers, which later use to update the next control amplitudes.

The modified GRAPE algorithm for n number of states is

1. Guess initial controls $u_k(j)$
2. Starting from ρ_{n0} , calculate $\rho_{nj} = U_j \cdots U_1 \rho_{n0} U_1^\dagger \cdots U_j^\dagger$ for all $j \leq N$ and $n = 1, 2, \dots, P$.
3. Starting from $\lambda_{nN} = F_n$, calculate $\lambda_{nj} = U_{j+1}^\dagger \cdots U_N^\dagger F_n U_N \cdots U_{j+1}$ for all $j \leq N$ and $n = 1, 2, \dots, P$.
4. Evaluate $G_{nj} = \frac{\delta\Phi_n}{\delta u_k(j)}$ for $n = 1, 2, \dots, P$.
5. Evaluate $G_{avg}(j)$ and update $m \times N$ control amplitudes $u_k(j)$ according to Eq. 7.7.
6. With these as the new controls, go to step 2.

The algorithm is terminated if the change in the performance index Φ_{avg} is smaller than a chosen threshold value.

Figure 7.9 shows the shape of the pulses optimized simultaneously using above algorithm for ^1H and ^{13}C with J coupling of 197 Hz for the following transfers.

$$-I_z S_x \rightarrow -I_y S_x \quad (7.8)$$

$$I_z S_y \rightarrow -I_y S_z \quad (7.9)$$

Figure 7.10 shows the simulations for the corresponding transfers. For more details see Figures 7.9 and 7.10.

7.7.2 Fanta4 pulse selection

A number of PP 90° and 180° , and UR 90° and 180° shaped pulses are optimized for ^1H and ^{13}C . Shaped pulses with fidelity ≥ 0.9999 are chosen for simulation on coupled two spins-1/2 system. By considering a pair of pulses in any given pulse sequence (Fig. 7.1c), we simulated the performance of all sixteen combinations of four types of ^1H with four types of ^{13}C shaped pulses. Simulations were performed at ideal RF amplitude

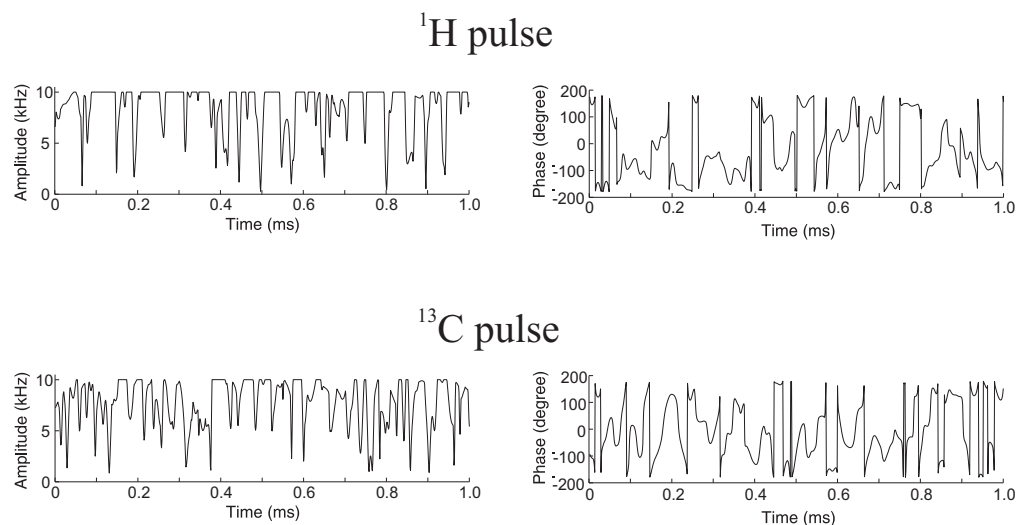


Figure 7.9: The amplitude and phase of ^1H and ^{13}C pulses optimized simultaneously are plotted as a function of the pulse duration. All are 1 ms long with a maximum amplitude of 10 kHz.

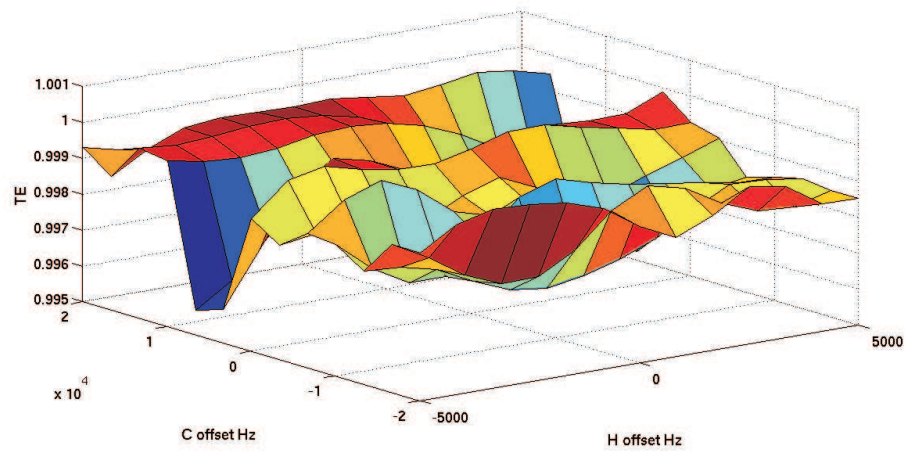
with J coupling of 200 Hz over the offset range of 20 kHz and 35 kHz for ^1H and ^{13}C respectively with offset step of 250 Hz. Each component of cartesian product operator of coupled two spins-1/2 system was considered as initial state and the performance of pulse combination was determined by detecting all components.

Figures 7.11, 7.12, 7.13, and 7.14 show all possible combinations of ^1H and ^{13}C pulses. For each pulse combination, starting with initial component, the desired (D), undesired (empty box), and components which can be ignored (I) during simulation are indicated. Later we used combinatorial approach to select the best pulse set (depicted in Fig. 7.15).

The process of best pulse set selection is summarized in following steps,

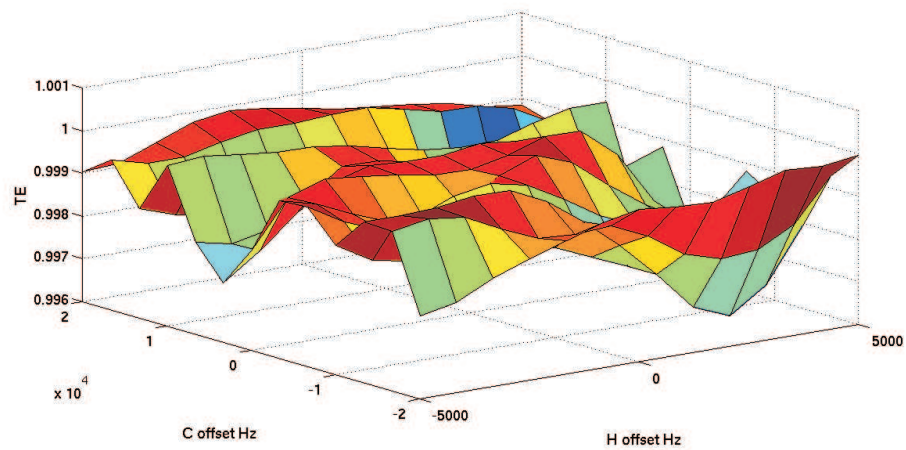
1. Optimize a number of ^1H and ^{13}C pulses with defined constraints.
2. Select the ^1H and ^{13}C pulses with fidelity ≥ 0.9999 .
3. Simulate each combination of ^1H and ^{13}C pulses simultaneously for every single component of cartesian product operator for two spin-1/2 system with defined J coupling (in this case $J= 200$ Hz), and over given offset range for both nuclei (see Figures 7.11, 7.12, 7.13, and 7.14).
4. Calculate the average fidelity over the offsets for all pulse combinations.
5. Based on the pulse combination sort out the desired (D), undesired (empty box), and terms which can be ignored (I) with their respective fidelities. For example, see Figure 7.11 for the pulse combination of PP 90° of ^1H and ^{13}C .
6. For all pulse combinations, calculate the total fidelity over all components of cartesian product operator using the appropriate quality factor (see Figure 7.15a). In our case we considered three quality factors,

$$-I_z S_x \rightarrow -I_y S_x$$



13 offset points in each direction

$$I_z S_y \rightarrow -I_y S_z$$



13 offset points in each direction

Figure 7.10: (Color online) Theoretical performances of ^1H and ^{13}C pulses optimized simultaneously for a transfer $-I_z S_x \rightarrow -I_y S_x$ and $I_z S_y \rightarrow -I_y S_z$ are plotted as a function of ^1H and ^{13}C offsets.

$$Q_1(\text{pc}) = \text{Min}(Q_d) - \text{Max}(Q_{ud})$$

$$Q_2(\text{pc}) = \text{Min}(\overline{Q_d}) - \text{Max}(\overline{Q_{ud}})$$

$$Q_3(\text{pc}) = 1 - (\overline{1 - Q_d^2}) - (\overline{0 - Q_{ud}^2})$$

where, pc is indices for the pulse combination, Q_d and Q_{ud} are the fidelities for desired and undesired terms. $\overline{Q_d}$ and $\overline{Q_{ud}}$ are averages of desired and undesired terms. Min and Max are minimum and maximum of the values.

7. For the selected pulses with desired fidelity (Q_1 or Q_2 or Q_3), we use the combinatorial approach to find best set of pulses. (see Figure 7.15).
8. For every pulse set calculate fidelity $Q_{final} = \sum Q_{ij}$, where i and j are indices for the pulse combinations (see Figure 7.15b).
9. Choose the pulse set with highest Q_{final} .

Based on this procedure the effect of heteronuclear J-coupling during shaped pulses could be reduced by choosing appropriate pulse combination.

Q_2 is summarized for the current set of ^1H and ^{13}C Fanta4 pulses in following table.

Table 7.1: Q_2 is summarized for the current set of ^1H and ^{13}C Fanta4 pulses.

Q_2	PP _C 90°	PP _C 180°	UR _C 90°	UR _C 180°
PP _H 90°	0.4479	0.7916	0.8534	0.8497
PP _H 180°	0.8000	0.7914	0.8585	0.8606
UR _H 90°	0.8831	0.8810	0.9311	0.9278
UR _H 180°	0.8617	0.8716	0.9311	0.9400

7.7.3 Fanta4 pulse shapes and excitation profiles

All experiments were implemented on a Bruker 600 MHz AVANCE III spectrometer equipped with SGU units for RF control and linearized amplifiers, utilizing a triple-resonance TXI probehead and gradients along the z-axis. Measurements are the residual HDO signal using a sample of 99.96% D₂O doped with CuSO₄ to a T_1 relaxation time of 100 ms at 298° K. For the ^1H pulses shown in Figure 7.16, signals are obtained for offsets between -11.1 kHz to 11.1 kHz in steps of 200 Hz at ideal RF amplitude with RF_{max} of 18 kHz (Fig. 7.17). For the ^{13}C pulses shown in Figure 7.18, signals are obtained at offsets between -18.5 kHz to 18.5 kHz in steps of 200 Hz at ideal RF amplitude with RF_{max} of 10 kHz (Fig. 7.17). To reduce the effects of RF field inhomogeneity, approximately 40 μl of sample solution was placed in a 5 mm Shigemi limited volume tube. The duration of each Fanta4 pulse is 1 ms.

		PP _H 90° - PP _C 90°											
		Initial ¹ H		¹³ C	¹ H ¹³ C								
Final		x	y	z	xx	xy	xz	yx	yy	yz	zx	zy	zz
¹ H	x	I	I										
	y	I	I	D									
	z												
¹³ C	x			I	I								
	y			I	I	D							
	z												
¹ H ¹³ C	xx				I	I		I	I				
	xy				I	I	I	I	I				
	xz												
	yx				I	I		I	I		I	I	
	yy				I	I	I	I	I		I	I	D
	yz												
	zx												
	zy												
	zz												

		PP _H 90° - PP _C 180°											
		Initial ¹ H		¹³ C	¹ H ¹³ C								
Final		x	y	z	xx	xy	xz	yx	yy	yz	zx	zy	zz
¹ H	x	I	I										
	y	I	I	D									
	z												
¹³ C	x			I	I								
	y			I	I								
	z												
¹ H ¹³ C	xx				I	I		I	I				
	xy				I	I		I	I				
	xz												
	yx				I	I		I	I		I	I	
	yy				I	I		I	I		I	I	
	yz												D
	zx												
	zy												
	zz												

		PP _H 90° - UR _C 90°											
		Initial ¹ H		¹³ C	¹ H ¹³ C								
Final		x	y	z	xx	xy	xz	yx	yy	yz	zx	zy	zz
¹ H	x	I	I										
	y	I	I	D									
	z												
¹³ C	x			D									
	y												
	z												
¹ H ¹³ C	xx				I	I		I	I				
	xy				I	I		I	I				
	xz												
	yx				I	I		I	I		D	D	
	yy				I	I		I	I				D
	yz				I	I		I	I				D
	zx												
	zy												
	zz												

		PP _H 90° - UR _C 180°											
		Initial ¹ H		¹³ C	¹ H ¹³ C								
Final		x	y	z	xx	xy	xz	yx	yy	yz	zx	zy	zz
¹ H	x	I	I										
	y	I	I	D									
	z												
¹³ C	x			D									
	y												
	z												
¹ H ¹³ C	xx				I	I		I	I				
	xy				I	I		I	I				
	xz												
	yx				I	I		I	I		D	D	
	yy				I	I		I	I				D
	yz				I	I		I	I				D
	zx												
	zy												
	zz												

Figure 7.11: (Color online) This figure shows the combinations of PP_H 90° pulse with rest of ¹³C pulses. For simulation of pair of pulses on coupled two spins-1/2 system, each component of cartesian product operator are considered as initial state and all components are detected. The desired(D, in red), undesired(empty box), and terms which can be ignored (I) are indicated in each case.

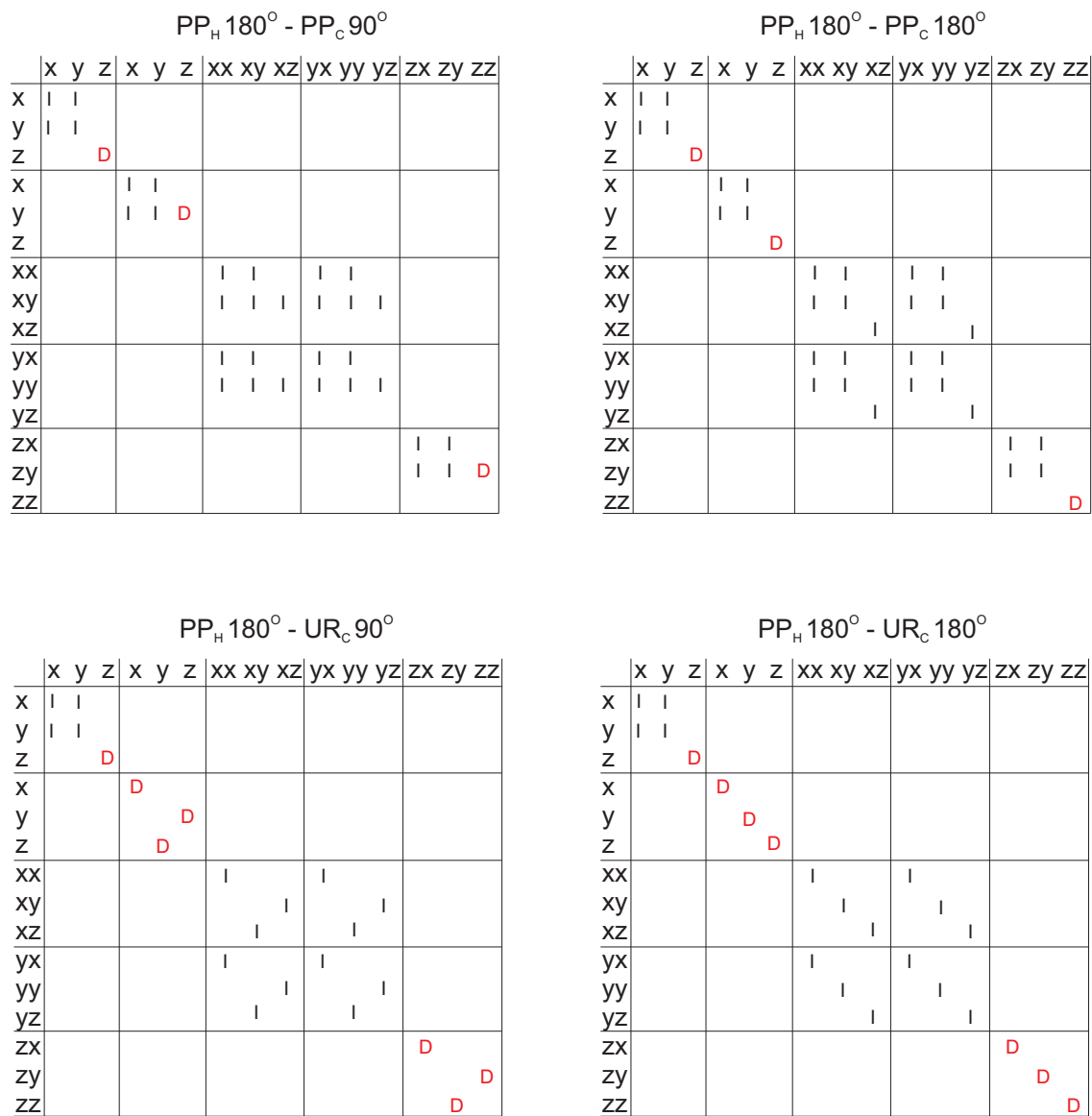


Figure 7.12: The combinations of PP_H 180° pulse with rest of ¹³C pulses. Compare Figure 7.11.

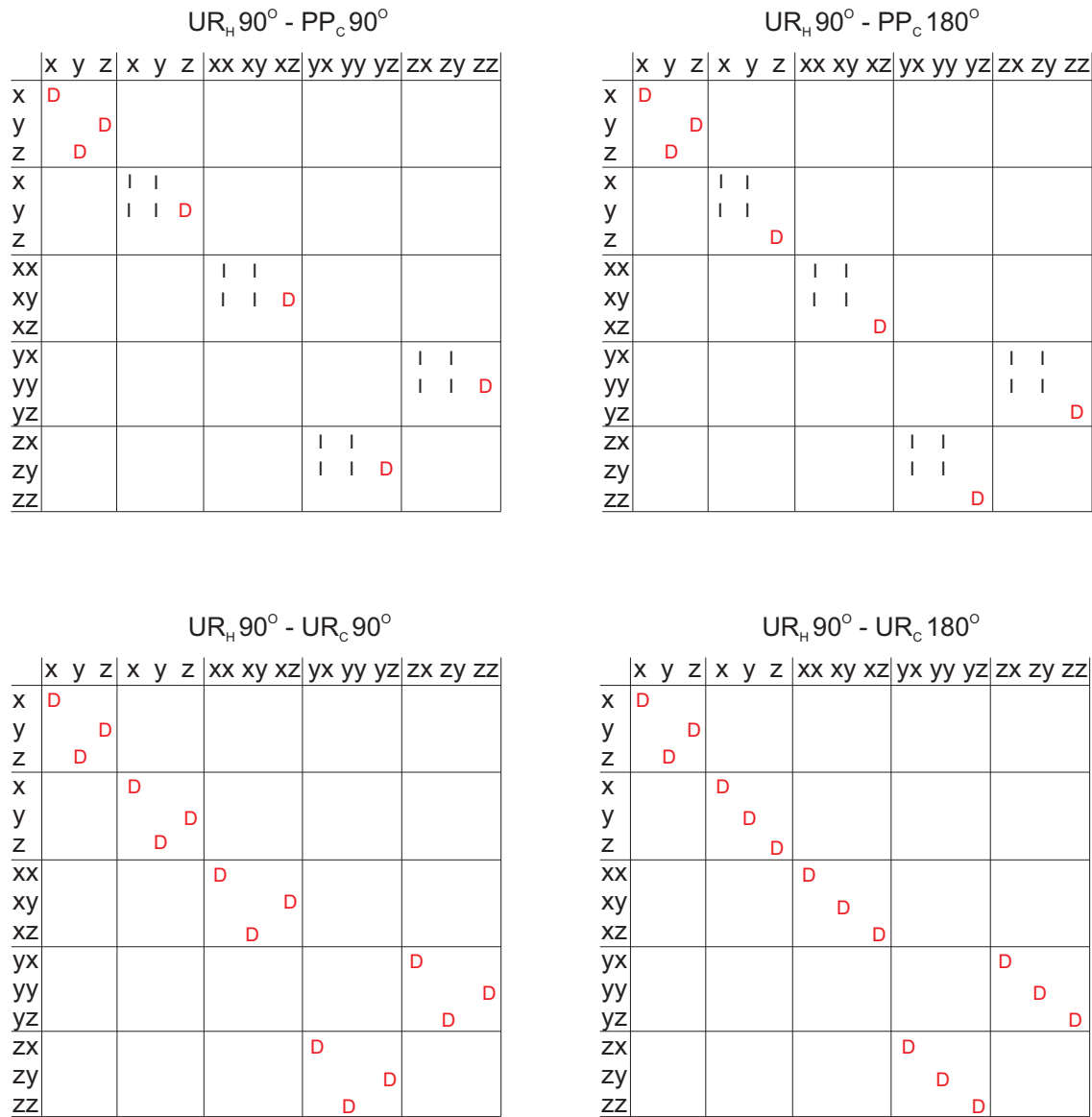


Figure 7.13: The combinations of $UR_H 90^\circ$ pulse with rest of ^{13}C pulses. Compare Figure 7.11.

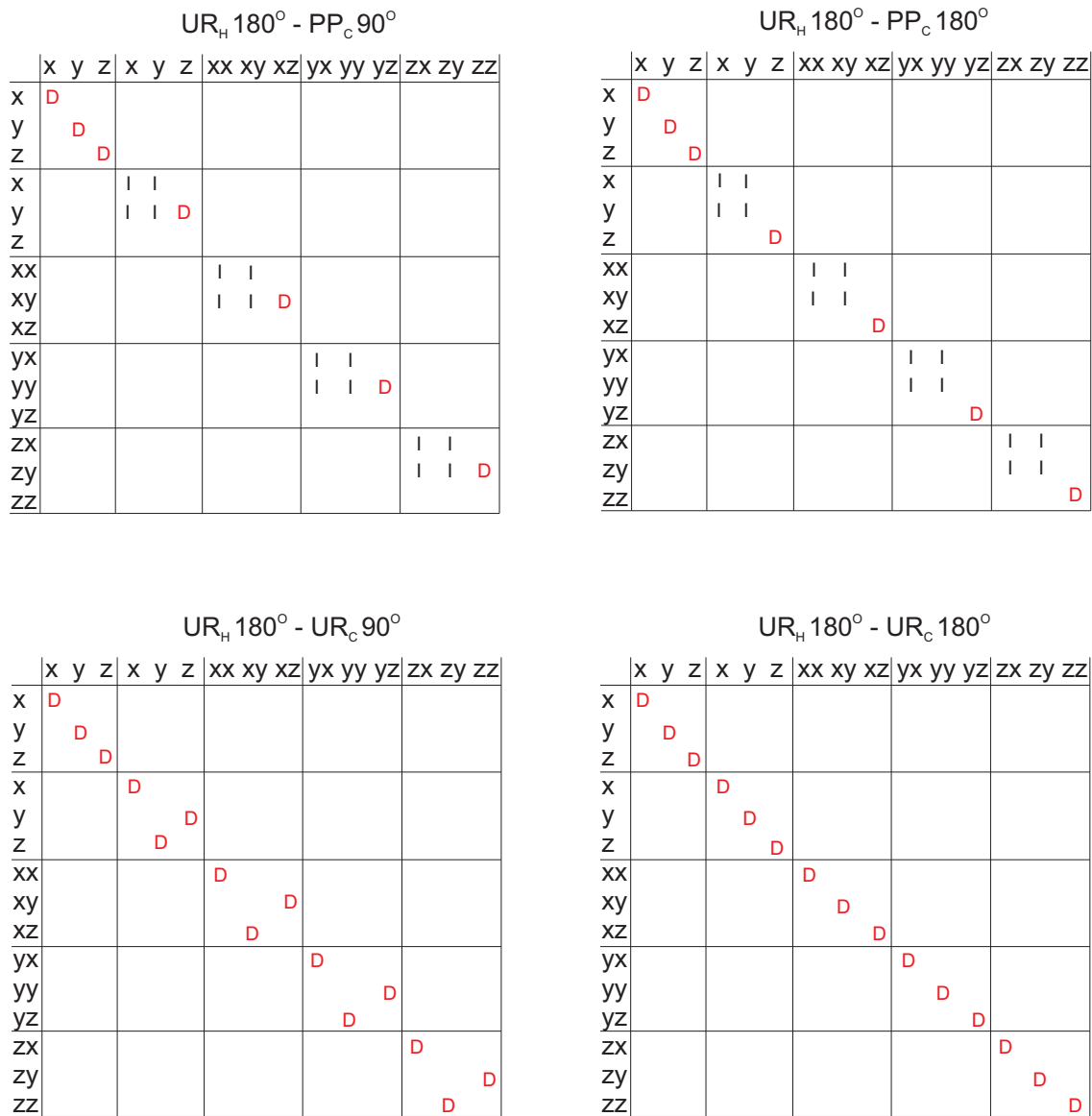


Figure 7.14: The combinations of $UR_H 180^\circ$ pulse with rest of ^{13}C pulses. Compare Figure 7.11.

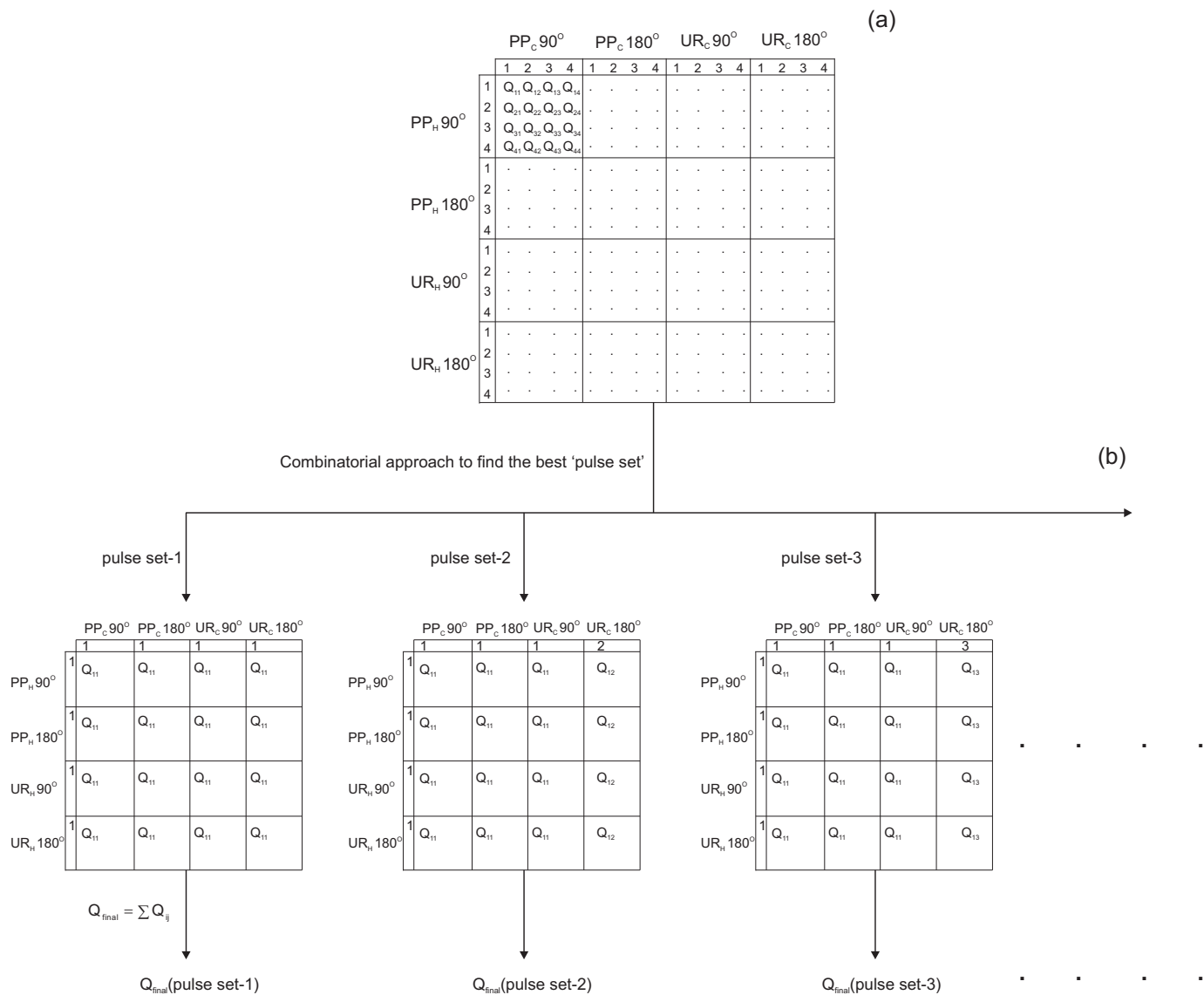


Figure 7.15: It depicts the combinatorial approach to select the best set of pulses. Figure (a) list the selected pulses with fidelity Q_{ij} , where i and j are indices for the pulse combination. Figure (b) shows the possible sets of pulses and calculation of the combined fidelity Q_{final} for each pulse set.

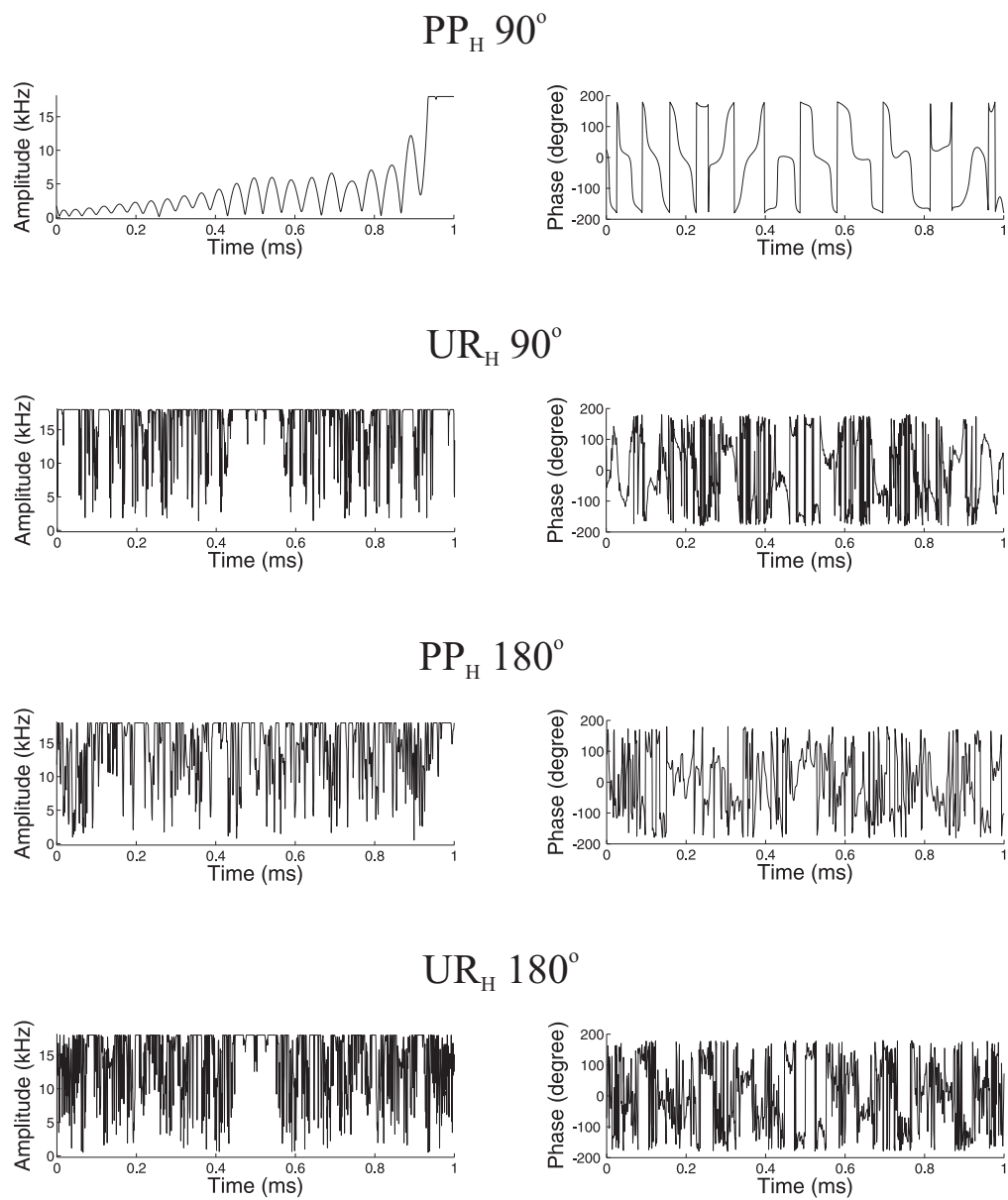


Figure 7.16: The amplitude and phase of ^1H pulses are plotted as a function of the pulse duration. All are 1 ms long with a maximum amplitude of 18 kHz.

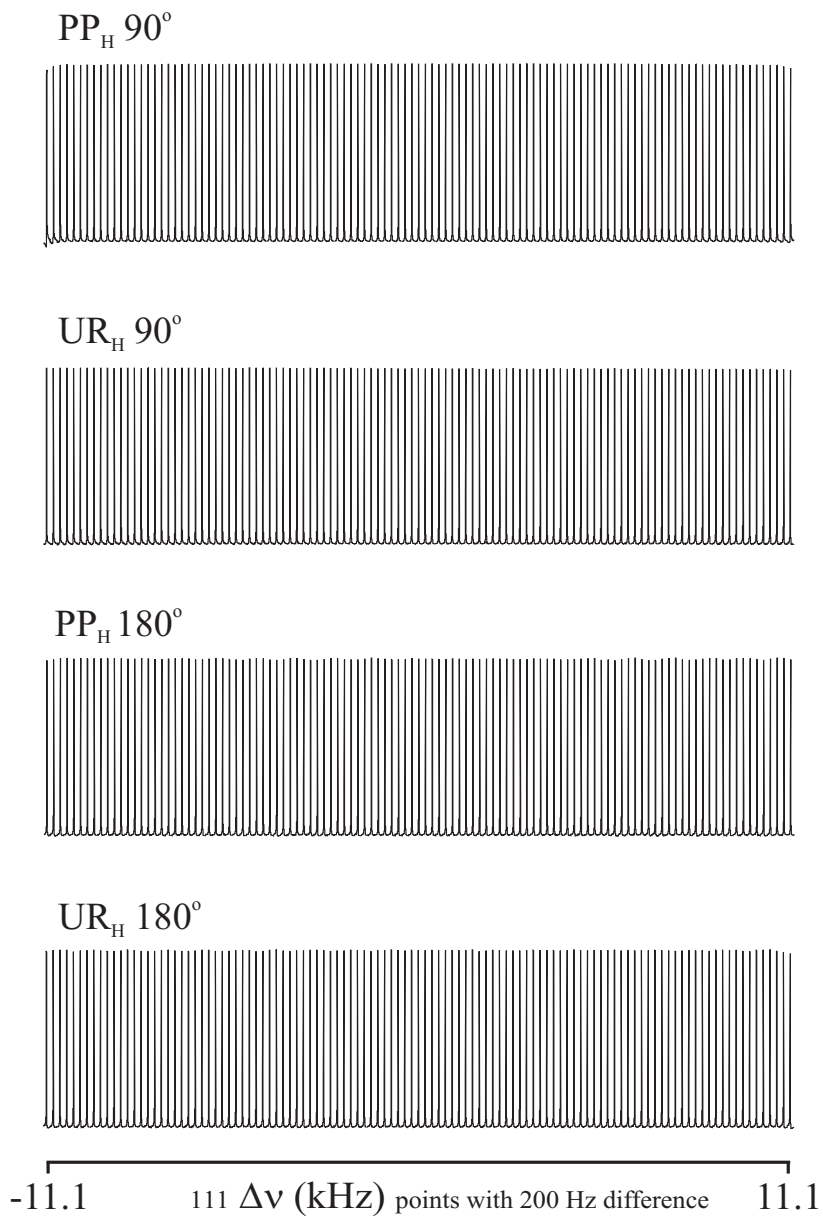
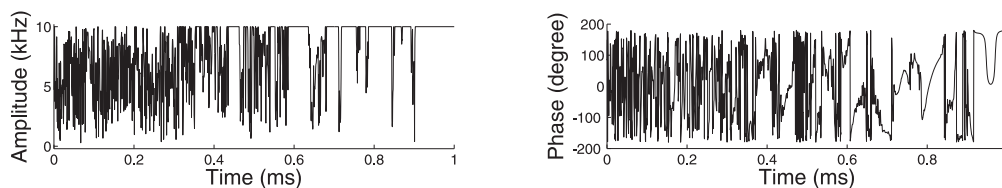
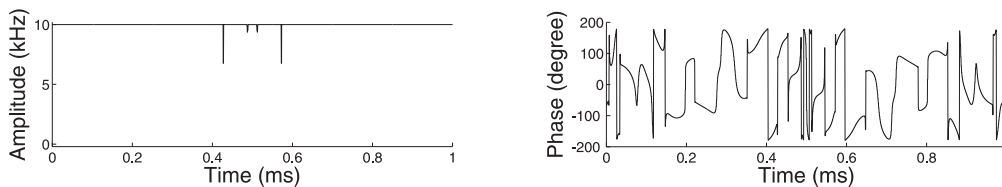


Figure 7.17: The experimental performance of ^1H pulses is plotted as function of the offset $\Delta\nu$ at ideal RF amplitude with a RF_{max} of 18 kHz. Experiments were acquired on residual proton in HDO for an offset range of 22.2 kHz in steps of 200 Hz. ^1H pulses are optimized for 20 kHz of total offset range with RF miscalibration of $\pm 5\%$ but they are naturally robust for $\pm 15\%$ RF miscalibration. ^1H PP 90° and UR 90° show the excitation profile for the $z \rightarrow -y$ and ^1H PP 180° and UR 180° show an inversion profile from $z \rightarrow -z$.

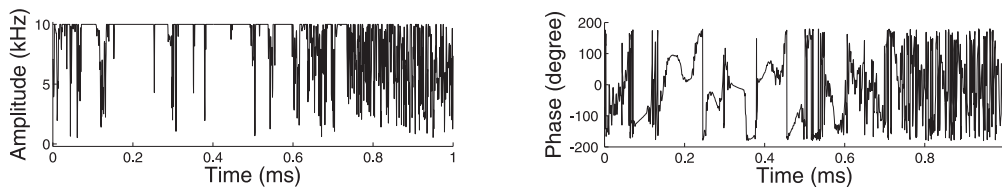
$PP_C 90^\circ$



$UR_C 90^\circ$



$PP_C 180^\circ$



$UR_C 180^\circ$

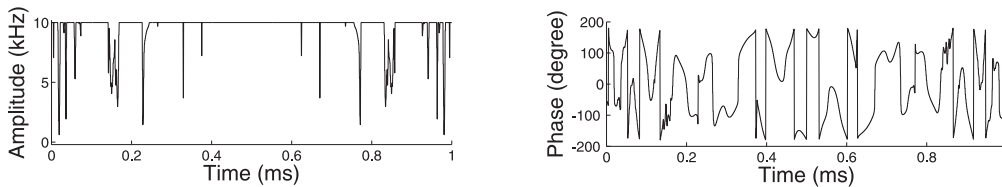


Figure 7.18: The amplitude and phase of ^{13}C pulses are plotted as a function of the pulse duration. All are 1 ms long with a maximum amplitude of 10 kHz.

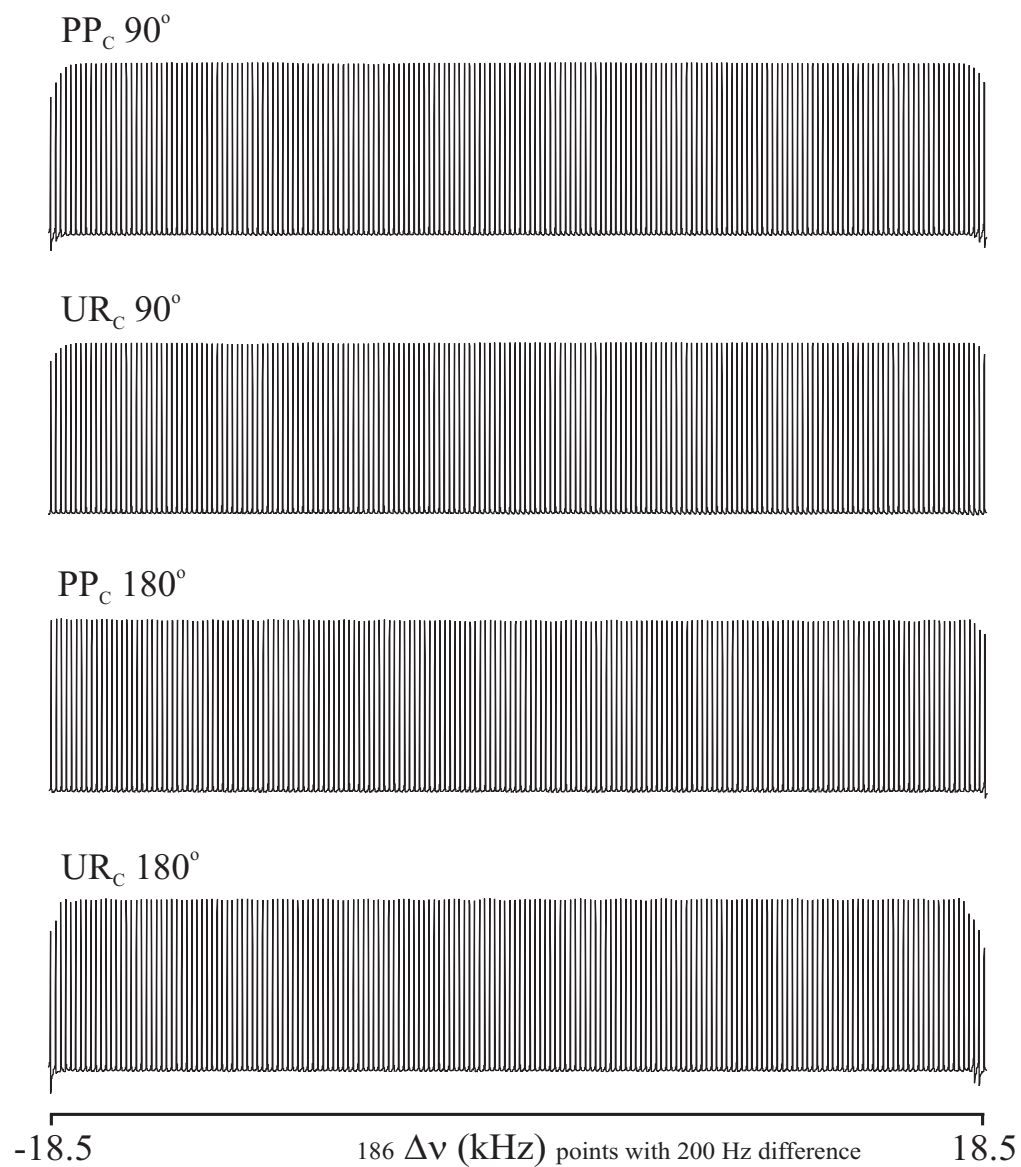


Figure 7.19: The experimental performance of ^{13}C pulses is plotted as function of the offset $\Delta\nu$ at ideal RF amplitude with a RF_{max} of 10 kHz. Experiments were acquired on residual proton in HDO for offset range of 37 kHz in steps of 200 Hz. ^1H pulses are optimized for 35 kHz of total offset range with RF miscalibration of $\pm 5\%$ but they are naturally robust for $\pm 10\%$ RF miscalibration. ^{13}C PP 90° and UR 90° show the excitation profile for the $z \rightarrow -y$ and ^{13}C PP 180° and UR 180° show an inversion profile from $z \rightarrow -z$.

Bibliography

- [1] N. C. Nielsen, C. Kehlet, S. J. Glaser, and N. Khaneja. Optimal Control Methods in NMR Spectroscopy. *Encyclopedia of Nuclear Magnetic Resonance*, 9:100, 2010.
- [2] E. Pinch. *Optimal Control and the Calculus of Variations*. Oxford University Press, Oxford, 1993.
- [3] H. Goldstein. *Classical Mechanics*. Addison-Wesley, Reading, MA,, 1980.
- [4] N. I. Gershenzon, K. Kobzar, B. Luy, S. J. Glaser, and T. E. Skinner. Optimal Control Design of Excitation Pulses that Accomodate Relaxation. *J. Magn. Reson.*, 188:330, 2007.
- [5] T. E. Skinner, T. O. Reiss, B. Luy, N. Khaneja, and S. J. Glaser. Application of Optimal Control Theory to the Design of Broadband Excitation Pulses for High Resolution NMR. *J. Magn. Reson.*, 163:8, 2003.
- [6] N. Khaneja, T. Reiss, C. Kehlet, T. Schulte-Herbrüggen, and S. J. Glaser. Optimal Control of Coupled Spin Dynamics: Design of NMR Pulse Sequences by Gradient Ascent Algorithms. *J. Magn. Reson.*, 172:296–305, 2005.
- [7] N. Khaneja, T. Reiss, B. Luy, and S. J. Glaser. Optimal Control of Spin Dynamics in the Presence of Relaxation. *J. Magn. Reson.*, 162:311–319, 2003.
- [8] N. I. Gershenzon, T. E. Skinner, B. Brutscher, N. Khaneja, M. Nimbalkar, B. Luy, and S. J. Glaser. Linear Phase Slope in Pulse Design: Application to Coherence Transfer. *J. Magn. Reson.*, 192:235, 2008.
- [9] E. Pinch. *Optimal Control and the Calculus of Variations*. Oxford University Press, Oxford, 1993.
- [10] T. E. Skinner, T. O. Reiss, B. Luy, N. Khaneja, and S. J. Glaser. Application of Optimal Control Theory to the Design of Broadband Excitation Pulses for High Resolution NMR. *J. Magn. Reson.*, 163:8, 2003.
- [11] T. E. Skinner, T. O. Reiss, B. Luy, N. Khaneja, and S. J. Glaser. Reducing the Duration of Broadband Excitation Pulses Using Optimal Control with Limited RF Amplitude. *J. Magn. Reson.*, 167:68–74, 2004.
- [12] K. Kobzar, T. E. Skinner, N. Khaneja, S. J. Glaser, and B. Luy. Exploring the Limits of Broadband Excitation and Inversion Pulses. *J. Magn. Reson.*, 170:236–243, 2004.

- [13] T. E. Skinner, T. O. Reiss, B. Luy, N. Khaneja, and S. J. Glaser. Tailoring the optimal control cost function to a desired output: application to minimizing phase errors in short broadband excitation pulses. *J. Magn. Reson.*, 172:17–23, 2005.
- [14] T. E. Skinner, K. Kobzar, B. Luy, R. Bendall, W. Bermel, N. Khaneja, and S. J. Glaser. Optimal Control Design of Constant Amplitude Phase-Modulated Pulses: Application to Calibration-Free Broadband Excitation. *J. Magn. Reson.*, 179:241, 2006.
- [15] Christopher Bauer, Ray Freeman, Tom Frenkiel, James Keeler, and A. J. Shaka. Gaussian pulses. *J. Magn. Reson.*, 58:442, 1984.
- [16] N. I. Gershenzon, K. Kobzar, B. Luy, S. J. Glaser, and T. E. Skinner. Optimal Control Design of Excitation Pulses that Accomodate Relaxation. *J. Magn. Reson.*, 188:330, 2007.
- [17] J. S. Waugh. Theory of broadband spin decoupling. *J. Magn. Reson.*, 50:30, 1982.
- [18] Ě. Kupĉe and R. Freeman. Polychromatic selective pulses. *J. Magn. Reson. Ser. A*, 102:122, 1993.
- [19] B. Luy, K. Kobzar, T. E. Skinner, N. Khaneja, and S. J. Glaser. Construction of Universal Rotations from Point to Point Transformations. *J. Magn. Reson.*, 176:179–186, 2005.
- [20] Thomas E. Skinner, Naum I. Gershenzon, Manoj Nimbalkar, Wolfgang Bermel, Burkhard Luy, and Steffen J. Glaser. Broadband 180° universal rotation pulses for NMR spectroscopy designed by optimal control. *J. Magn. Reson.*, in press, 2011.
- [21] M. Kock, R. Kerssebaum, and W. Bermel. A broadband ADEQUATE pulse sequence using chirp pulses. *Magn. Reson. Chem.*, 41:6569, 2003.
- [22] M. H. Levitt and R. Freeman. NMR population inversion using a composite pulse. *J. Magn. Reson.*, 33:473, 1979.
- [23] A. J. Shaka, J. Keeler, T. Frenkiel, and R. Freeman. An improved sequence for broadband decoupling:WALTZ-16. *J. Magn. Reson.*, 52:335, 1983.
- [24] A. J. Shaka, J. Keeler, and R. Freeman. Evaluation of a new broadband decoupling sequence: WALTZ-16. *J. Magn. Reson.*, 53:313, 1983.
- [25] J. Baum, R. Tycko, and A. Pines. Broadband population inversion by phase modulated pulses. *J. Chem. Phys.*, 79:4643, 1983.
- [26] M. H. Levitt and R. R. Ernst. Composite pulses constructed by a recursive expansion procedure. *J. Magn. Reson.*, 55:247, 1983.
- [27] M. S. Silver, R. I. Joseph, and D. I. Hoult. Selective spin inversion in nuclear magnetic resonance and coherence optics through an exact solution of the Bloch-Riccati equation. *Phys. Rev. A.*, 31:2753, 1985.
- [28] J. Baum, R. Tycko, and A. Pines. Broadband and adiabatic inversion of a two-level system by phase-modulated pulses. *Phys. Rev. A.*, 32:3435, 1985.

- [29] A. J. Shaka. Composite pulses for ultra-broadband spin inversion. *Phys. Lett.*, 120:201, 1985.
- [30] M. H. Levitt. Composite pulses. *Prog. Nucl. Magn. Reson. Spectrosc.*, 18:61122, 1986.
- [31] Ě. Kupĉe and R. Freeman. Adiabatic pulses for wideband inversion and broadband decoupling. *J. Magn. Reson. Ser. A*, 115:273–276, 1995.
- [32] Ě. Kupĉe and R. Freeman. Optimized adiabatic pulses for wideband spin inversion. *J. Magn. Reson. Ser. A*, 118:299–303, 1996.
- [33] A. Tannus and M. Garwood. Improved performance of frequency-swept pulses using offset-independent adiabaticity. *J. Magn. Reson. Ser. A*, 120:133–137, 1996.
- [34] T. Hwang, P. van Zijl, and M. Garwood. Fast broadband inversion by adiabatic pulses. *J. Magn. Reson.*, 133:200–203, 1998.
- [35] M. A. Smith, H. Hu, and A. J. Shaka. Improved broadband inversion performance for NMR in liquids. *J. Magn. Reson.*, 151:269–283, 2001.
- [36] K. Kobzar, T. E. Skinner, N. Khaneja, S. J. Glaser, and B. Luy. Exploring the Limits of Broadband Excitation and Inversion Pulses. *J. Magn. Reson.*, 170:236–243, 2004.
- [37] K. Kobzar, T. E. Skinner, N. Khaneja, S. J. Glaser, and B. Luy. Exploring the limits of broadband excitation and inversion: II. Rf-power optimized pulses. *J. Magn. Reson.*, 194:58–66, 2008.
- [38] M. H. Levitt and R. Freeman. Compensation for pulse imperfections in NMR spin-echo experiments. *J. Magn. Reson.*, 43:65–80, 1980.
- [39] S. Conolly, G. Glover, D. Nishimura, and A. Macovski. A reduced power selective adiabatic spin-echo pulse sequence. *Magn. Reson. Med.*, 18:28–38, 1991.
- [40] T. L. Hwang, P. C. M. Van Zij, and M. Garwood. Broadband Adiabatic Refocusing without Phase Distortion. *J. Magn. Reson.*, 124:250–254, 1997.
- [41] B. Luy, K. Kobzar, T. E. Skinner, N. Khaneja, and S. J. Glaser. Construction of Universal Rotations from Point to Point Transformations. *J. Magn. Reson.*, 176:179–186, 2005.
- [42] A. J. Shaka and A. J. Pines. Symmetric phase-alternating composite pulses. *J. Magn. Reson.*, 71:495503, 1987.
- [43] S. Conolly, D. Nishimura, and A. Macovski. Optimal control solutions to the magnetic resonance selective excitation problem. *IEEE Trans. Med. Imaging*, MI-5:106, 1986.
- [44] J. Mao, T. H. Mareci, K. N. Scott, and E. R. Andrew. Selective inversion radiofrequency pulses by optimal control. *J. Magn. Reson.*, 70:310318, 1986.
- [45] V. Smith, J. Kurhanewicz, and T. L. James. Solvent-suppression pulses. I. Design using optimal control theory. *J. Magn. Reson.*, 95:4160, 1991.

- [46] V. Smith, J. Kurhanewicz, and T. L. James. Solvent-suppression pulses. II. In vitro and in vivo testing of optimal-control-theory pulses. *J. Magn. Reson.*, 95:6170, 1991.
- [47] D. Rosenfeld and Y. Zur. Design of adiabatic selective pulses using optimal control theory. *Magn. Reson. Med.*, 36:401409, 1996.
- [48] T. E. Skinner, T. O. Reiss, B. Luy, N. Khaneja, and S. J. Glaser. Application of Optimal Control Theory to the Design of Broadband Excitation Pulses for High Resolution NMR. *J. Magn. Reson.*, 163:8, 2003.
- [49] T. E. Skinner, T. O. Reiss, B. Luy, N. Khaneja, and S. J. Glaser. Reducing the Duration of Broadband Excitation Pulses Using Optimal Control with Limited RF Amplitude. *J. Magn. Reson.*, 167:68–74, 2004.
- [50] T. E. Skinner, T. O. Reiss, B. Luy, N. Khaneja, and S. J. Glaser. Tailoring the optimal control cost function to a desired output: application to minimizing phase errors in short broadband excitation pulses. *J. Magn. Reson.*, 172:17–23, 2005.
- [51] T. E. Skinner, K. Kobzar, B. Luy, R. Bendall, W. Bermel, N. Khaneja, and S. J. Glaser. Optimal Control Design of Constant Amplitude Phase-Modulated Pulses: Application to Calibration-Free Broadband Excitation. *J. Magn. Reson.*, 179:241, 2006.
- [52] N. I. Gershenson, K. Kobzar, B. Luy, S. J. Glaser, and T. E. Skinner. Optimal Control Design of Excitation Pulses that Accomodate Relaxation. *J. Magn. Reson.*, 188:330, 2007.
- [53] N. I. Gershenson, T. E. Skinner, B. Brutscher, N. Khaneja, M. Nimbalkar, B. Luy, and S. J. Glaser. Linear Phase Slope in Pulse Design: Application to Coherence Transfer. *J. Magn. Reson.*, 192:235, 2008.
- [54] N. I. Gershenson, D. F. Miller, and T. E. Skinner. The design of excitation pulses for spin systems using optimal control theory: With application to NMR spectroscopy. *Optim. Control Appl. Meth.*, 30:463475, 2009.
- [55] N. I. Gershenson and T. E. Skinner. Optimal control design of pulse shapes as analytic functions. *J. Magn. Reson.*, 204:248255, 2010.
- [56] T. E. Skinner, M. Braun, K. Woelk, N. I. Gershenson, and S. J. Glaser. Design and Application of Robust RF Pulses for Toroid Cavity NMR Spectroscopy. *J. Magn. Reson.*, 209:282–290, 2011.
- [57] N. Khaneja, T. Reiss, C. Kehlet, T. Schulte-Herbrüggen, and S. J. Glaser. Optimal Control of Coupled Spin Dynamics: Design of NMR Pulse Sequences by Gradient Ascent Algorithms. *J. Magn. Reson.*, 172:296–305, 2005.
- [58] K. Kobzar. PhD thesis, Technische Universität München, 2007.
- [59] T. W. Borneman, M. D. Hürlimann, and D. G. Cory. Application of optimal control to CPMG refocusing pulse design. *J. Magn. Reson.*, 207:220233, 2010.
- [60] C. Rangan and P. H. Bucksbaum. Optimally shaped terahertz pulses for phase retrieval in a Rydberg-atom data register. *Phys. Rev. A*, 64:033417–5, 2001.

- [61] J. P. Palao and R. Kosloff. Quantum computing by an optimal control algorithm for unitary transformations. *Phys. Rev. Lett.*, 89:188301–4, 2002.
- [62] T. Schulte-Herbrüggen, A. Spörl, and S. J. Glaser N. Khaneja. Optimal control-based efficient synthesis of building blocks of quantum algorithms seen in perspective from network complexity towards time complexity. *Phys. Rev. A*, 72:042331–7, 2005.
- [63] R. P. Feynman, Jr. F. L. Vernon, and R. W. Hellwarth. Geometrical representation of the Schrödinger equation for solving maser problems. *J. Appl. Phys.*, 28:49–52, 1957.
- [64] J. M. Boehlen and G. Bodenhausen. Experimental aspects of chirp NMR spectroscopy. *J. Magn. Reson. Series A*, 102:293301, 1993.
- [65] Thomas E. Skinner, Naum I. Gershenson, Manoj Nimbalkar, and Steffen J. Glaser. Optimal control design of band-selective excitation pulses that accommodate relaxation and RF inhomogeneity. *J. Magn. Reson.*, submitted, 2011.
- [66] Barrett L. Tomlinson and H. D. W. Hill. Fourier synthesized excitation of nuclear magnetic resonance with application to homonuclear decoupling and solvent line suppression. *J. Chem. Phys.*, 59:17751785, 1973.
- [67] Geoffrey Bodenhausen, Ray Freeman, and Gareth A. Morris. A simple pulse sequence for selective excitation in Fourier transform NMR. *J. Magn. Reson.*, 23:171175, 1976.
- [68] G. A. Morris and R. Freeman. Selective excitation in Fourier transform nuclear magnetic resonance. *J. Magn. Reson.*, 29:433, 1978.
- [69] D. I. Hoult. The solution of the Bloch equations in the presence of a varying B1 field: An approach to selective pulse analysis. *J. Magn. Reson.*, 35:68–86, 1979.
- [70] Lyndon Emsley and Geoffrey Bodenhausen. Self-refocusing effect of 270° Gaussian pulses. Applications to selective two-dimensional exchange spectroscopy. *J. Magn. Reson.*, 82:211–221, 1989.
- [71] P. Caravatti, G. Bodenhausen, and R. R. Ernst. Selective pulse experiments in high-resolution solid state NMR. *J. Magn. Reson.*, 55:88–103, 1983.
- [72] Christopher Bauer, Ray Freeman, Tom Frenkiel, James Keeler, and A. J. Shaka. Gaussian pulses. *J. Magn. Reson.*, 58:442, 1984.
- [73] D. I. Hoult M. S. Silver, R. I. Joseph. Highly selective $\pi/2$ and π pulse generation. *J. Magn. Reson.*, 59:347–351, 1984.
- [74] Jan Friedrich, Simon Davies, and Ray Freeman. Shaped selective pulses for coherence-transfer experiments. *J. Magn. Reson.*, 75:390–395, 1987.
- [75] C. J. Hardy, P. A. Bottomley, M. O'Donnell, and P. Roemer. Optimization of two dimensional spatially selective NMR pulses by simulated annealing. *J. Magn. Reson.*, 77:223–259, 1988.
- [76] F. Loaiza, M. A. McCoy, S. L. Hammes, and W. S. Warren. Selective excitation without phase distortion using self-refocused amplitude- and amplitude/phase-modulated pulses. *J. Magn. Reson.*, 77:175–181, 1988.

- [77] Piotr Tekely, Jean Brondeau, Karim Elbayed, Alain Retournard, and Daniel Canet. A simple pulse train, using 90 hard pulses, for selective excitation in high-resolution solid-state NMR. *J. Magn. Reson.*, 80:509–516, 1988.
- [78] X.-L. Wu and R. Freeman. Darwin’s ideas applied to magnetic resonance. The marriage broker. *J. Magn. Reson.*, 85:414–420, 1989.
- [79] H. Geen, S. Wimperis, and R. Freeman. Band-selective pulses without phase distortion. A simulated annealing approach. *J. Magn. Reson.*, 85:620–627, 1989.
- [80] L. Emsley and G. Bodenhausen. Self-refocusing 270° gaussian pulses for slice selection without gradient reversal in magnetic resonance imaging. *Magn. Reson. Med.*, 10:273–281, 1989.
- [81] A. E. Yagle. Inversion of the Bloch transform in magnetic resonance imaging using asymmetric two-component inverse scattering. *Inverse Problem*, 6:133–151, 1990.
- [82] M. Shinnar, L. Bolinger, and J. S. Leigh. The synthesis of pulse sequences yielding arbitrary magnetization vectors. *Mag. Reson. Med.*, 12:74–80, 1989.
- [83] M. Shinnar, L. Bolinger, and J. S. Leigh. The use of finite impulse response filters in pulse design. *Mag. Reson. Med.*, 12:81–87, 1989.
- [84] M. Shinnar, L. Bolinger, and J. S. Leigh. The synthesis of pulse sequences yielding arbitrary magnetization vectors. *Mag. Reson. Med.*, 12:88–92, 1989.
- [85] M. Shinnar, L. Bolinger, and J. S. Leigh. The application of spinors to pulse synthesis and analysis. *Mag. Reson. Med.*, 12:93–98, 1989.
- [86] J. W. Carlson. Exact solution for selective-excitation pulses. *Mag. Reson. Med.*, 94:376–386, 1991.
- [87] H. Geen and R. Freeman. Band-selective radiofrequency pulses. *J. Magn. Reson.*, 93:93–141, 1991.
- [88] R. Freeman. Selective excitation in high-resolution NMR. *Chem. Rev.*, 91-7:1397–1412, 1991.
- [89] R. Freeman. High resolution NMR using selective excitation. *J. Mol. Struct.*, 266:39–51, 1992.
- [90] J. W. Carlson. Exact solution for selective-excitation pulses. II Excitation pulses with phase control. *J. Magn. Reson.*, 97:65, 1992.
- [91] D. E. Rourke and P. G. Morris. The inverse scattering and its use in the exact inversion of the Bloch equation for noninteracting spins. *J. Magn. Reson.*, 99:118, 1992.
- [92] L. Emsley and G. Bodenhausen. Optimization of shaped selective pulses for NMR using a quaternion description of their overall propagators. *J. Magn. Reson.*, 97:135–148, 1992.
- [93] Ě. Kupĉe and R. Freeman. Polychromatic selective pulses. *J. Magn. Reson. Ser. A*, 102:122, 1993.

- [94] D. E. Rourke, M.J.W. Prior, P. G. Morris, and J. A. B. Lohman. Stereographic projection method of exactly calculating selective pulses. *J. Magn. Reson. Ser. A*, 107:203, 1994.
- [95] L. Emsley. Selective pulses and their applications to assignment and structure determination in nuclear magnetic resonance. *Methods Enzymol.*, 239:207–248, 1992.
- [96] Ě. Kupĉe and R. Freeman. Band-Selective Correlation Spectroscopy. *J. Magn. Reson. Ser. A*, 112:134–137, 1995.
- [97] Ě. Kupĉe, J. Boyd, and I.D. Campbell. Short selective pulses for biochemical applications. *J. Magn. Reson. Ser. A*, 106:300–303, 1995.
- [98] S. Caldarelli, A. Lesage, and L. Emsley. Pure-phase selective excitation in NMR by acquisition during the pulse. *J. Magn. Reson. Ser. A*, 116:129–132, 1995.
- [99] C. Dalvit, S. Y. Ko, and J.-M. Böhlen. Single and multiple-selective excitation combined with pulsed field gradients. *J. Magn. Reson. Ser. B*, 10:124–132, 1996.
- [100] P. Borgnat, A. Lesage, S. Caldarelli, and L. Emsley. Narrowband linear selective pulses for NMR. *J. Magn. Reson. Ser. A*, 119:289–294, 1996.
- [101] E. Lunati, P. Cofrancesco, M. Villa, P. Marzola, and F. Osculati. Evolution Strategy Optimization for Selective Pulses in NMR. *J. Magn. Reson.*, 134:223–235, 1998.
- [102] A. Virgili T. Parella, F. Snchez-Ferrando. A simple approach for ultraclean multi-site selective excitation using excitation sculpting. *J. Magn. Reson.*, 135:50–53, 1998.
- [103] Ray Freeman. Shaped radiofrequency pulses in high resolution NMR. *Prog. Nucl. Magn. Reson. Spectrosc.*, 32:59–106, 1998.
- [104] P. Xu, X.-L. Wu, and R. Freeman. User-friendly selective pulses. *J. Magn. Reson.*, 99:308–322, 1992.
- [105] M. A. McCoy and L. Mueller. Nonresonant effects of frequency-selective pulses. *J. Magn. Reson.*, 99:18–36, 1992.
- [106] C. Roumestand, C. Delay, J. A. Gavid, and D. Canet. A practical approach to the implementation of selectivity in homonuclear multidimensional NMR with frequency selective-filtering techniques. Application to the chemical structure elucidation of complex oligosaccharides. *Magn. Reson. Chem.*, 37:451–478, 1999.
- [107] C. Roumestand and D. Canet. Extending the excitation sculpting concept for selective excitation. *J. Magn. Reson.*, 147:331–339, 2000.
- [108] K. Zangger, M. Oberer, and H. Sterk. Pure-phase selective excitation in fast-relaxing systems. *J. Magn. Reson.*, 152:48–56, 2001.
- [109] P. Charmont, D. Sakellariou, and L. Emsley. Sample restriction using radiofrequency field selective pulses in high-resolution solid-state NMR. *J. Magn. Reson.*, 154:136–141, 2002.

- [110] K. E. Cano, M. A. Smith, and A. J. Shaka. Adjustable, broadband, selective excitation with uniform phase. *J. Magn. Reson.*, 155:131–139, 2002.
- [111] M. Veshtort and R. Griffin. High-performance selective excitation pulses for solid- and liquid-state NMR spectroscopy. *Chem. Phys. Chem.*, 5:834–850, 2004.
- [112] P. J. Hajduk, D. A. Horita, and L. E. Lerner. Theoretical analysis of relaxation during shaped pulses. The effects of short T_1 and T_2 . *J. Magn. Reson. Ser. A*, 103:40–52, 1993.
- [113] A. Raddi and U. Klose. Relaxation effects on transverse magnetization using RF pulses long compared to T_2 . *J. Magn. Reson.*, 144:108–114, 2008.
- [114] J.-M. Nuzillard and R. Freeman. Band-selective pulse designed to accommodate relaxation. *J. Magn. Reson. Ser. A*, 107:113–118, 1994.
- [115] J. Shen and L. E. Lerner. Selective radiofrequency pulses minimizing relaxation. *J. Magn. Reson. Ser. A*, 112:265–269, 1995.
- [116] D. E. Rourke, L. Khodarinova, and A. A. Karabanov. Two-Level Systems with Relaxation. *Phys. Rev. Letters*, 92:163003–4, 2004.
- [117] D. E. Rourke, A. A. Karabanov, G. H. Booth, and I. Frantsuzov. The Bloch equation when $T_1 = T_2$. *Inverse Problems*, 23:609–623, 2007.
- [118] B. Issa. Design of self-refocused pulses under short relaxation times. *J. Magn. Reson.*, 198:151–159, 2009.
- [119] Navin Khaneja, Roger Brockett, and Steffen J. Glaser. Time optimal control in spin systems. *Phys. Rev. A*, 63(3):032308, 2001.
- [120] Timo O. Reiss, Navin Khaneja, and Steffen J. Glaser. Time-optimal coherence-order-selective transfer of in-phase coherence in heteronuclear spin systems. *J. Magn. Reson.*, 154(2):192–195, 2002.
- [121] N. Khaneja, T. Reiss, B. Luy, and S. J. Glaser. Optimal Control of Spin Dynamics in the Presence of Relaxation. *J. Magn. Reson.*, 162:311–319, 2003.
- [122] K. Kobzar, T. E. Skinner, N. Khaneja, S. J. Glaser, and B. Luy. Exploring the Limits of Broadband Excitation and Inversion Pulses. *J. Magn. Reson.*, 170:236–243, 2004.
- [123] K. Kobzar, B. Luy, N. Khaneja, and S. J. Glaser. Pattern Pulses: Design of Arbitrary Excitation Profiles as a Function of Pulse Amplitude and Offset. *J. Magn. Reson.*, 173:229–235, 2005.
- [124] J. L. Neves, B. Heitmann, T. O. Reiss, H. H. R. Schor, N. Khaneja, and S. J. Glaser. Exploring the Limits of Polarization Transfer Efficiency in Homonuclear Three Spin Systems. *J. Magn. Reson.*, 181:126–134, 2006.
- [125] K. Kobzar, T. E. Skinner, N. Khaneja, S. J. Glaser, and B. Luy. Exploring the limits of broadband excitation and inversion: II. Rf-power optimized pulses. *J. Magn. Reson.*, 194:58–66, 2008.
- [126] J. L. Neves, B. Heitmann, N. Khaneja, and S. J. Glaser. Heteronuclear decoupling by optimal tracking. *J. Magn. Reson.*, 201:7–17, 2009.

- [127] M. Braun and S. J. Glaser. Cooperative Pulses. *J. Magn. Reson.*, 207:114–123, 2010.
- [128] N. Pomplun and S. J. Glaser. Exploring the Limits of Electron-Nuclear Polarization Transfer Efficiency in Three-Spin Systems. *Phys. Chem. Chem. Phys.*, 12:5791–5798, 2010.
- [129] Y. Zhang, M. Lapert, D. Sugny, M. Braun, and S. J. Glaser. Time-Optimal Control of Spin 1/2 Particles in the Presence of Radiation Damping and Relaxation. *J. Chem. Phys.*, 134:054103, 2011.
- [130] T. E. Skinner, N. I. Gershenson, B. Luy, and S. J. Glaser. Optimal control of band-selective excitation pulses to accommodate relaxation, 48th Experimental NMR Conference (ENC) Daytona Beach, Florida, April, 2007.
- [131] N. I. Gershenson and S. J. Glaser and T. E. Skinner. Empirical relations for the design of band-selective pulses using optimal control theory, 48th Experimental NMR Conference (ENC) Daytona Beach, Florida, April, 2007.
- [132] D. J. Lurie. A systematic design procedure for selective pulses in NMR imaging. *Magn. Reson. Imaging*, 3:235–243, 1985.
- [133] M. O'Donnell and W. J. Adams. Selective time-reversal pulses for NMR imaging. *Magn. Reson. Imaging*, 3:377–382, 1985.
- [134] J. B. Murdoch, A. H. Lent, and M. R. Kritzer. Computer-optimized narrowband pulses for multi-slice imaging. *J. Magn. Reson.*, 74:226–263, 1987.
- [135] D. Rosenfeld and S. L. Panfil and Y. Zur. Optimization of adiabatic selective pulses. *J. Magn. Reson.*, 126:221–228, 1997.
- [136] J. Pauly, P. Le Roux, D. Nishimur, and A. Macovski. Parameter relations for the Shinnar-Le Roux selective excitation pulse design algorithm. *IEEE Trans. Med. Imaging*, 10:53, 1991.
- [137] A. Hennig R. F. Schulte, J. Tsao, P. Boesiger, and K.P.Pruessmann. Design of broadband RF pulses with polynomial-phase response. *J. Magn. Reson.*, 186:167–175, 2007.
- [138] R. F. Schulte, P. Le Roux, M. W. Vogel, and H. Koenig. Design of phase-modulated broadband refocusing pulses. *J. Magn. Reson.*, 190:271–279, 2008.
- [139] T. W. Parks and C. S. Burrus. *Digital Filter Design*. John Wiley and Sons, New York, 1987.
- [140] Manoj Nimbalkar, Robert Zeier, Jorge Neves, S. Begam Elavarasi, Kavita Dorai, Haidong Yuan, Navin Khaneja, and Steffen J. Glaser. Multiple-spin coherence transfer in linear Ising spin chains and beyond: numerically-optimized pulses and experiments. *Phys. Rev. A*, in press, 2011.
- [141] E. Lieb, T. Schultz, and D. Mattis. Two Soluble Models of an Antiferromagnetic Chain. *Ann. Phys.*, 18:407–466, 1961.
- [142] H. M. Pastawski, G. Usaj, and P. R. Levstein. Quantum Interference Phenomena in the Local Polarization Dynamics of Mesoscopic Systems: an NMR Observation. *Chem. Phys. Lett.*, 261:329–334, 1996.

- [143] S. J. Glaser and G. P. Drobny. Controlled Coherence Transfer by a Multiple-Step Tailored TOCSY Experiment. *Chem. Phys. Lett.*, 181:553–559, 1991.
- [144] J. Listerud, S. J. Glaser, and G. P. Drobny. Symmetry and Isotropic Coherence Transfer. II. Three Spin Calculations Using a Young Tableaux Formulation. *Mol. Phys.*, 78:629–658, 1993.
- [145] S. J. Glaser. Coupling Topology Dependence of Polarization-Transfer Efficiency in TOCSY and TACSU Experiments. *J. Magn. Reson. A*, 104:283–301, 1993.
- [146] S. J. Glaser and J. J. Quant. Homonuclear and Heteronuclear Hartman-Hahn Transfer in Isotropic Liquids. In W. S. Warren, editor, *Advances in Magnetic and Optical Resonance*, volume 19, pages 59–252. Academic Press, San Diego, 1996.
- [147] R. M. White. *Quantum Theory of Magnetism*. Springer, Berlin, 1983.
- [148] D. C. Mattis. *The Theory of Magnetism I, Statistics and Dynamics*. Springer, Berlin, 1988.
- [149] Z. L. Mádi, B. Brutscher, T. Schulte-Herbrüggen, R. Brüschweiler, and R. R. Ernst. Time-resolved Observation of Spin Waves in a Linear Chain of Nuclear Spins. *Chem. Phys. Lett.*, 268:300–305, 1997.
- [150] N. Khaneja and S. J. Glaser. Efficient Transfer of Coherence through Ising Spin Chains. *Phys. Rev. A*, 66:060301(R), 2002.
- [151] Haidong Yuan, Steffen J. Glaser, and Navin Khaneja. Geodesics for efficient creation and propagation of order along ising spin chains. *Phys. Rev. A*, 76(6):012316, 2007.
- [152] H. Yuan, R. Zeier, and N. Khaneja. Elliptic Functions and Efficient Control of Ising Spin Chains with Unequal Couplings. *Phys. Rev. A*, 77:032340, 2008.
- [153] F. Yamaguchi and Y. Yamamoto. Crystal Lattice Quantum Computer. *Appl. Phys. A*, 68:1–8, 1999.
- [154] S. G. Schirmer and P. J. Pemberton-Ross. Fast High-Fidelity Information Transmission through Spin-Chain Quantum Wires. *Phys. Rev. A*, 80:030301(R), 2009.
- [155] M. L. Remerowski, S. J. Glaser, and G. P. Drobny. A Theoretical Study of Coherence Transfer by Isotropic Mixing: Calculation of Pulse Sequence Performance for Systems of Biological Interest. *Mol. Phys.*, 68:1191–1218, 1989.
- [156] H. L. Eaton, S. W. Fesik, S. J. Glaser, and G. P. Drobny. Time Dependence of ^{13}C - ^{13}C Magnetization Transfer in Isotropic Mixing Experiments Involving Amino Acid Spin Systems. *J. Magn. Reson.*, 90:452–463, 1990.
- [157] J. Cavanagh, W. J. Fairbrother, A. G. Palmer, and N. J. Skelton. *Protein NMR Spectroscopy: Principles and Practice*. Academic Press, San Diego, 1996.
- [158] Richard R. Ernst, Geoffrey Bodenhausen, and Alexander Wokaun. *Principles of Nuclear Magnetic Resonance in One and Two Dimensions*. Clarendon Press, Oxford, 1997. reprinted with corrections.
- [159] S. J. Archer, M. Ikura, D. A. Torchia, and A. Bax. An Alternative 3D NMR Technique for Correlating Backbone ^{15}N with Side Chain H_β Resonances in Larger Proteins. *J. Magn. Reson.*, 95:636–641, 1991.

- [160] M. Sattler, J. Schleucher, and C. Griesinger. Heteronuclear multidimensional NMR experiments for the structure determination of proteins in solution employing pulsed field gradients. *Prog. NMR Spec.*, 34:93–158, 1999.
- [161] M. H. Levitt and R. R. Ernst. Multiple-quantum Excitation and Spin Topology Filtration in High-resolution NMR. *J. Chem. Phys.*, 83:3297–3310, 1985.
- [162] E. Ising. Beitrag zur theorie des ferromagnetismus. *Z. Physik*, 31:253–258, 1925.
- [163] Willem J. Caspers. *Spin systems*. World Scientific, Singapore, 1989.
- [164] G. A. Morris and R. Freeman. Enhancement of Nuclear Magnetic Resonance Signals by Polarization Transfer. *J. Am. Chem. Soc.*, 101:760–762, 1979.
- [165] Navin Khaneja, Roger Brockett, and Steffen J. Glaser. Time optimal control in spin systems. *Phys. Rev. A*, 63(3):032308, 2001.
- [166] Timo O. Reiss, Navin Khaneja, and Steffen J. Glaser. Time-optimal coherence-order-selective transfer of in-phase coherence in heteronuclear is spin systems. *J. Magn. Reson.*, 154(2):192–195, 2002.
- [167] Navin Khaneja, Steffen J. Glaser, and Roger Brockett. Sub-riemannian geometry and time optimal control of three spin systems: quantum gates and coherence transfer. *Phys. Rev. A*, 65(3):032301, 2002.
- [168] Navin Khaneja, Frank Kramer, and Steffen J. Glaser. Optimal experiments for maximizing coherence transfer between coupled spins. *J. Magn. Reson.*, 173(1):116–124, 2005.
- [169] Navin Khaneja, Björn Heitmann, Andreas Spörl, Haidong Yuan, Thomas Schulte-Herbrüggen, and Steffen J. Glaser. Shortest paths for efficient control of indirectly coupled qubits. *Phys. Rev. A*, 75(1):012322, 2007.
- [170] R. Fisher, H. Yuan, A. Spörl, and S. Glaser. Time-Optimal Generation of Cluster States. *Phys. Rev. A*, 79:042304, 2009.
- [171] E. Assémat, M. Lapert, Y. Zhang, M. Braun, S. J. Glaser, and D. Sugny. Simultaneous Time-Optimal Control of the Inversion of Two Spin 1/2 Particles. *Phys. Rev. A*, 82:013415, 2010.
- [172] N. Khaneja, T. Reiss, B. Luy, and S. J. Glaser. Optimal Control of Spin Dynamics in the Presence of Relaxation. *J. Magn. Reson.*, 162:311–319, 2003.
- [173] N. Khaneja, B. Luy, and S. J. Glaser. Boundary of Quantum Evolution under Decoherence. *Proc. Natl. Acad. Sci. USA*, 100:13162–13166, 2003.
- [174] D. Stefanatos, N. Khaneja, and S. J. Glaser. Optimal Control of Coupled Spins in Presence of Longitudinal and Transverse Relaxation. *Phys. Rev. A*, 69:022319, 2004.
- [175] D. P. Fröh, T. Ito, Jr-Shin Li, G. Wagner, S. J. Glaser, and N. Khaneja. Sensitivity Enhancement in NMR of Macromolecules by Application of Optimal Control Theory. *J. Biomol. NMR*, 32:23–30, 2005.
- [176] D. Stefanatos, N. Khaneja, and S. J. Glaser. Relaxation Optimized Transfer of Spin Order in Ising Chains. *Phys. Rev. A*, 72:062320, 2005.

- [177] M. Lapert, Y. Zhang, M. Braun, S. J. Glaser, and D. Sugny. Singular Extremals for the Time-Optimal Control of Dissipative Spin 1/2 Particles. *Phys. Rev. Lett.*, 104:083001, 2010.
- [178] N. C. Nielsen, C. Kehlet, S. J. Glaser, and N. Khaneja. Optimal Control Methods in NMR Spectroscopy. *Encyclopedia of Nuclear Magnetic Resonance*, 9:100, 2010.
- [179] T. E. Skinner, T. O. Reiss, B. Luy, N. Khaneja, and S. J. Glaser. Application of Optimal Control Theory to the Design of Broadband Excitation Pulses for High Resolution NMR. *J. Magn. Reson.*, 163:8, 2003.
- [180] K. Kobzar, B. Luy, N. Khaneja, and S.J. Glaser. Pattern Pulses: Design of Arbitrary Excitation Profiles as a Function of Pulse Amplitude and Offset. *J. Magn. Reson.*, 173:229–235, 2005.
- [181] K. Kobzar, T. E. Skinner, N. Khaneja, S. J. Glaser, and B. Luy. Exploring the Limits of Excitation and Inversion Pulses II: RF-Power Optimized Pulses. *J. Magn. Reson.*, 194:58, 2008.
- [182] N. I. Gershenzon, T. E. Skinner, B. Brutscher, N. Khaneja, M. Nimbalkar, B. Luy, and S. J. Glaser. Linear Phase Slope in Pulse Design: Application to Coherence Transfer. *J. Magn. Reson.*, 192:235, 2008.
- [183] N. Khaneja, T. Reiss, C. Kehlet, T. Schulte-Herbrüggen, and S. J. Glaser. Optimal Control of Coupled Spin Dynamics: Design of NMR Pulse Sequences by Gradient Ascent Algorithms. *J. Magn. Reson.*, 172:296–305, 2005.
- [184] Z. Tošner, T. Vosegaard, C. T. Kehlet, N. Khaneja, S. J. Glaser, and N. C. Nielsen. Optimal Control in NMR Spectroscopy: Numerical Implementation in SIMPSON. *J. Magn. Reson.*, 197:120–134, 2009.
- [185] S. Machnes, U. Sander, S. J. Glaser, P. de Fouquières, A. Gruslys, S. Schirmer, and T. Schulte-Herbrüggen. Comparing, Optimising and Benchmarking Quantum Control Algorithms in a Unifying Programming Framework. *Phys. Rev. A*, 84:022305, 2011.
- [186] P. de Fouquieres, S. G. Schirmer, S. J. Glaser, and I. Kuprov. Second Order Gradient Ascent Pulse Engineering. *J. Magn. Reson.*, 212:241–247, 2011.
- [187] A. N. Pechen and D. J. Tannor. Are there Traps in Quantum Control Landscapes? *Phys. Rev. Lett.*, 106:120402, 2011.
- [188] M. Lapert, Y. Zhang, M. Braun, S. J. Glaser, and D. Sugny. Geometric Versus Numerical Optimal Control of a Dissipative Spin 1/2 Particle. *Phys. Rev. A*, 82:063418, 2010.
- [189] K. Kobzar, T. E. Skinner, N. Khaneja, S. J. Glaser, and B. Luy. Exploring the Limits of Broadband Excitation and Inversion Pulses. *J. Magn. Reson.*, 170:236–243, 2004.
- [190] J. L. Neves, B. Heitmann, T. O. Reiss, H. H. R. Schor, N. Khaneja, and S. J. Glaser. Exploring the Limits of Polarization Transfer Efficiency in Homonuclear Three Spin Systems. *J. Magn. Reson.*, 181:126–134, 2006.

- [191] Nikolas Pomplun, Björn Heitmann, Navin Khaneja, and Steffen Glaser. Optimization of electron-nuclear polarization transfer. *Appl. Magn. Reson.*, 34:331–346, 2008.
- [192] N. Pomplun and S. J. Glaser. Exploring the Limits of Electron-Nuclear Polarization Transfer Efficiency in Three-Spin Systems. *Phys. Chem. Chem. Phys.*, 12:5791–5798, 2010.
- [193] N. I. Gershenzon, K. Kobzar, B. Luy, S. J. Glaser, and T. E. Skinner. Optimal Control Design of Excitation Pulses that Accomodate Relaxation. *J. Magn. Reson.*, 188:330, 2007.
- [194] M. Lapert, Y. Zhang, S. J. Glaser, and D. Sugny. Towards the Time-Optimal Control of Dissipative Spin 1/2 Particles in Nuclear Magnetic Resonance. *J. Phys. B*, 44:154014, 2011.
- [195] Y. Zhang, M. Lapert, D. Sugny, M. Braun, and S. J. Glaser. Time-Optimal Control of Spin 1/2 Particles in the Presence of Radiation Damping and Relaxation. *J. Chem. Phys.*, 134:054103, 2011.
- [196] T. E. Skinner, T. O. Reiss, B. Luy, N. Khaneja, and S. J. Glaser. Reducing the Duration of Broadband Excitation Pulses Using Optimal Control with Limited RF Amplitude. *J. Magn. Reson.*, 167:68–74, 2004.
- [197] T. E. Skinner, K. Kobzar, B. Luy, R. Bendall, W. Bermel, N. Khaneja, and S. J. Glaser. Optimal Control Design of Constant Amplitude Phase-Modulated Pulses: Application to Calibration-Free Broadband Excitation. *J. Magn. Reson.*, 179:241, 2006.
- [198] T. E. Skinner, M. Braun, K. Woelk, N. I. Gershenzon, and S. J. Glaser. Design and Application of Robust RF Pulses for Toroid Cavity NMR Spectroscopy. *J. Magn. Reson.*, 209:282–290, 2011.
- [199] G. A. Morris and R. Freeman. Selective excitation in Fourier transform nuclear magnetic resonance. *J. Magn. Reson.*, 29:433, 1978.
- [200] N. Khaneja, J.-S. Li, C. Kehlet, B. Luy, and S. J. Glaser. Broadband relaxation-optimized polarization transfer in magnetic resonance. *Proc. Natl. Acad. Sci. USA*, 101:14742, 2004.
- [201] Nikolas Pomplun. PhD thesis, Technische Universität München, 2010.
- [202] R. Marx, N. Pomplun, W. Bermel, H. Zeiger, F. Engelke, A. F. Fahmy, and S. J. Glaser. Engineering of an all-heteronuclear 5-qubit NMR quantum computer. in preparation, 2011.
- [203] D. Canet, J. Brondeau, and C. Roumestand. Analytical Expressions for the DANTE Pulse Sequence. *J. Magn. Reson. A*, 117:103, 1995.
- [204] M. H. Levitt, R. Freeman, and T. Frenkiel. Broadband heteronuclear decoupling. *J. Magn. Reson.*, 47:328–330, 1982.
- [205] R. Freeman, S. P. Kempell, and M. H. Levitt. Radiofrequency pulse sequences which compensate their own imperfections. *J. Magn. Reson.*, 38:453–479, 1980.

- [206] M. H. Levitt. Symmetrical composite pulse sequences for NMR population inversion. I. Compensation of radiofrequency field inhomogeneity. *J. Magn. Reson.*, 48:234264, 1982.
- [207] M. H. Levitta and R. R. Ernst. Composite pulses constructed by a recursive expansion procedure. *J. Magn. Reson.*, 55:247254, 1983.
- [208] R. Tycko, H.M. Cho, E. Schneider, and A. Pines. Composite pulses without phase distortion. *J. Magn. Reson.*, 61:9091, 1985.
- [209] M. H. Levitt. Composite pulses. *Prog. Nucl. Magn. Reson. Spectrosc.*, 18:61122, 1986.
- [210] A. J. Shaka and A. J. Pines. Symmetric phase-alternating composite pulses. *J. Magn. Reson.*, 71:495503, 1987.
- [211] J. M. Boehlen, M. Rey, and G. Bodenhausen. Refocusing with chirped pulses for broadband excitation without phase dispersion. *J. Magn. Reson.*, 84:191197, 1989.
- [212] J. M. Boehlen and G. Bodenhausen. Experimental aspects of chirp NMR spectroscopy. *J. Magn. Reson. Series A*, 102:293301, 1993.
- [213] D. Abramovich and S. Vega. Derivation of broadband and narrowband excitation pulses using the Floquet Formalism. *J. Magn. Reson. Series A*, 105:30–48, 1993.
- [214] Ě. Kupĉe and R. Freeman. Wideband excitation with polychromatic pulses. *J. Magn. Reson. Series A*, 108:268–273, 1994.
- [215] K. Hallenga and G. M. Lippens. A constant-time ^{13}C - ^1H HSQC with uniform excitation over the complete ^{13}C chemical shift range. *J. Biomol. NMR*, 5:59–66, 1995.
- [216] T. L. Hwang, P. C. M. van Zijl, and M. Garwood. Broadband adiabatic refocusing without phase distortion. *J. Magn. Reson.*, 124:250–254, 1997.
- [217] K. E. Cano, M. A. Smith, and A. J. Shaka. Adjustable, broadband, selective excitation with uniform phase. *J. Magn. Reson.*, 155:131–139, 2002.
- [218] B. Luy, K. Kobzar, T. E. Skinner, N. Khaneja, and S. J. Glaser. Construction of Universal Rotations from Point to Point Transformations. *J. Magn. Reson.*, 176:179–186, 2005.
- [219] Klaus-Daniel Umland, Adeline Palisse, Timm T. Haug, and Stefan F. Kirsch. Domino Reactions Consisting of Heterocyclization and 1,2-MigrationRedox-Neutral and Oxidative Transition-Metal Catalysis. *Angew. Chem. Int. Ed.*, 50:1–5, 2011.
- [220] Arthur G. Palmer III, John Cavanagh, Peter E. Wright, and Mark Rance. Sensitivity improvement in proton-detected two-dimensional heteronuclear correlation NMR spectroscopy. *J. Magn. Reson.*, 93:151–170, 1991.
- [221] J. Schleucher, M. Schwendinger, M. Sattler, P. Schmidt, O. Schedletsky, S. J. Glaser, O. W. Sørensen, and C. Griesinger. A general enhancement scheme in heteronuclear multidimensional NMR employing pulsed field gradients. *J. Biomol. NMR*, 4:301–306, 1994.

- [222] Lewis E. Kay, Paul Keifer, and Tim Saarinen. Pure absorption gradient enhanced heteronuclear single quantum correlation spectroscopy with improved sensitivity. *J. Am. Chem. Soc.*, 114:10663–5, 1992.
- [223] Daniel O. Cicero, Gaetano Barbato, and Renzo Bazzo. Sensitivity Enhancement of a Two-Dimensional Experiment for the Measurement of Heteronuclear Long-Range Coupling Constants, by a New Scheme of Coherence Selection by Gradients. *J. Magn. Reson.*, 148:209–213, 2001.